

UNICAMP

UNIVERSIDADE ESTADUAL DE CAMPINAS
Instituto de Física "Gleb Wataghin"

GABRIEL BOTOGOSKE

**Application of Arapuca technology for detection of
scintillation light in liquid argon and Cherenkov radiation
in water**

**Aplicação da tecnologia Arapuca para detecção de luz de
cintilação em argônio líquido e radiação Cherenkov em
água**

Campinas

2023

Gabriel Botogoske

**Application of Arapuca technology for detection of
scintillation light in liquid argon and Cherenkov radiation
in water**

**Aplicação da tecnologia Arapuca para detecção de luz de
cintilação em argônio líquido e radiação Cherenkov em
água**

Dissertação apresentada ao Instituto de Física "Gleb Wataghin" da Universidade Estadual de Campinas como parte dos requisitos exigidos para a obtenção do título de Mestre em Física na área de Física.

Dissertation presented to the "Gleb Wataghin" Institute of Physics of the University of Campinas in partial fulfillment of the requirements for the degree of Master in Physics the Area of Physics.

Supervisor: Ana Amélia Bergamini Machado

Co-supervisor: Anderson Campos Fauth

Este trabalho corresponde à versão final da Dissertação defendida pelo aluno Gabriel Botogoske e orientado pela Profa. Dra. Ana Amélia Bergamini Machado.

Campinas

2023

Ficha catalográfica
Universidade Estadual de Campinas
Biblioteca do Instituto de Física Gleb Wataghin
Lucimeire de Oliveira Silva da Rocha - CRB 8/9174

B657a Botogoske, Gabriel, 1996-
Application of ARAPUCA technology for detection of scintillation light in liquid argon and Cherenkov radiation in water / Gabriel Botogoske. – Campinas, SP : [s.n.], 2023.

Orientador: Ana Amélia Bergamini Machado.
Coorientador: Anderson Campos Fauth.
Dissertação (mestrado) – Universidade Estadual de Campinas, Instituto de Física Gleb Wataghin.

1. X-ARAPUCA. 2. Cintiladores. 3. Radiação Cherenkov. 4. Experimento SBND. 5. Argônio. I. Machado, Ana Amélia Bergamini, 1975-. II. Fauth, Anderson Campos, 1957-. III. Universidade Estadual de Campinas. Instituto de Física Gleb Wataghin. IV. Título.

Informações Complementares

Título em outro idioma: Aplicação da tecnologia ARAPUCA para detecção de luz de cintilação em argônio líquido e radiação de Cherenkov em água

Palavras-chave em inglês:

X-ARAPUCA

Scintillators

Cherenkov radiation

SBND experiment

Argon

Área de concentração: Física

Titulação: Mestre em Física

Banca examinadora:

Ana Amélia Bergamini Machado [Orientador]

Alessandra Tomal

William Badgett

Data de defesa: 19-05-2023

Programa de Pós-Graduação: Física

Identificação e informações acadêmicas do(a) aluno(a)

- ORCID do autor: <https://orcid.org/0000-0001-6525-5475>

- Currículo Lattes do autor: <http://lattes.cnpq.br/6396800117961371>



INSTITUTO DE FÍSICA
GLEB WATAGHIN

MEMBROS DA COMISSÃO EXAMINADORA DA DISSERTAÇÃO DE MESTRADO DO ALUNO GABRIEL BOTOGOSKE - RA 198034 APRESENTADA E APROVADA AO INSTITUTO DE FÍSICA GLEB WATAGHIN, DA UNIVERSIDADE ESTADUAL DE CAMPINAS, EM 19/05/2023.

COMISSÃO JULGADORA:

- Profa. Dra. Ana Amélia Bergamini Machado - Presidente e orientadora (IFGW/UNICAMP)
- Profa. Dra. Alessandra Tomal (IFGW/UNICAMP)
- Dr. William Badgett (Fermi National Accelerator Laboratory)

OBS.: Ata da defesa com as respectivas assinaturas dos membros encontra-se no SIGA/Sistema de Fluxo de Dissertação/Tese e na Secretaria do Programa da Unidade.

CAMPINAS

2023

This work is dedicated to my brother, Mateus Botogoske, the greatest warrior who ever lived.

Acknowledgements

This study was financed in part by the Coordenação de Aperfeiçoamento de Pessoal de Nível Superior - Brasil (CAPES) - Finance Code 001. So first I would like to thank the financial support of "Ministry of Science, Technology and Innovation" and the "National Council for Scientific and Technological Development – CNPq" (130296/2021-0).

I want to thank my advisor Ana Amélia Bergamini Machado for all the support, friendship, and help in this work and for always have trusted me. I also want to thank my co-advisor, Anderson Campus Fauth, for everything that he taught me in theoretical and experimental physics. Another professor I want to thank is Ettore Segreto for all the support and help with the collection and analysis of data for the X-ARAPUCA experiment.

The next persons that I want to thanks are my parents Elio Joly Botogoske and Helenice Jacira Costa Botogoske for always being on my side, and also my brother and my best friend and my hero Mateus Botogoske. Without them, I wouldn't be here. I also want to thank for everything, my friend that is like my brother, Adil Coelho. Still related to family I want to homage my cats (Bella and Zoe) for the company throughout the years, and my dogs that passed way two years ago (Dandara and Lorelai).

The next three persons I want the thanks are the ones of the greatest friends I ever have and who helped me when I was on Fermilab Site. First is Heriques Frandini Gatti for all the help with the SBND work and for creating the design of the C-Arapuca. The next persons are Gabriela Vitti Stenico and Pedro Simoni Pasquini for helping me understand neutrino and particle physics.

Also related to SBND work I want to thank William Badgett, Vincent Basque, Matt Troups, Polina Abratenko, and Anne Schukraft for all the help. Related to the transport of the SBND detector I want to thank Mônica Soares Nunes, Shishir Shetty, and Nicola McConkey.

In UTFPR I would like to thank Luciana Rocha Hirsch for helping me at start of this cycle. Other UTFPR teachers I want to thanks are Daniel Rossato, Bruno Sens Chang, and Rafael Barreto.

Related to Leptons Laboratory, I want to thank Henrique Vieira de Souza for the codes provided and for help to understand them. Then I would like to thank Vinicius Pimentel from CTI "Renato Archer" for helping me from the start of my masters with this work, be with C-Arapuca, SBND or the "Tower of Piza".

Still in Leptons Laboratory, I want to thank Vinicius Andreossi with the simulation the the X-Arapuca setup. Then I would like to thanks Patricia Duarte de Almeida with the dichroic filter transmittance spectrum of the X-ARAPUCA and C-Arapuca . Then I would like to thank Eliabe Duarte Queiroz for reducing the noise in the experimental setup. I also want to thank Mariana Mischieri for her initial help in assembling the first C-Arapuca barrel and for being the best pupil. I also want to thank Frederico Luciano Demolin for helping to learn how to use the 3D printer.

As a man, I'm flesh and blood, I can be ignored, I can be destroyed; but as a symbol... as a symbol I can be incorruptible, I can be everlasting. (Batman Begins - 2005).

Resumo

O ARAPUCA é um dispositivo idealizado e desenvolvido para aprisionar e detectar fótons provindos da interação de neutrinos em experimentos de argônio líquido. Os neutrinos são partículas fundamentais que possuem propriedades ainda não completamente entendidas, por esta razão são os melhores instrumentos para estudar a física além do modelo padrão das partículas. Uma das características peculiares dos neutrinos é o fenômeno de oscilação, onde um tipo de neutrino pode se transformar em outro tipo. O maior experimento dedicado a física de oscilação de neutrinos que está sendo construído, que utiliza argônio líquido como meio de interação é o DUNE (Deep Underground Neutrino Experiment). Enquanto o DUNE irá estudar as oscilações de neutrinos a longo alcance, existe também um programa de experimentos para o estudo das oscilações de neutrinos a curto alcance, o SBND (Short Baseline Neutrino Detector) é um desses experimentos. O sistema de fóton detecção tanto de DUNE quanto de SBND é composto por X-ARAPUCAs (uma versão otimizada da ARAPUCA). Existe também a possibilidade da aplicação do ARAPUCA para detectar fótons providos de radiação Cherenkov em água. Experimentos construídos para o estudo de raios cósmicos podem ser beneficiados com o uso do Cherenkov-ARAPUCA, ou simplesmente, C-ARAPUCA. O objetivo deste trabalho é desenvolver e testar duas novas versões da ARAPUCA, a X-ARAPUCA para luz visível e a C-ARAPUCA.

Palavras-chave: ARAPUCA, Cintilação, Cherenkov, SBND, Argônio

Abstract

The ARAPUCA is a device designed and developed to trap and detect photons resulting from the interaction of neutrinos in liquid argon experiments. Neutrinos are fundamental particles that possess not yet fully understood properties, which is why they are the best tools for studying physics beyond the standard model of particles. One of the peculiar characteristics of neutrinos is the phenomenon of oscillation, where one type of neutrino can transform into another type. The largest experiment dedicated to neutrino oscillation physics that is being built, which uses liquid argon as the interaction medium, is the DUNE (Deep Underground Neutrino Experiment). While DUNE will study long-range neutrino oscillations, there is also a program of experiments for the study of short-range neutrino oscillations, and the SBND (Short Baseline Neutrino Detector) is one of those experiments. The photon detection system for both DUNE and SBND is composed of X-ARAPUCAs (an optimized version of ARAPUCA). There is also the possibility of using ARAPUCA to detect photons provided by Cherenkov radiation in water. Experiments built for the study of cosmic rays can benefit from the use of the Cherenkov-ARAPUCA, or simply C-ARAPUCA. This work aims to develop and test two new versions of ARAPUCA, the X-ARAPUCA for visible light and the C-ARAPUCA.

Keywords: ARAPUCA, Scintillation, Cherenkov, SBND, Argon

List of Figures

Figure 1 – W^- boson decaying into a massive lepton (electron, muon or tau) and its respective neutrino	28
Figure 2 – Excessive neutrinos observed in miniBoone [1]	31
Figure 3 – Higgs' mechanism for the Dirac's particle [2]	32
Figure 4 – Higgs' mechanism for the Majorana particle [2]	33
Figure 5 – Localization of each SBN detector [3]	35
Figure 6 – Expected oscillation of the neutrino beam as function of the travelled distance, for two possibles Δm_{41} [4]	36
Figure 7 – Histogram of types of neutrino that form the neutrino beam as function of energy [5]	37
Figure 8 – LArTPC of SBND [6]	38
Figure 9 – Signals in U,V and Y planes [7]	39
Figure 10 – Principle of work of a LArTPC [4]	39
Figure 11 – Scintillation intensity, showing the fast, slow and total component [8] .	40
Figure 12 – Scintillation process of the Liquid Argon [9]	41
Figure 13 – Graphic of the generated charge and number of generated photons (both normalized) in function of the applied electric field [10]	44
Figure 14 – Channels of interaction of neutrino in liquid argon	45
Figure 15 – PDS system	46
Figure 16 – Differences with the DAPHNE and APSAIA X-ARAPUCAs	47
Figure 17 – Distribution of the X-ARAPUCAs on each side of the LArTPC	48
Figure 18 – Illustrated scheme of the ARAPUCA, S1 is the first organic scintillator and S2 is the second organic scintillator [11]	49
Figure 19 – Transmittance and reflectance spectrum of the dichroic filter [12]	50
Figure 20 – Para-terphenyl(PTP) [13]	50
Figure 21 – Tetraphenyl-butadiene (TPB) [14]	50
Figure 22 – PTP's luminescence spectrum [15]	51
Figure 23 – TPB's Absorption spectrum [16]	51
Figure 24 – TPB's fluorescence spectrum [9]	52
Figure 25 – VIKUITI ESR's reflectivity spectrum [17]	53
Figure 26 – Illustrative scheme of the X-ARAPUCA [18]	54
Figure 27 – Illustrative scheme of the cone that separates the photons that suffer total internal reflection and those who do not suffer	55
Figure 28 – Photon capture mechanism of the X-ARAPUCA [19]	56

Figure 29 – The 4 APSAIAs of SBND	58
Figure 30 – High Voltage Supply electric schematic of APSAIA	59
Figure 31 – Amplifier electric schematic of APSAIA	59
Figure 32 – The APSAIAs connected to the flange	60
Figure 33 – The APSAIAs connected to the flange	61
Figure 34 – Block diagram of the APSAIA readout electronics	61
Figure 35 – Electric schematic of the setup	62
Figure 36 – Breadboard made to power supply all the APSAIAs and communicate them to the SBND server	63
Figure 37 – Switch utilized to communicate the APSAIAs to the server	64
Figure 38 – Adapter board from 8 wires to RJ45	65
Figure 39 – Botobox	65
Figure 40 – APSAIA gain configuration. Left: Low Gain Right: High Gain	66
Figure 41 – Bode plot of the frequency response of APSAIA	67
Figure 42 – APSAIA delay, in yellow the input signal in blue the output signal . . .	67
Figure 43 – Interface boards of the DAPHNE system (Jon Ameel)	68
Figure 44 – DAPHNE Front End Board	69
Figure 45 – DAPHNE Controller	69
Figure 46 – DAPHNE setup Diagram (Daniel Mishins)	70
Figure 47 – DAPHNE data out, using a trigger of 1Hz	71
Figure 48 – DAPHNE data format (Polina Abratenko)	72
Figure 49 – Registers Definition of FEB FPGA	72
Figure 50 – Light Monitoring System	73
Figure 51 – Electric diagram of the light monitoring system	75
Figure 52 – Python software of the light monitoring system	76
Figure 53 – Java software of the light monitoring system	77
Figure 54 – Light data for Box1	78
Figure 55 – Light data for Box2	78
Figure 56 – Light data for Box3	79
Figure 57 – Light data for Box4	79
Figure 58 – Angle software	80
Figure 59 – X-ARAPUCA used in this experiment	81
Figure 60 – OPTO dichroic filter spectrum	82
Figure 61 – Lightguide from glass to power	82
Figure 62 – Cryostat	83
Figure 63 – Support for the X-ARAPUCA and VIKUITI with TPB embedded . . .	83
Figure 64 – Diagram of the experimental setup	85

Figure 65 – Electrical configuration of the SiPMs	86
Figure 66 – Electrical diagram of the setup	87
Figure 67 – Simulated setup of the experiment	87
Figure 68 – Distance travelled by photons in TPB before being absorbed	88
Figure 69 – TPB Specrum of reemision	88
Figure 70 – Energy spectrum of emitted alphas	89
Figure 71 – Histogram of photons that arrived in the window per alpha emitted	89
Figure 72 – ADC CAEN equivalence to mV. The value b means the baseline put in the Wavedump configuration file (0 to 100)	90
Figure 73 – Signal without the filter	92
Figure 74 – Signal with the filter	93
Figure 75 – Mean Signal of the SiPM from channel 0 with 34V	94
Figure 76 – Mean Signal of the SiPM from channel 1 with 34V	94
Figure 77 – Mean Signal of the SiPM from channel 0 with 36V	95
Figure 78 – Mean Signal of the SiPM from channel 1 with 36V	95
Figure 79 – Mean Signal of the SiPM from channel 0 with 38V	96
Figure 80 – Mean Signal of the SiPM from channel 1 with 38V	96
Figure 81 – Histogram for 34V	97
Figure 82 – Histogram for 36V	98
Figure 83 – Histogram for 38V	98
Figure 84 – Fitted single-photon electron peaks	100
Figure 85 – Mean signal of one, two and three photo-electron generated	102
Figure 86 – Ratio charge in function of total charge	104
Figure 87 – Mean signal for muons and alphas	105
Figure 88 – Light signal for the alphas particles	107
Figure 89 – Light signal for the muons	107
Figure 90 – Crosstalk fit	109
Figure 91 – Histogram of detected photo-electron for the case of the alpha particles	110
Figure 92 – Efficiency fit	111
Figure 93 – Muon Decay	113
Figure 94 – Flux of cosmic rays protons as a function of energy [20]	114
Figure 95 – Primaries cosmic rays creating secondaries [21]	116
Figure 96 – Vertical muon flux as a function of momento [22]	117
Figure 97 – Stopping power of muon in cooper [23]	118
Figure 98 – Flux of vertical muons and another particle as function of altitude [20]	119
Figure 99 – Ratio of zenith muon flux to vertical flux [24]	120
Figure 100– Scheme of Cherenkov Radiation [21]	121

Figure 101–Spectrum of Cherenkov radiation in water for a particle with charge e and $\beta = 0.9997$	123
Figure 102–Density of Cherenkov photons. In the plot we can see the effect of absorption in low wavelengths explained in the text [25]	124
Figure 103–Preliminary barrel	125
Figure 104–Tyvek in the barrel	126
Figure 105–PMT used in the setup	127
Figure 106–Spectral sensitivity of the PMT [26]	128
Figure 107–Voltage divisor electric schematic	129
Figure 108–Conductive material on PMT	130
Figure 109–Amplitude histogram	131
Figure 110–Charge histogram. The parameters in table are the number of entries in the histogram, the value of the χ^2 fit using a gaussian fit (the red function), and the 3 fit parameters (constant, mean and standard deviation)	132
Figure 111–Theoretically histogram in function of voltage trigger	133
Figure 112–Histogram of noise and the muons, and the effect of increasing the gain and trigger threshold	134
Figure 113–Dark bottle	135
Figure 114–Charge histogram of the dry SiPM using a blue led. The meaning of each fit parameter is: P0 is the constant that multiplies the normalized noise Gaussian, P1 and P2 are the mean and the standard deviation the same gaussian. Meanwhile, P3 is the constant that multiplies the normalized Gaussian of the LED light signal, and for last P4 and P5 are the mean and the standard deviation of the second gaussian	135
Figure 115–New barrel of the setup	137
Figure 116–Tyvek in the new barrel	138
Figure 117–Schematic of the C-Arapuca setup	139
Figure 118–Scintillation vs Cherenkov spectre [27].	140
Figure 119–C-Arapuca design	141
Figure 120–C-Arapuca dichroic filter transmittance spectrum	141
Figure 121–Water prof connector of C-Arapuca	142
Figure 122–Different WLS spectrum of absorption and emission [28]	143
Figure 123–Photo efficiency of each SiPM. Left: VE Right:HS [29]	144
Figure 124–Refractive index of water as a function of wavelength	145
Figure 125–Absorbance spectrum of the wavelength shifter bar (WLS)	145
Figure 126–Reemission spectrum of the wavelength shifter bar (WLS)	146

Figure 127–Charge histogram of the PMT and the C-Arapuca inside the new tonel. The mean charge obtained for the PMT was 585 pC, and for the C-Arapuca was 1653pC	147
Figure 128–Possible order of the masses [2]	161
Figure 129–Particle traveling in a medium with speed in z direction [21]	162
Figure 130–Schematic of a PMT [8]	170
Figure 131–Equipotencial lines in Electron Optical Input System [8]	171
Figure 132–Electric Diagram of a voltage divider [26]	172
Figure 133–Plot of the gain as a function of the applied voltage [30]	173
Figure 134–Plot of the current as a function of the applied voltage and luminosity flux [8]	174
Figure 135–Scheme of PN junction [31]	176
Figure 136–Polarizing effect of a PN junction [31]	176
Figure 137–Microcells matrix forming a SiPM [32]	177
Figure 138–Electric diagram of a microcell [32]	178
Figure 139–Diagram of a SiPM band [33]	178
Figure 140–Scheme of an avalanche photodiode [33]	179
Figure 141–P-on-N and N-on-P photodiodes [34]	180
Figure 142–Photodiode P-on-N and N-on-P [33]	180
Figure 143–Electric model of a SiPM	182
Figure 144–Thevenin equivalent in discharge phase	183
Figure 145–Expected current signal when a photon is detected in a single cell [33] .	184
Figure 146–Gain as a function of Overvoltage [33]	185
Figure 147–Electric model of a SiPM [35]	186
Figure 148–Circuit for reading SiPM’s Signal	187
Figure 149–PDE as a function of overvoltage and wavelength [36]	188
Figure 150–Crosstalk and Afterpulses in a SiPM [33]	189
Figure 151– sp^2 hybridization process [37]	190
Figure 152–Shape of the orbitals [38]	190
Figure 153– π connections in the benzene molecule and resultant orbital [39]	191
Figure 154–Levels of energy of an organic scintillator [40]	191
Figure 155–Levels of energy of a organic scintillator [41]	192

List of Tables

Table 1 – Charges and Masses of the quarks [20]	24
Table 2 – Charges and Masses of the leptons [20]	25
Table 3 – Charge and Mass of the gauge boson. [20]	27
Table 4 – Noble gases and water properties [42]	46
Table 5 – Frequency Response	66
Table 6 – Information of each data run	91
Table 7 – Experimental data of the run 27	101
Table 8 – Table with integral and percentages of each photon electron	108
Table 9 – Results of the values in the voltage divisor	131
Table 10 – Values of the mixing angles [20]	160

List of abbreviations and acronyms

UNICAMP	Universidade Estadual de Campinas
IFGW	Instituto de física Gleb Wataghin
SM	Standard Model
SBND	Short Baseline Near Detector
DUNE	Deep Underground Neutrino Experiment
SBN	Short Baseline Neutrino
ARAPUCA	Argon R&D Advanced Program at UniCAmp
APSAIA	ARAPUCA Power Source And Input Amplifier
DAPHNE	Detector electronics for Acquiring PHotons from NEutrinos
PMT	PhotoMultiplier Tube
SiPM	Silicon PhotoMultiplier
LAr	Liquid Argon
LArTPC	Liquid Argon Time Projection Chamber
PDS	Photon Detection System

List of symbols

μ	Muon
ν	Neutrino
e^-	Electron
γ	Photon
α	Alpha particle
β	Beta particle

Contents

1	Introduction	22
2	Neutrinos physics	24
2.1	Standard Model	24
2.2	The neutrinos	27
2.3	Neutrinos Oscillation	29
2.4	Short Baseline Anomaly	30
2.4.1	Sterile Neutrino	31
2.4.1.1	Seesaw Mechanism	32
3	Short Baseline Near Detector	35
3.1	Accelerators and neutrino beam	36
3.2	Liquid Argon Time Projection Chamber	37
3.2.1	Liquid Argon Scintillation	40
3.2.2	Argon and Neutrinos	44
3.3	Photon Detection System	46
3.3.1	ARAPUCAs	48
3.3.1.1	ARAPUCA	48
3.3.1.2	X-ARAPUCA	54
3.3.2	Data Acquisition System	57
3.3.2.1	APSAIA	58
3.3.2.1.1	APSAIA Test Stand	62
3.3.2.2	DAPHNE	68
3.3.2.2.1	DAPHNE Test Stand	70
3.3.3	Light Monitoring System	73
4	First Estimation of VIS X-ARAPUCA detection efficiency	81
4.1	The X-ARAPUCA	81
4.2	The Setup	82
4.3	Electronics	85
4.4	Simulation	87
4.5	Data Acquisition	89
4.6	Data Analysis	91
4.7	Filtering the signal and Baseline	92
4.8	LED light	93
4.9	Single Photon Electron	99
4.10	X-ARAPUCA response	102

4.11	Alphas and Muons	103
4.12	Light Signal	105
4.13	Crosstalk	108
4.14	Efficiency	110
5	Cosmic Rays	113
5.1	Atmospheric Muons	116
5.1.1	Energy Loss	118
6	Cherenkov Radiation	121
7	Test Stand for the characterization of C-ARAPUCA for water Cherenkov light	125
7.1	Preliminary Setup	125
7.1.1	The Barrel	125
7.1.2	Electronics and softwares	126
7.1.3	PMT	127
7.1.4	Muon peak	130
7.1.5	SiPM test	135
7.2	Current Setup	136
7.2.1	New Barrel	136
7.2.2	The C-Arapuca	139
7.2.3	WLS and SiPMs	142
7.2.4	Expected efficiency	144
7.2.5	First Test of C-Arapuca device	147
8	Conclusion	149
	BIBLIOGRAPHY	151
	Appendix	156
	APPENDIX A Model of neutrino oscillation	157
	APPENDIX B Measured values of PMNS matrix	160
	APPENDIX C Cherenkov Radiation Derivation	162
C.1	The problem	162
C.1.1	The electromagnetic potentials	164
C.2	The Electromagnetic Fields	165
C.3	Spectrum	167
	APPENDIX D Photomultiplier	170
D.1	Photomultiplier Tube	170
D.1.1	Electron Optical Input System	171

D.1.2	Photomultiplication	172
D.1.3	Voltage Divider	172
D.1.4	Gain	172
D.1.5	Linearity	173
D.1.6	Quantum Efficiency	174
D.2	Silicon photomultipliers	175
D.2.1	PN Junction	175
D.2.1.1	Avalanche effect	177
D.2.2	SiPM	177
D.2.3	Electric Model	181
D.2.4	Measurement circuit	186
D.2.5	Photon Detection Efficiency	187
D.2.6	Noise Sources	188
D.2.6.1	Dark Noise	188
D.2.6.2	Afterpulse	189
D.2.6.3	Crosstalk	189
	APPENDIX E WaveLength Shifters	190

1 Introduction

The aim of this work is to study different applications for the X-ARAPUCA device, which are using Scintillation light in liquid argon or using Cherenkov radiation in water.

The ARAPUCA (3.3.1) device was idealized to improve the photon detection efficiency in a Liquid Argon Time Projection Chamber (LArTPC). The concept is to trap photons inside a box with highly reflective internal surfaces, so that the detection efficiency of trapped photons is high even with a limited active coverage of its internal surface. Scintillation light in a LArTPC has a wavelength around VUV (Vacuum Ultra Violet $\approx 127\text{nm}$).

After the success of the working principle and the validation test performing during the first run of protoDUNE [43], the ARAPUCA becomes the photon detection design for the DUNE (Deep Underground Neutrino Experiment) [44]. An optimization of this idea is called X-ARAPUCA [19]. The X-ARAPUCA can reach a higher efficiency and facilitate the construction and assembly of the device. Since 2017 a full R&D program have being done in order to validate and optimizing this device not only in a bench setup in different laboratories (UNICAMP-FERMILAB-CERN-CIEMAT-MIB) but also in a real physics experiment as SBND (Short Baseline Near Detector)[5].

SBND makes part of the Short Baseline Neutrino Program which explore neutrino oscillation in a short range from the beam production. This program consist in 3 LArTPC detectors at different distances of the neutrino beam production. Beyond VUV light, SBND will also have visible light , due to the foils installed in the cathode of the experiment. These foils are coated with an wavelength shifter that converts VUV photons into visible ones (VIS), giving a second chance to be detected. As we will have VUV and VIS photons, we need to have a device that is also sensitive to the visible ones.

One of the aims of this dissertation is the measurement of the efficiency detection for the VIS X-ARAPUCA and contributions to photodetection data acquisition for SBND experiment.

This work is also dedicate to the studies in build an ARAPUCA sensitive to water Cherenkov detector for use in cosmic rays experiment. We call this new device as C-ARAPUCA (Cerenkov-ARAPUCA), with the goal of use the device in the next generations of experiments.

Even that the principle for trap photons is the same, there are some difference

on the device. X-ARAPUCA for LArTPC requires to work in a cryogenic temperatures, the SiPM would have a low dark count rate, once it is working in a low temperatures, the mechanical structure needs to be resistant to thermal contraction. The main challenge in the C-ARAPUCA is the humidity inside the device, once the C-ARAPUCA will work into ultrapure water.

This dissertation is divided in three main part. The first one is dedicate to the front end electronics of the photon detection system of SBND experiment. The second part is the measure in our Laboratory at Unicamp of the detection efficiency for X-ARAPUCA sensitive for visible light The third part of this works is devoted for design, produce and tests of a C-ARAPUCA.

Thus, all the work in this dissertation, whether with the Light Visible X-ARAPUCA, the C-Arapuca proposal and the work on data acquisition electronics at SBND, are related to a central theme - ARAPUCAs.

In chapter 2 the standard model will be presented and then it will be followed by the physics of neutrinos. Then it will be explained that neutrinos are difficulty to detect and a lot of information about them are mysterious. More specifically will be treated about the neutrino oscillation anomaly at short baseline.

In chapter 3 will be presented the Short Baseline program, with focus in the the Short Baseline Neutrino Detector. The goal of the program is to validate the neutrino oscillation anomaly and to detect the sterile neutrino. Then it will be explained the LArTPC and the photo detection system. To understand how they work it will be shown a little of the theory about liquid argon scintillation and how an ARAPUCA work. For last is going to be shown the work done and the actual status of both data acquisition systems: APSAIA and DAPHNE. And in chapter 4 will be shown the experiment done to verify the VIS X-Arapuca efficiency.

Changing the subject in chapter 5 will be talked about cosmic rays and the atmospheric muons the free abundant secondaries particles that can be used to test the C-Arapuca. So will be shown the mean energy of the muon, the energy and angular distribution. In the same spirit, the chapter 6 will explain the Cherenkov radiation, since it will be used to detect the atmospheric muons talked in previous chapter.

In chapter 7 will be talked about the experiment and setup itself of the C-Arapuca. The experiment is divided in two, the preliminary setup and the current setup. The preliminary setup was used to validate the possibility of using a small water Cherenkov barrel to detect atmospheric muons. The current setup is the experiment for testing the C-Arapuca device.

2 Neutrinos physics

This section will make an introduction to neutrinos physics and what are their mysterious properties that today's experiments want to discover.

First, it will be explained the theory of the Standard Model. Then it will be explained neutrinos physics. For last it will be talked about the short baseline anomaly.

2.1 Standard Model

The known Universe is made of elemental particles. What we know about them is described by the Standard Model. The SM can explain almost all of the experimental data which is obtained in the area, and it is one of the most important concepts in physics nowadays.

The standard model list as particles: quarks, leptons, gauge bosons, and the Higgs boson.

The quarks can be found in 6 distinct flavors: up (u), down (d), strange (s), charm (c), top (t) and bottom (b). In the table 1 are shown the masses and the electric charge (in units of e).

Quark	Acronym	Mass	Charge (e)	Weak Isospin		Weak Hypercharge	
				Left	Right	Left	Right
Up	u	2.16 MeV	2/3	1/2	0	1/3	4/3
Down	d	4.67 MeV	-1/3	-1/2	0	1/3	-2/3
Charm	s	1.27 GeV	2/3	1/2	0	1/3	4/3
Strange	c	93.4 MeV	-1/3	-1/2	0	1/3	-2/3
Top	t	172.69 GeV	2/3	1/2	0	1/3	4/3
Bottom	b	4.18 GeV	-1/3	-1/2	0	1/3	-2/3

Table 1 – Charges and Masses of the quarks [20]

However the quarks are never found isolated in nature, they are always in bounded states (due to color lockdown, more details in [2]) forming baryons or mesons. The baryons are states formed by 3 quarks, and as an example we have the neutrons and the protons, formed respectively of udd and uud. But the mesons are states formed by two quarks, and as an example, we have the pions (π^0 , π^+ and π^-).

The other particle classification are the leptons. The leptons also are found in 6 distinct flavors, and they are: the muon (μ), the electron (e^-), the tau (τ), the muon

neutrino (ν_μ), the electron neutrino (ν_e) and the tau neutrino (ν_τ). In the table 2 are shown the masses and the electric charge (in units of e).

Lepton	Acronym	Mass	Charge (e)	Weak Isospin		Weak hypercharge	
				Left	Right	Left	Right
Electron	e^-	0.51 MeV	-1	-1/2	-1	-2	4/3
Muon	μ	105.66 MeV	-1	-1/2	-1	-2	4/3
Tau	τ	1776.86 MeV	-1	-1/2	-1	-2	4/3
Electron neutrino	ν_e	< 1.1 eV	0	1/2	X	-1	X
Muon neutrino	ν_μ	< 1.1 eV	0	1/2	X	-1	X
Tau neutrino	ν_τ	< 1.1 eV	0	1/2	X	-1	X

Table 2 – Charges and Masses of the leptons [20]

The electron, the muon and the tau have electric charge e^- , while the neutrinos have a null electric charge. By the standard model, theoretically, the neutrinos should have a mass equal to zero, however, nowadays we know that they must have mass - as will be discussed in 2.3.

The gauge bosons are responsible for the fundamental forces known today in nature, in order of magnitude: strong force, electromagnetic force, weak nuclear force and gravitational force, the last one not explained by the Standard Model. They are called bosons because they have an integer spin, different from quarks and leptons that have half spin and therefore are fermions.

The electromagnetic force mediator is the photon, having null mass and charge. Its representation is made through the unitary group (U(1)).

The weak nuclear force however has three mediators and they are: W^+ , W^- and the Z. Unlike the photon, they do have mass and, except for Z, they do have charge. They are represented by the special unitary group of degree 2 (SU(2)). The weak nuclear force is the only one that can change the flavor of the particles, being able to make a quark change its flavor to another quark flavor or a lepton change its flavor to another lepton flavor. The area that studies this force is called flavourdynamics.

Another interesting characteristic of this force is that exclusively particles with left-handed chirality and right-handed antiparticles can participate in the charged weak interaction (mediated by the W^+ and W^- bosons), hence is capable to break the CP symmetry.

The electromagnetic force and the weak nuclear force can be unified in a single force called electroweak force with U(1) X SU(2) gauge symmetry. Due to the break of the electroweak symmetry the four already mentioned gauge bosons, the photon, W^+ , W^-

and the Z emerged.

The symmetry break of the U(1) part creates the quantum number Y_W , known as weak hypercharge. The symmetry break of the SU(2) part creates the quantum number T_3 , known as weak isospin. Only particles with T_3 interact by charged weak interactions, therefore, of the elementary particles, only particles with left-handed chirality and antiparticles with right-handed chirality carry a weak isospin different than zero. In contrast, the coupling with the W boson is a linear combination of the weak isospin and the weak hypercharge.

For integrity reasons, the tables 1 and 2 were added as well columns representing the weak isospin and the weak hypercharge. The table is shown the values of both types of chirality: left-handed chirality (*Left*) and right-handed chirality (*Right*). For the respective antiparticles, you should simply reverse the sign of all values and exchange the columns *Right* and *Left*.

The already discussed symmetry break is responsible for the mass of the weak gauge bosons. Due they have mass, the weak nuclear force has a short range, unlike the electromagnetic force which has an infinity range, since the photon has its mass equal to zero.

The carrier of the strong force are the gluons and they are described by the SU(3) gauge's theory. Because of that symmetry, there are three types of force "charge", which are the colours, and they are named red, green and blue. Hence this area of Physics is called chromodynamics.

Quarks have a linear combination of those colours and anti-quarks have a linear combination of the anti-colours (they are anti-red, anti-green and anti-blue). However, because of the colour lockdown, the sum total must be equal to zero - that means that the final colour of the particle has to be "white". For mesons - there are formed by two quarks - one of the particles must be the anti-colour of the other, in other words, if one of the particles is red, the other particle must be anti-red. For baryons - there are formed by three quarks - every one of the particles must have distinct colors in such a way that the "combination" of those colours is white. The gluons however only couple particles with colour charge different from zero.

The gluons are the exception and don't have to be white, in fact gluons show two colour charges at the same time: one normal colour and one anti-colour. Is to be expected that there are nine distinct types of gluons, once there are three colours and three anti-colours, however there are only eight SU(3) group generators, and therefore only eight type of gluons. However, due to colour lockdown, the gluons are confined only

to the surroundings of the quarks. So even though the gluons don't have mass, the strong force does not have an infinity range.

The leptons do not have colour charge, and therefore do not participate in strong force. This is main difference between quarks and leptons.

The four gauge bosons of the electroweak force plus the eight gluons have spin equal to one. The only gauge boson that was not discovered yet is the graviton, responsible for the gravitational force and it's not really a part of the Standard Model. It is expected that its mass is equal to zero, once the gravitational force has an infinity range. Its also expected that the has spin equal to two, once its source is the energy-momentum tensor. The gravity is the weakest one of the four fundamental forces.

In the table 3 is shown the gauge boson characteristics.

Gauge boson	Spin	Mass	Charge(e)	Weak isospin	Weak hypercharge
Photon	1	0 eV	0	0	-0
W^+	1	80.34 GeV	1	+1	0
W^-	1	80.34 GeV	-1	-1	0
Z	1	91.19 GeV	0	0	0
Gluon	1	0 eV	0	0	0
Graviton	2	0 eV	0	0	0

Table 3 – Charge and Mass of the gauge boson. [20]

Finally, we have the Higgs boson that is a substantial piece of the standard model and the last one of them to be discovered - at least at this moment. The Higgs boson is a particle with a spin equal to zero, and its interaction with the standard model's fundamental particles generates the masses of those. Furthermore, it is responsible for the electroweak symmetry break that was explained earlier.

2.2 The neutrinos

The neutrinos are the second most abundant particles that are part of the standard model (more details in 2.1, losing only to the photons) and, however, the most difficult to detect - the reason behind that was explained in 2.1. The neutrino does not interact with the strong force and - because of its neutral charge - it does not interact with the electromagnetic force. The neutrino interacts only with the gravitational and the weak force, however - due to the fact that its mass is too small - its interaction with the gravitational force is weak. Therefore its only effective interaction with the rest of the universe is the weak nuclear force.

The neutrinos exist in three different flavours: The electron neutrino, the muon neutrino and the tau neutrino. The names are based on how they are created from a weak charged current. For instance, if a neutrino is created with an electron in weak interaction, this neutrino will be called an electron neutrino. If it's created with a muon, it'll be called an muon neutrino and the same logic works with the tau neutrino. In the figure 1 it is shown each one of the given examples.

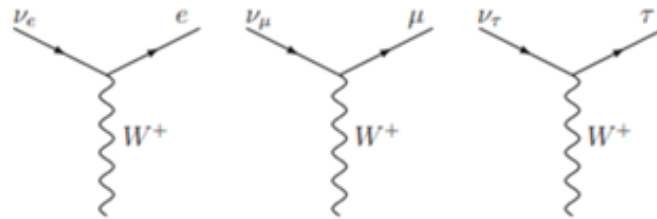


Figure 1 – W^+ boson decaying into a massive lepton (electron, muon or tau) and its respective neutrino

This happens because a quantity called leptonic number is conserved. There are three types of lepton number: the muon lepton number, the electron lepton number and the tau lepton number. As an example, the electron and the electron neutrino carry value +1 in its electron number and 0 in the other two numbers. The antiparticles, however, carry the opposite value, for instance, the positron carries the value -1 in its electron number. However, it is necessary to notice that the number is usually conserved - which will be explained in 2.3.

Another important characteristic of the neutrinos is that they always have left-handed chirality and helicity, and the antineutrinos have right-handed chirality and helicity.

The helicity is a projection of the spin in the movement direction and it is a movement constant. The chirality is more abstract, but represents how it transforms in Poincare's representation, and it is a Lorentz invariant. In the massless regime, both of them represent the same thing. Therefore, if the neutrino has no mass it would be coherent to find only neutrinos with the same chirality and helicity, however, since the neutrino has mass, it is expected that its chirality evolves in time.

Neutrinos have a lot of other open questions. Today physics knows that neutrinos have mass, but don't know their mass of them. It's only known that they are the lightest standard model particle (with exception of the photon). By the fact they have mass, neutrinos oscillate between their flavor states but we don't know if neutrinos and anti-neutrinos oscillate differently (CP violation in leptonic sector). The order of mass hierarchy

isn't now today and as a consequence isn't known which neutrinos' mass is heavier. Also isn't known if neutrinos are Dirac particles or Majorana particles, and if exist other types of neutrinos and interactions. Neutrinos can also be candidates to be dark matter.

2.3 Neutrinos Oscillation

Intending to measure the solar neutrino flux, the Homestake [45] experiment was designed. In this experiment, was expected a neutrino interaction ratio of 1.7 per day and only 0.48 per day were being detected. This was the first evidence that something was missing in the Physic theory of neutrinos.

The anomalous result persisted, in the Super-kamiokande experiment that utilizes the Cherenkov radiation - which will be explained in more detail in 6 - measured 0,465 of the expected flux of electron neutrinos originating from the Sun.

One of the hypotheses for this problem is that the electron neutrino, during the path from the Sun to the Earth, was changing into two different flavors: the tau and the muon flavor. Since the neutrino has mass, it was shown in [46] that could exist the possibility of the neutrinos oscillating between flavors.

To determine whether, in fact, the neutrinos were changing flavors, the experiment Sudbury Neutrino Observatory (SNO) was designed [47]. In this experiment were measured, individually, the three types of neutrinos arriving on the Earth. The expected electron neutrino flux was to be $(5, 1_{-0.81}^{+1.01}).10^{-6}cm^{-2}.s^{-1}$.

The measured flux is shown in 2.1.

$$\begin{aligned}\phi(\nu_e) &= (1, 76 \pm 0, 14).10^{-6}cm^{-2}.s^{-1} \\ \phi(\nu_\mu + \nu_\tau) &= (3.41_{-0.90}^{+0.93}).10^{-6}cm^{-2}.s^{-1}\end{aligned}\tag{2.1}$$

Therefore, the total flux it's the sum of both fluxes that is equal to $(5, 09_{-0.86}^{+0.90}).10^{-6}cm^{-2}.s^{-1}$ [47], which is consistent with the solar model.

There were two choices: accept that the solar model was mistaken and the Sun can produce others neutrino flavors, or assume that the electron neutrinos change into other flavors, this way changing the known Standard model. In fact, the second option was right and, in 2015, both experiments - SNO and the Super-Kamiokande - won the Nobel prize.

The neutrinos, as shown in 2.2, can be classified by their flavors. In quantum mechanics, they can be described in terms of their basis of flavour $|\nu_e\rangle, |\nu_\mu\rangle$ and $|\nu_\tau\rangle$.

The neutrino has mass, however differently of its expected that each flavour neutrino has a well-defined mass value, in fact each neutrino flavour is a linear combination of three distinct mass states, $|\nu_1\rangle, |\nu_2\rangle$ and $|\nu_3\rangle$. Each state of mass has a different mass called m_1, m_2 and m_3 respectively. This linear combination is described in 2.2.

$$\begin{pmatrix} \nu_e \\ \nu_\mu \\ \nu_\tau \end{pmatrix} = \begin{pmatrix} U_{e1} & U_{e2} & U_{e3} \\ U_{\mu1} & U_{\mu2} & U_{\mu3} \\ U_{\tau1} & U_{\tau2} & U_{\tau3} \end{pmatrix} \begin{pmatrix} \nu_1 \\ \nu_2 \\ \nu_3 \end{pmatrix} \quad (2.2)$$

The 3x3 unity matrix described in the equation 2.2 is called Pontecorvo–Maki–Nakagawa–Sakata (PMNS) matrix. If each neutrino flavour has a well-defined mass value the matrix should be the identity matrix, however, this does not occur. The values known today of the PMNS matrix are shown in Appendix B.

The probability for an electron neutrino oscillates to another flavor is given by equation 2.3, where E is the neutrino energy and L is the distance traveled by the electron neutrino.

$$\begin{aligned} P(\nu_e \longrightarrow \nu_k)(L) = & \delta_{ek} - 4Re\left(\sum_{j>i}^{3,3} U_{kj}^* U_{ej} U_{ki}^* U_{ei} \sin^2\left(\frac{m_j^2 - m_i^2}{4E} L\right)\right) \\ & + 2Im\left(\sum_{j>i}^{3,3} U_{kj}^* U_{ej} U_{ki}^* U_{ei} \left(\sin\left(\frac{m_j^2 - m_i^2}{2E} L\right)\right)\right) \end{aligned} \quad (2.3)$$

Therefore the three fundamental wave numbers of oscillation are given by the equation 2.4(not in natural units).

$$k_{ji} = \frac{c^3(m_j^2 - m_i^2)}{4E\hbar} \quad (2.4)$$

This way, we conclude that the oscillations between flavors depend on the difference in the square of the masses. Oscillation experiments fix L and E to measure the free parameters. The full derivation is shown in Appendix A.

2.4 Short Baseline Anomaly

The Liquid Scintillator Neutrino Detector (LSND) experiment detected an anomaly not predicted by the theory explained in 2.3. The detector, which was placed 30 meters away from the origin of the neutrinos beam, detected an excess of electron neutrinos [48].

Then, the miniBoone experiment also detected anomalies in neutrinos oscillation. The detector was 540 meters away from the origin of the neutrinos beam. The experiment detected an excess of 638 electron neutrinos [1].

In the figure 2 it is shown the excessive electron neutrinos in function of the neutrino energy. The black points are the obtained data with their respective error bars. In the dashed line are the fitted curves for the possible values of $\sin^2 2\theta$ and Δm^2 - which will be explained in 2.4.1.

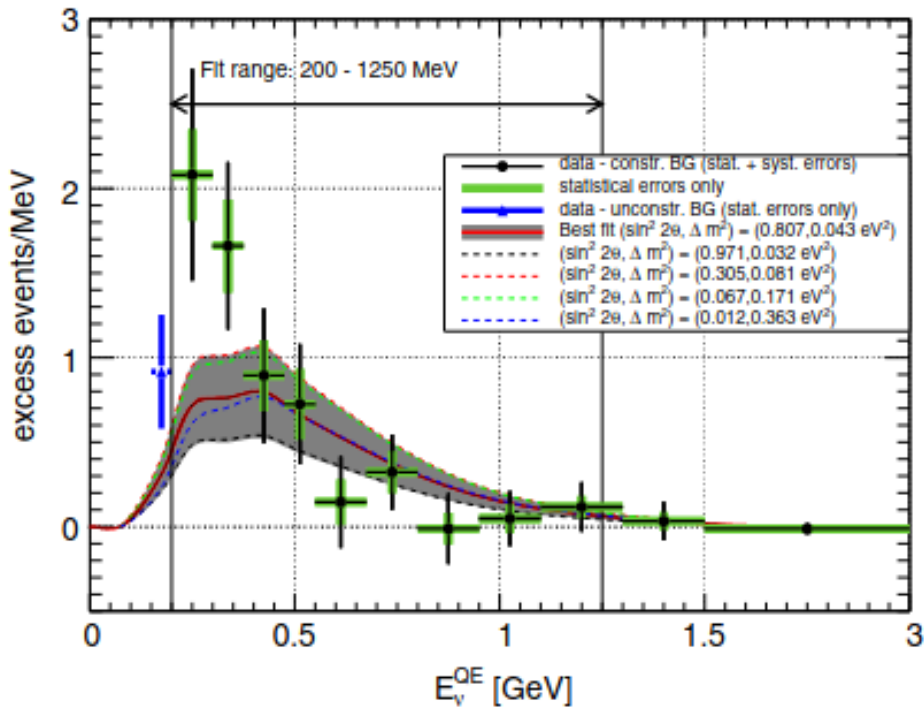


Figure 2 – Excessive neutrinos observed in miniBoone [1]

One of the possible explanations for the already explained anomaly is the existence of a fourth neutrino flavour, called the sterile neutrino. This neutrino would have no charge, no weak isospin and no weak hypercharge. In other words, they don't interact either with electromagnetic force or with strong and weak force (once they are leptons).

2.4.1 Sterile Neutrino

Considering this new flavour, the oscillation model 2.2 must be modified, adding the new flavour and a new state of mass, as shown in equation 2.5.

$$\begin{pmatrix} \nu_e \\ \nu_\mu \\ \nu_\tau \\ \nu_s \end{pmatrix} = \begin{pmatrix} U_{e1} & U_{e2} & U_{e3} & U_{e4} \\ U_{\mu1} & U_{\mu2} & U_{\mu3} & U_{\mu4} \\ U_{\tau1} & U_{\tau2} & U_{\tau3} & U_{\tau4} \\ U_{s1} & U_{s2} & U_{s3} & U_{s4} \end{pmatrix} \begin{pmatrix} \nu_1 \\ \nu_2 \\ \nu_3 \\ \nu_4 \end{pmatrix} \quad (2.5)$$

In a similar way to what was shown in A it is possible to calculate the probability of a flavour change into another. This probability is given by 2.6 in the short-range limit [49].

$$\begin{aligned} P(\nu_\alpha \longrightarrow \nu_\beta)(L) &= \sin^2(2\theta_{\alpha\beta}) \sin^2\left(\frac{\Delta m_{41}^2 L}{4E}\right) \\ P(\nu_\alpha \longrightarrow \nu_\alpha)(L) &= 1 - \sin^2(2\theta_{\alpha\alpha}) \sin^2\left(\frac{\Delta m_{41}^2 L}{4E}\right) \end{aligned} \quad (2.6)$$

In which the terms $\sin^2 2\theta_{\alpha\beta}$ are the functions of $U_{\alpha 4}$ and $U_{\beta 4}$ and the terms used in 2 to fit the curve are the Δm_{41}^2 and the term $\sin^2 2\theta_{\mu e}$.

2.4.1.1 Seesaw Mechanism

This section will explain one of the possibles origin of the normal and sterile neutrino masses, the seesaw mechanism.

The mass acquisition mechanism through the Higgs Bosons requires the existence of both chiralities. We could assume the existence of both chiralities for neutrinos and the Lagrangian of the neutrinos can be describe as in 2.7.

$$\mathcal{L}_D = -m_D(\bar{\nu}_R\nu_L + \bar{\nu}_L\nu_R) \quad (2.7)$$

This is equals to the following interaction, shown in the Feynman's diagram of the figure 3.

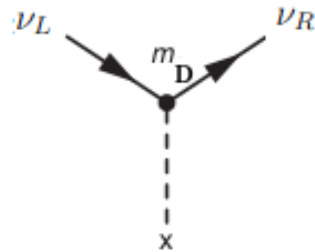


Figure 3 – Higgs' mechanism for the Dirac's particle [2]

However if that is, in fact, the origin of the neutrino's mass, it is expected to have a mass in the same order of magnitude of the others elemental particles.

Another neutrino mass acquisition form, since it does not have charge, it is through the following Lagrangian 2.8, without breaking the gauge invariance required to the Standard model.

$$\mathcal{L}_M = -\frac{m_M}{2}((\bar{\nu}^C)_L \nu_R + \bar{\nu}_R (\nu^C)_L) \quad (2.8)$$

The C index is the CP operator that causes the change of charge and reverses the chirality. In other words, $(\Psi_{L,R})^C = \Psi^C_{R,L}$. Therefore is the operator that changes the particle for its antiparticle with the reversed chirality. Hence the equation 2.8 can be described as 2.9.

$$\mathcal{L}_M = -\frac{m_M}{2}(((\nu_R)^C) \nu_R + \bar{\nu}_R \nu_R^C) \quad (2.9)$$

This mechanism, in theory, is possible for the neutrino, because - since it does not have charge - the coupling of particle and antiparticle - as shown in 4 - does not violate the conservation of the electric charge.

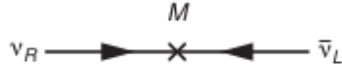


Figure 4 – Higgs' mechanism for the Majorana particle [2]

Particles that acquire mass for this model are called Majorana particles, and that imposes the nonexistence of a distinction between the particle and its antiparticle. In other words, the particle is its own antiparticle.

The mechanism that expects neutrinos to have mass is a combination of the mechanism already mentioned: Dirac and Majorana. The Lagrangian becomes 2.10.

$$\mathcal{L}_{DM} = -m_D \bar{\nu}_L \nu_R - \frac{m_R}{2} (\nu_R)^C \nu_R - \frac{m_L}{2} \bar{\nu}_L (\nu_L)^C + h.c. \quad (2.10)$$

The first term is the coupling of the left-handed chirality neutrino with the right-handed chirality neutrino, generating the Dirac mass (m_D). The second term is the coupling of a left-handed chirality antineutrino with a right-handed chirality antineutrino, generating the Majorana mass (m_R). The last term is the coupling of a left-handed neutrino with a right-handed neutrino, generating the Majorana mass (m_L).

Writing in matrix form the equation 2.10 it is obtained the equation 2.11, remembering that $\bar{\nu}_L \nu_R = \bar{\nu}_R^C \nu_L^C$, due to the condition of the Majorana.

$$\mathcal{L} = -\frac{1}{2} \begin{pmatrix} \bar{\nu}_L & (\bar{\nu}_R)^C \end{pmatrix} \begin{pmatrix} m_L & m_D \\ m_D & m_R \end{pmatrix} \begin{pmatrix} (\nu_L)^C \\ \nu_R \end{pmatrix} + h.c. \quad (2.11)$$

When diagonalizing the matrix we got the eigenvalues of the masses described by the equation 2.12.

$$m, M = \frac{m_R + m_L}{2} \pm \sqrt{\left(\frac{m_R - m_L}{2}\right)^2 + m_D^2} \quad (2.12)$$

Equating the term m_L to zero, once the standard model does not allow this term because it breaks the expected symmetries [50], and also assuming that m_R is way bigger than m_D , we got the following mass values shown in 2.13.

$$\begin{aligned} m &\approx \frac{m_D^2}{m_R} \\ M &\approx m_R \end{aligned} \quad (2.13)$$

In other words, for each flavour exists a very small mass that is associated to with a active left-handed chirality neutrino and a much bigger mass that is associated to a right-handed chirality neutrino, that is the sterile neutrino.

3 Short Baseline Near Detector

The Short Baseline Near Detector (SBND) will be an experiment part of the Short Baseline Neutrino Program (SBN), which is located at Fermi National Accelerator Laboratory (Fermilab).

The main goals of this program is to verify the short-baseline neutrino anomaly (2.4) to test the sterile neutrino hypothesis (2.4.1), to develop and improve the LarTPC technology and to study the interactions between the neutrinos with the atoms of argon, the last two to help to development of the DUNE ([51]).

The program is made of three detectors: SBND, μ BooNE and ICARUS, in order from near to far from the neutrino beam origin. The SBND is located 110m from the beam origin and will use 270 tons of argon, which 112 tons will be the active volume. The μ BooNE stays at 470 m from the detector and the ICARUS at 600m. More information can be seen in figure 5.

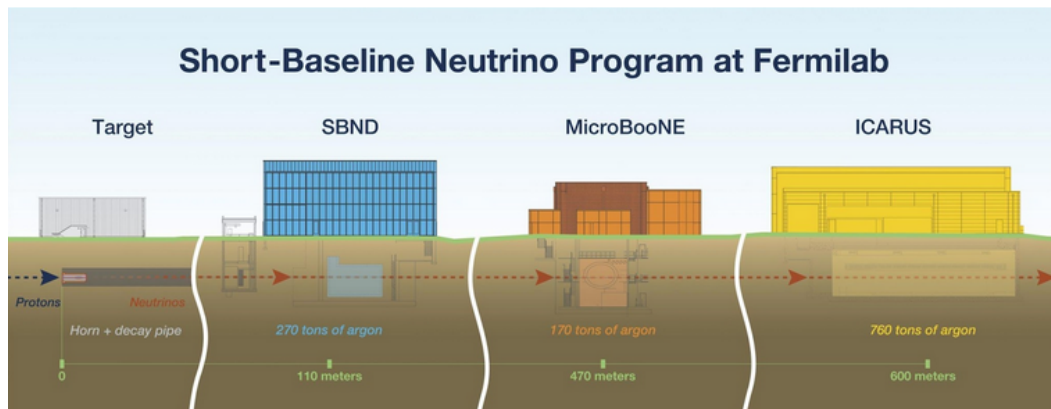


Figure 5 – Localization of each SBN detector [3]

SBN will use this three detectors to measure oscillations of neutrinos at different distant of the source.

In figure 6 is shown the expected oscillation of the neutrino flux per travelled distance. The SBND will measure the data from neutrinos that are almost the same from the origin.

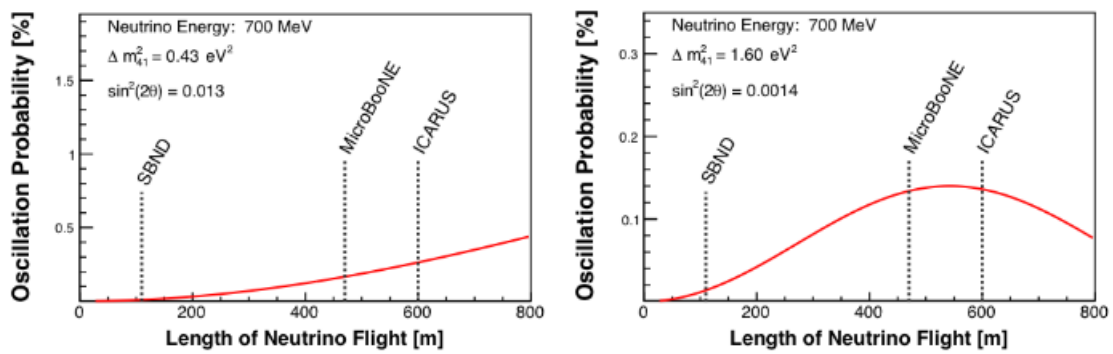


Figure 6 – Expected oscillation of the neutrino beam as function of the travelled distance, for two possible Δm_{41} [4]

3.1 Accelerators and neutrino beam

The neutrino beam is formed when accelerated protons collide with a beryllium's target. The protons are injected in the LINAC and are accelerated to 400 MeV kinetic energy. The LINAC sends those protons to the booster where they are accelerated from 400 MeV to 8 GeV kinetic energy. After that, they are extracted to the direction of the beryllium target.

From there the proton beam collides with the beryllium target and the products of the collision travel inside the decay pipe. The final result is the Booster Neutrino Beam (BNB). The particles that compound the final neutrino beam is shown in figure 7. The beam is most made of muon neutrinos, followed by anti muon neutrinos.

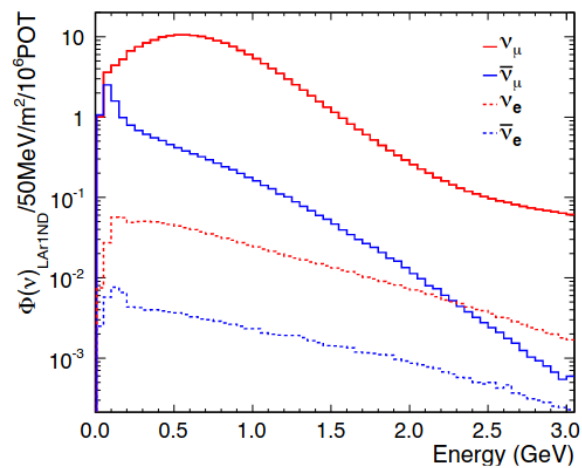


Figure 7 – Histogram of types of neutrino that form the neutrino beam as function of energy [5]

3.2 Liquid Argon Time Projection Chamber

The Liquid Argon Time Projection Chamber (LArTPC) is a particle detector that uses a strong electric field with a collection wire planes.

The SBND LArTPC is a box of dimensions 5mx4mx4m. In the interior of the LArTPC is filled with 112t of active Liquid Argon at 87K. The detector is made of one Cathode Plane Assemblies (CPA) in the center of the detector and 4 Anode Plane Assemblies (APA), 2 in each side parallel to the neutrino beam. The SBND's LArTPC can be seen in figure 8. The TPC will stay in the interior of a cryostat containing 270 ton of LAr.

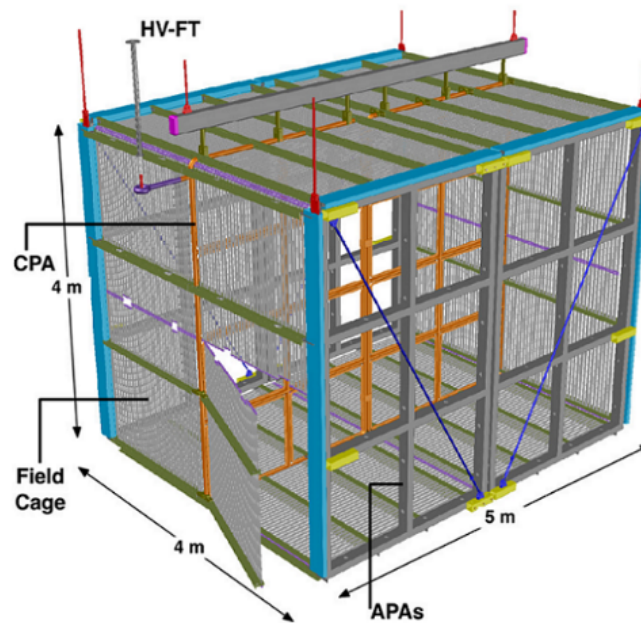


Figure 8 – LArTPC of SBND [6]

The voltage applied between the anode and the cathode is so that an electric field of 500V/cm appears inside the LArTPC from anode to cathode. So the cathode separates two electron drift regions.

When a neutrino coming from the neutrino beam arrives in the interior of the cryostat it generate electric particles that drift to the direction of the planes. The negative charges travel in direction to the anode.

Each APA is made of three wire planes, 2 of induction and one of collection, containing 3964 wires. The wires in collection plane are in the vertical, while the wires in the induction plane are in plus and minus 60° in relation of vertical, the U and V plane respectively.

When an electron cross the induction planes, the passage of the electric particles inducts a signal in the wire. Then the collection plane (Y Plane) is responsible to collect the electron and as consequence a current is formed. In figure ?? shown the expected signals in each plane.

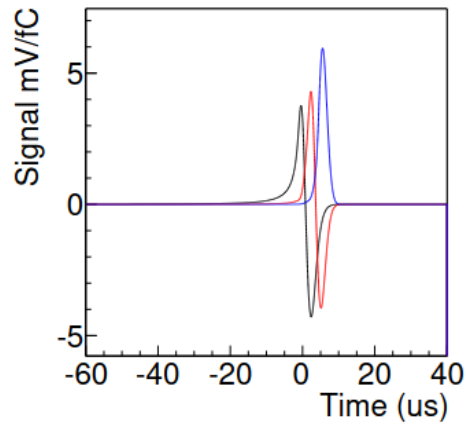


Figure 9 – Signals in U,V and Y planes [7]

As the electric particles are drifted to the APA, signals start to appear in different wires (space resolution) along the time. So in that way its possible to track the particles trajectories as shown in figure 10.

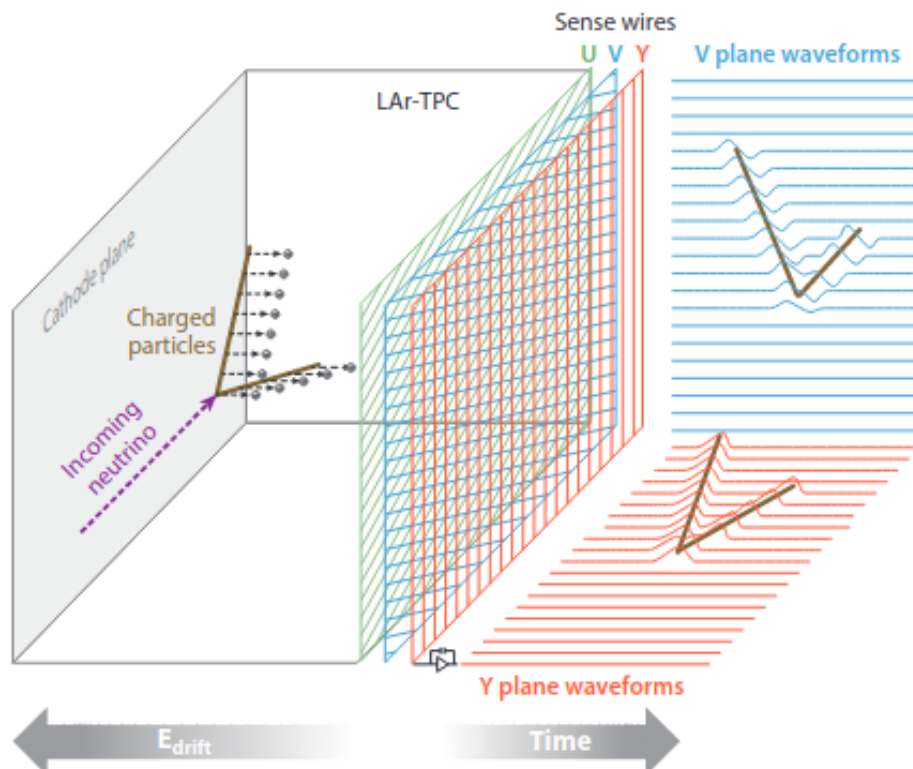


Figure 10 – Principle of work of a LArTPC [4]

3.2.1 Liquid Argon Scintillation

Scintillation is the process in which a certain material (called scintillator) emits photons due to the passage of energetic particles (photons, electrons, alpha particles, among others).

The light emission intensity can be describe as in 3.1.

$$N = N_s e^{-\frac{t}{\tau_s}} + N_f e^{-\frac{t}{\tau_f}} \quad (3.1)$$

In which N is the number of emitted photons, τ_s is the slow time constant, τ_f is the fast time constant, N_s are the number of photons emitted by the slow process, finally, N_f are the number of photons emitted by the fast process.

In the figure 11 it is shown the curves of scintillation of the fast component and of the slow component. The curve with the highest peak is the sum of the two components. it can be observed that the fast component decays faster than the slower - as it should be expected. The rise time can be disregarded, once it is much faster than the decay time.

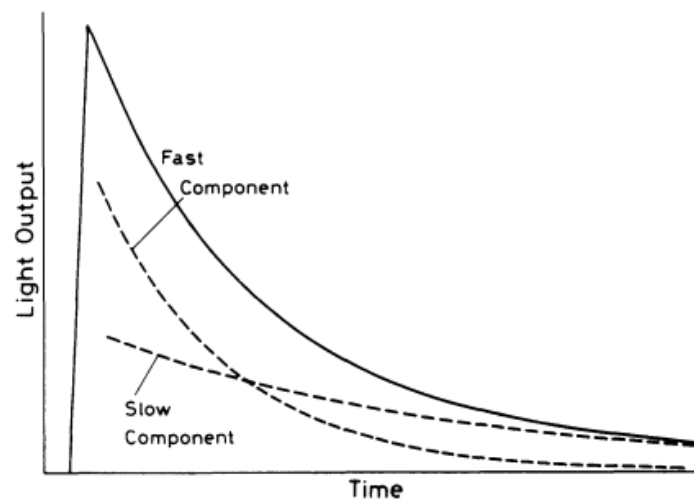


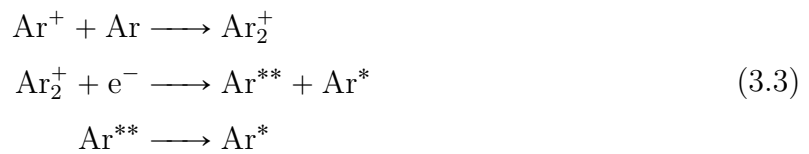
Figure 11 – Scintillation intensity, showing the fast, slow and total component [8]

Energetic particles when passing through liquid argon (LAr) gives energy to the Argon atoms by two distinct process. The first process, called excitation process, is the promotion of an argon atom to a higher level of energy, forming what is called exciton (Ar^*). The exciton interacts with a argon atom in the fundamental state through instant distortions in the lattice and momentarily forms (it takes only picoseconds) the excited

molecule (Ar_2^*). Then, the system decays to two argon atoms in the fundamental state, emitting a photon. The process explained in this paragraph is described by the equations in 3.2.



The second process, called recombination process, is the formation of a pair ion-electron. The formed cation of argon momentarily connects with a neutral argon atom, forming the Ar_2^+ element. Then the Ar_2^+ recombine itself with the electron that was generated in the cation creation process, forming a argon atom in the fundamental state and a Argon exciton called Ar^{**} , that is more energetic than the exciton Ar^* . This new exciton Ar^{**} decays to the exciton Ar^* through the emission of a phonon (heat). The exciton Ar^* , then suffers from the process already described by the equations 3.2. The recombination process is described in the equations 3.3.



An illustrative scheme of both process can be seen in the figure 12.

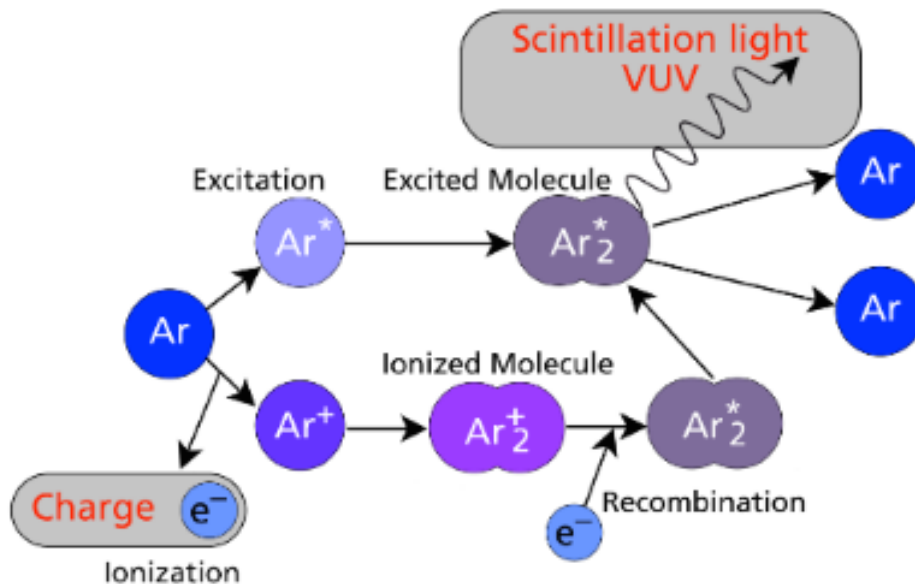


Figure 12 – Scintillation process of the Liquid Argon [9]

The excited state A_2^* is a singlet state and can decay in two forms to the fundamental state Ar_2 - which is a state dissociated from the singlet -, or it decays directly, originating a fast component of the spectrum; or it firstly decays to a A_2^* triplet state, then it decays to a Ar_2 state, originating the slow component of the spectrum. The reason for the last being a slow component in the spectrum is due to the same reasons explained in [E](#), that is, due to selection rules.

The wave length of the photon emitted by the slow component it is equal to 127,3 nm and by the fast component it is equal to 126,4 nm. In other words, the spectrum of both components are very close to each other. The time constant of the fast component (τ_f) is estimated to be about 7 ns, while the slow (τ_s) is about 1600 ns [[10](#)].

The ratio of the number of excited argon and the number of ionized argon are given [[10](#)] by the equation [3.4](#).

$$\frac{N_{ex}}{N_i} = 0.21 \quad (3.4)$$

Therefore, the maximum number of scintillation photons generated - considering that a recombination has happened - it is given by the equation [3.5](#).

$$N_{max} = N_i + N_{ex} \quad (3.5)$$

Using the equation [3.4](#) in [3.5](#) it is obtained the equation [3.6](#).

$$N_{max} = 1.21N_i \quad (3.6)$$

It is known in the literature that the average energy spent to form an electron and Ar^+ pair is equal to 23.6 eV [[10](#)]. Hence the equation [3.6](#) becomes [3.7](#), in which E_o is the energy given by the ionizing radiation that passed through the LAr.

$$N_{max} = 1.21 \frac{E_o}{23.6eV} = \frac{E_o}{19.5eV} \quad (3.7)$$

Therefore if the given energy (E_o) is equal to 1 MeV, the maximum number of photon generated is [3.8](#):

$$N_{max} = 1.21 \frac{1MeV}{23.6eV} = 5.13 \times 10^4 \text{photons} \quad (3.8)$$

As a result, the number of generated photons is equal to $5.13 \times 10^4 \frac{\gamma}{MeV}$. That's clear disregarding that part of the electrons can escape the recombination and other forms

of energy loss. In practice, this number is equal to $4.10^4 \frac{\gamma}{MeV}$, without any electric field applied.

The number of photons emitted per MeV of deposited energy varies according to the energy associated with the ionizing particle and the mainly mechanism that causes this variation also changes.

Talking now about the particle passage in the argon medium and the intensity between the fast and slow component. The ratio between singlet intensity in relation to the triplet intensity increases (I_f/I_s) as the energy of the particle increases. Actually this value is 0,3 to electrons and to the alpha particles (Helium atoms) is 1.3.

Since the energy of the first triplet and singlet states are almost the same, the difference of energy of different particles shouldn't be the directly responsible for the different intensity. The reason for this difference is the consequence of spin selection rule. This rule forbidden transitions from singlet-singlet. So at low energy the system is more allowed to go to triplet excited state. But as energy increases, this rule starts to fail and the multipole rules starts to rule, increasing the rate of singlet states created.

Furthermore, the scintillation process is affected by the electric field applied in the argon, once the electric field allows the electrons to escape from the Coulombian force generated by the Ar^+ , this way decreasing the number of recombinations.

In the figure 13 it is shown the collected charge and the light produced by the passage of electrons containing the energy of 1 MeV for the liquid argon and the liquid xenon.

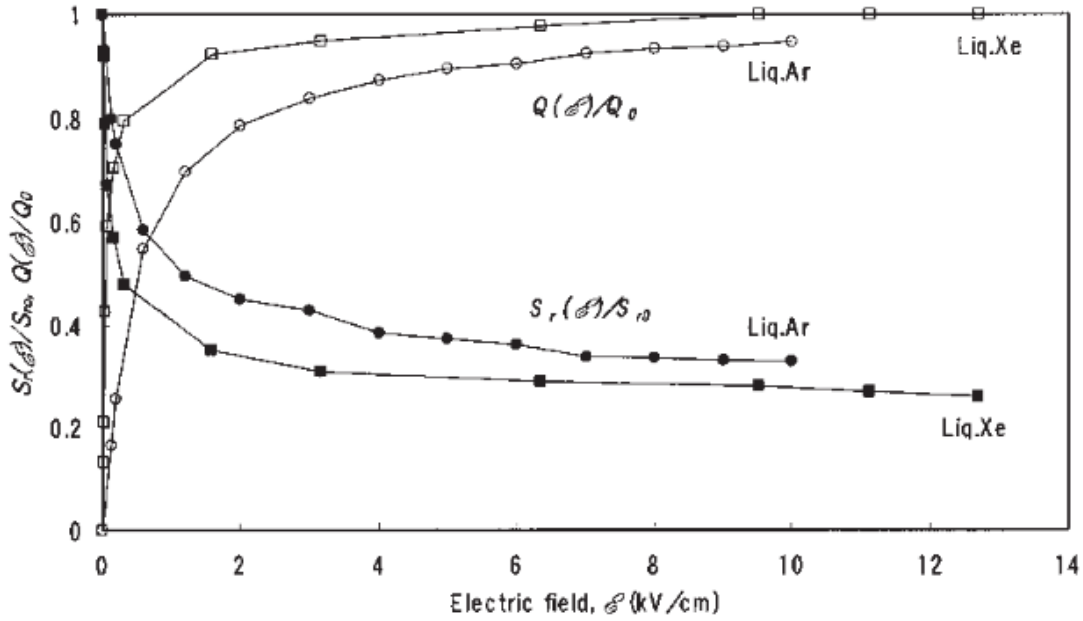


Figure 13 – Graphic of the generated charge and number of generated photons (both normalized) in function of the applied electric field [10]

For the figure 13 it is possible to notice that as the electric field increases, the process of scintillation decreases, since there are more electrons escaping from the recombination process. At the same time the collected charge increases, for the same reasons, more electrons are drifting along the Argon.

The pure argon is transparent to its own scintillation light, since the energy emitted by photon is equal to:

$$E_{cint} = \frac{hc}{\lambda_{cint}} = 9.69eV \quad (3.9)$$

The first excited level, however, have a energy of 11.55eV. But when the argon shows impurities (like nitrogen, for example), the proton is absorbed, mitigating the luminosity signals. In fact, the LAr is extremely sensible to impurities.

3.2.2 Argon and Neutrinos

When the neutrinos arrives in the region filled with Liquid Argon it can interact with the argon's atoms or with his electrons with different interaction channels.

The different types of interaction are shown in the feynman diagrams in figure 14. The interactions give energy to protons and neutrons, but also produces electrons and muons.

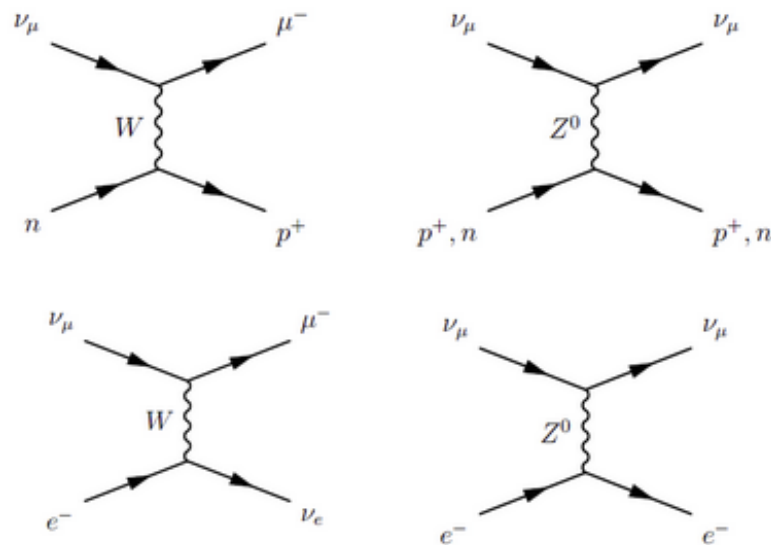


Figure 14 – Channels of interaction of neutrino in liquid argon

The particles generate will be drifted to the grids in the LArTPC (3.2), and those particles while travelling in the Argon will generate scintillation light 3.2.1, that can be detected in the Photon Detection system 3.3. The applied electric field controls the proportion of charge detect with the photon detect as seen in figure 13. So the LArTPC must have an electric field that is good enough to drift the charge, but not too strong to kill the scintillation light.

The argon being a noble gas explain the reason to choose it to make the electrons originated from the neutrinos reactions travel in it, since the argon is noble it wont absorb the electron. But do not explain why to choose the argon over another noble gases.

The reason are summarized in table 4. In the table we can see that the loss of electron energy per length travelled in argon is 2.1 MeV/cm. At same time that is less than kryptonium and xenon, but is higher than neon and helium. Meanwhile the number of photons produced per MeV deposited in LAr is 4000, which is better than Neon and Helium, but worse than Xenon. So argon is in the middle term in relation of electron drift and photon scintillation.

At the same time its needed a lot of scintillator to detect neutrinos, so for this reason the material with high density is better, since with same quantity of volume more

mols of the noble gas are in the active volume. In table 4 we see that argon have a density of $1,4 \text{ g/cm}^3$, more than neon, but less than kryptonium.

So the argon have mid terms properties in relation of the other possible candidates scintillators. So the main reason to choose the Argon is the price and abundance, since it's the noble gas with more quantity in the atmosphere (around 0.9 %).

Elements	Helium	Neon	Argon	Kryptonium	Xenon	Water
Boiling temperature [K] 1 atm	4.2	27.1	87.3	120	165	373
Density g/cm^3	0.125	1.2	1.4	2.4	3.0	1
Scintillation wavelength [nm]	89	78	128	150	175	X
Scintillation yield [γ/MeV]	19000	30000	40000	25000	42000	X
dE/dx [MeV/cm]	0.24	1.4	2.1	3.0	3.8	1.9

Table 4 – Noble gases and water properties [42]

3.3 Photon Detection System

The Photon Detection System (PDS) its responsible for reading the scintillation light coming from the neutrinos interaction with the LAr in the interior of LArTPC. The system is made of 120 PMTs and 192 X-ARAPUCAs located behind the two anode frames. So in each frame there is half of the cited numbers. The PDS system can be seen in figure 15.

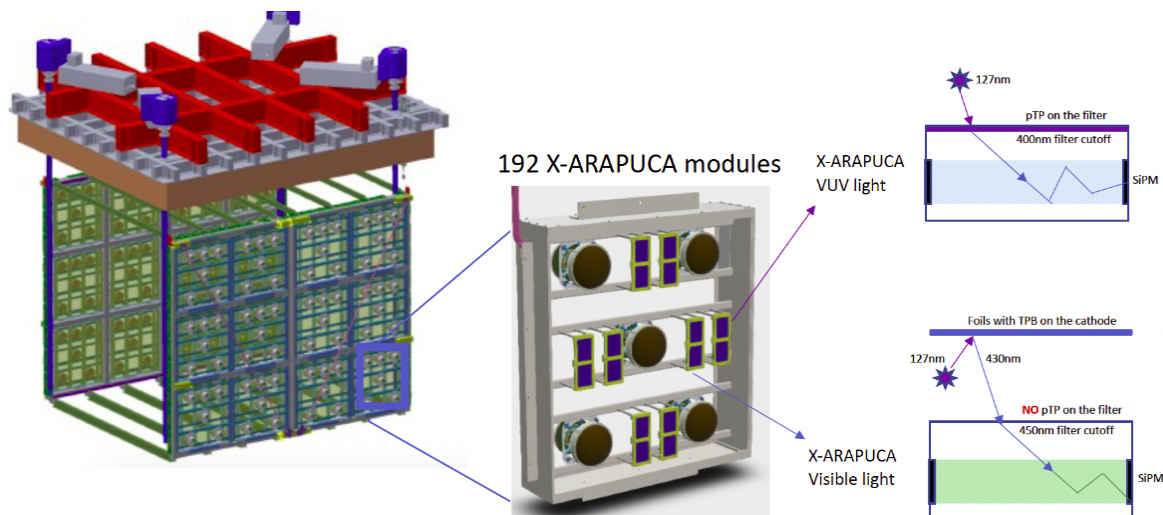


Figure 15 – PDS system

From 96 of the PMTs have TPB coated in his acceptance window and the other

24 PMTs don't have the TPB material. The PMT's in question are the 8" HAMAMATSU R5912-mod.

In the cathode plan, there is TPB foils that convert the 127nm scintillation photons to 430 nm. For this reason, the X-ARAPUCAs are also divided into two types, as seen in figure 15. Half of them (98) is to catch the UV photons, so they are the traditional models explained in 3.3.1 containing the PTP layer in the dichroic filter, this with a cut-off wavelength of 400 nm. Meanwhile the other don't have the PTP material and the cut-off wavelength is 450 nm. The reason for the higher cut-off is because the 430 nm photons must be allowed to enter the X-ARAPUCA.

But this is not the only difference between the X-ARAPUCAs, since 176 of them are the DAPHNEs X-ARAPUCAs and the other 16 are the APSAIA X-ARAPUCAs. More details are shown in figures 16, 17 and in sections 3.3.2.1 and 3.3.2.2. The distribution in each side are shown in the last figure the APSAIA X-ARAPUCAs are the 8 inside the green rhombus. The red ones in the figure are the visible light X-ARAPUCAs and the blue ones the UV version. So UV and visible light X-ARAPUCAs always comes in pair, one in side of the other.

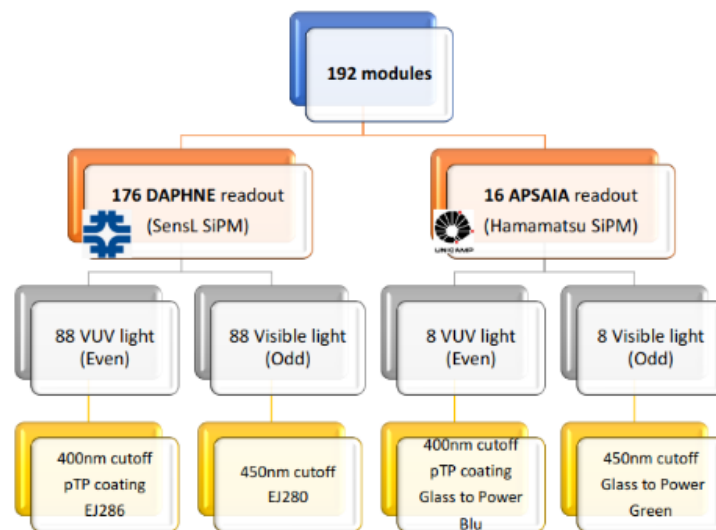


Figure 16 – Differences with the DAPHNE and APSAIA X-ARAPUCAs

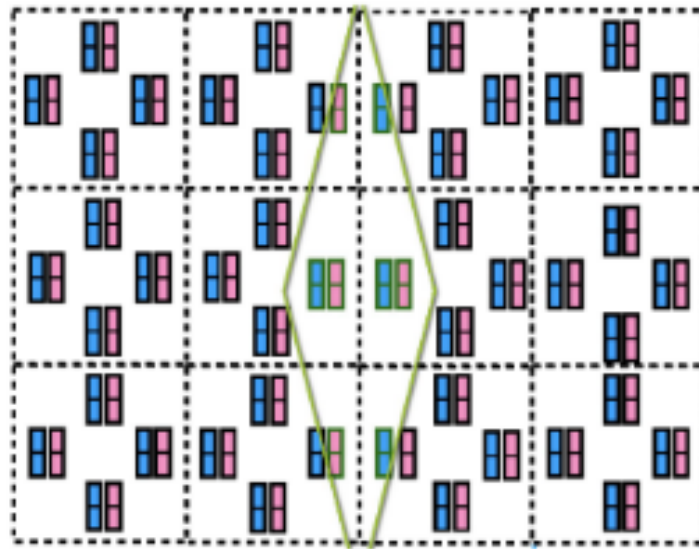


Figure 17 – Distribution of the X-ARAPUCAs on each side of the LArTPC

Each square in the figure 17 its called PDS box and contains 8 X-ARAPUCAs and 5 PMTs. There is in total 24 PDS box, 12 in each side.

3.3.1 ARAPUCAs

The X-ARAPUCA is a device developed by the physicists Ana Amélia Bergamini Machado and Ettore Segreto to detect the scintillation light in argon. This device will be utilized in experiments like DUNE (Deep Underground Neutrino Experiment), SBND (Short Baseline Neutrino Detector) and Proto-DUNE.

The X-ARAPUCA is more compact, requires a smaller power supply in relation to other photomultipliers and have better efficiency to photon detection.

To better understand how the X-ARAPUCA works, first will be explained how the ARAPUCA, the previous version o the device, works. The X-ARAPUCA will be explained then in 3.3.1.2.

3.3.1.1 ARAPUCA

The ARAPUCA is a acronym to Argon R&D Advanced Program at UniCamp, [11], at the same time that the name arapuca comes from the traps developed by the Indigenous tribes in South America to hunt small animals like birds and rabbits. The name is not a coincidence, since the ARAPUCA catches the photons that came from scintillation in liquid argon and keep them trapped until they are collected by active light

sensors - the SiPMs (Silicon photomultipliers). The SiPMs working principle are explained in appendix D.2.

The ARAPUCA is a box with highly reflective internal walls that have a dichroic filter, two organic scintillators and a SiPMs in its interior. In the figure 18 it is shown a illustrated scheme of the device.

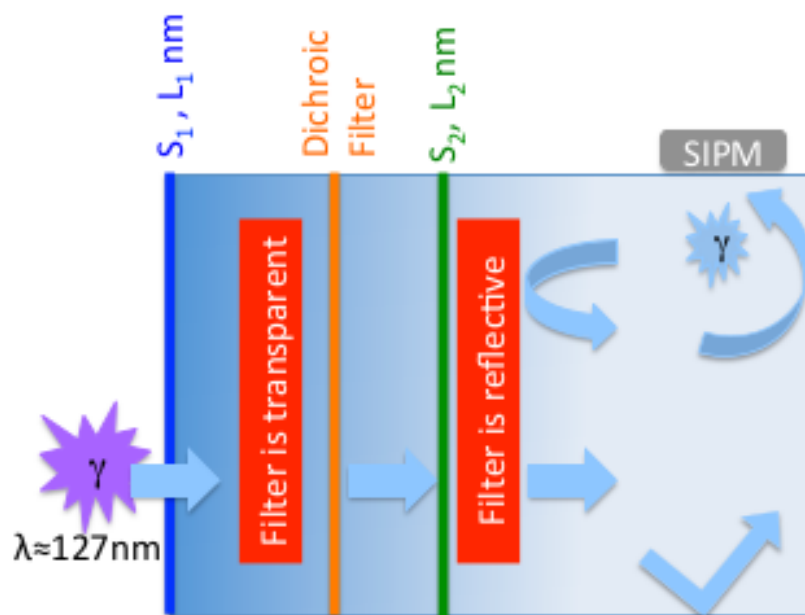


Figure 18 – Illustrated scheme of the ARAPUCA, S1 is the first organic scintillator and S2 is the second organic scintillator [11]

A dichroic filter is a material made of several layers with distinct reflection indexes. Due to the difference of the optical paths described by each one of the reflective rays and transmitted between layers it causes certain wavelengths to be transmitted, while others are reflected.

In the case of the ARAPUCA, the dichroic filter is a lowpass filter with cutoff wavelength equals to 400 nm, in other words, wavelength above that value are reflected and bellow that value are transmitted. It has a transmittance of 95 % to wavelength below 400nm and reflectance above 98 % to photons with wavelength greater than 400 nm. In the figure 19 it is shown the transmittance and reflectance spectrum of the dichroic filter for both distinct types of polarization.

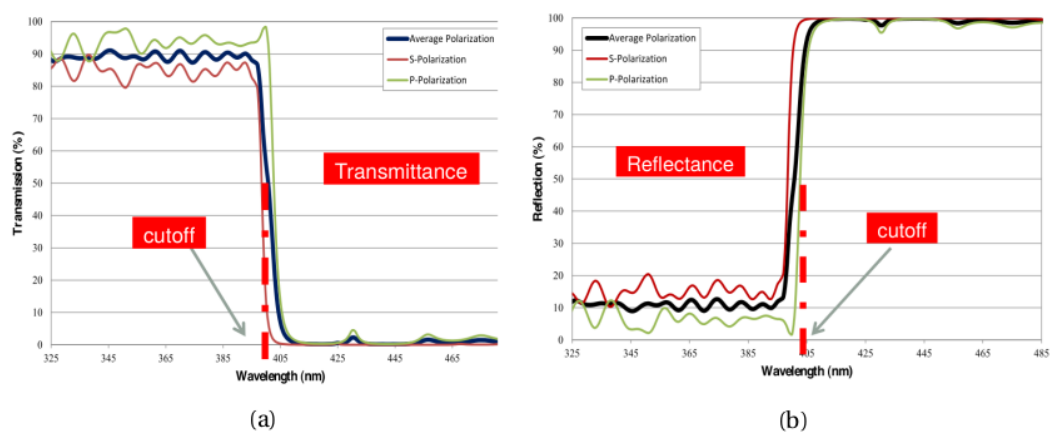


Figure 19 – Transmittance and reflectance spectrum of the dichroic filter [12]

The organic scintillators (WLS) utilized are the para-terphenyl (PTP) and the Tetraphenyl-butadiene (TPB). The chemical structures of both compounds are shown in 20 and 21. More information in E.



Figure 20 – Para-terphenyl(PTP) [13]

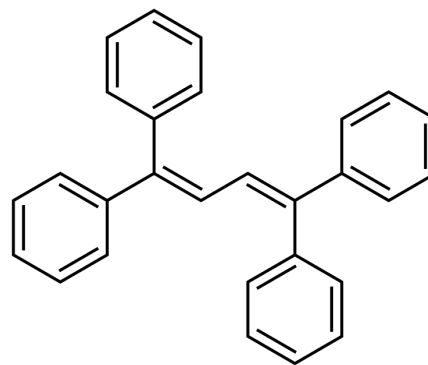


Figure 21 – Tetraphenyl-butadiene (TPB) [14]

In the figure 22 is the PTP luminescence spectrum. In the figure, can be observed that the emission peak is located approximately in 340 nm.

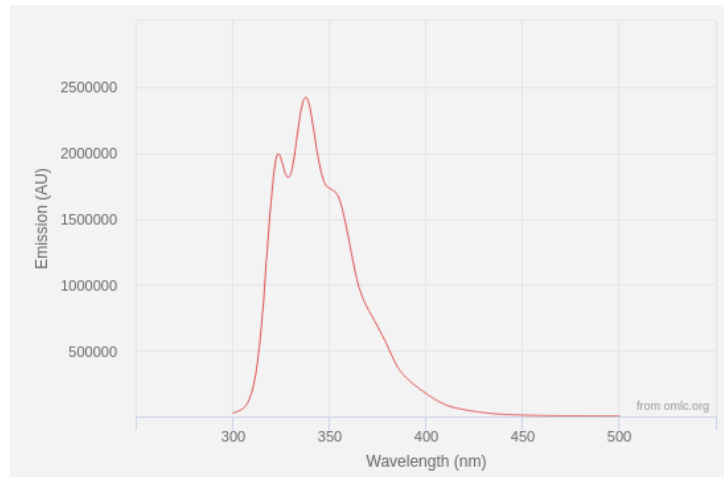


Figure 22 – PTP's luminescence spectrum [15]

Research shows that the efficiency rate of the conversion of a 127 nm photon originated in liquid argon scintillation to the range of 340 nm, when absorbed by PTP is very close to 100% [11].

The TPB shows the absorption spectrum shown in figure 23. In the figure, can be observed that the TPB shows a absorption peak in the value of a wavelength value close to 340 nm, what is the exact value emitted by the TPB.

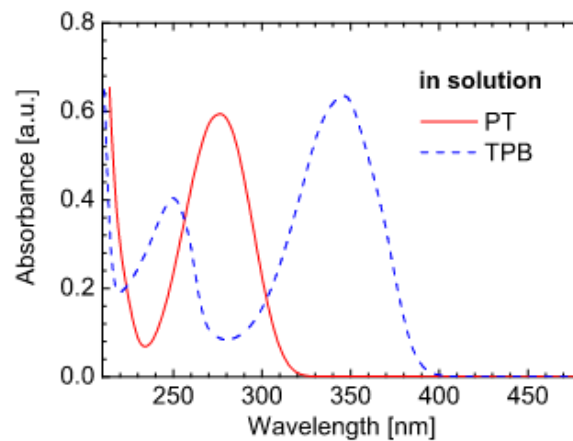


Figure 23 – TPB's Absorption spectrum [16]

In the figure 24, it is shown the TPB fluorescence spectrum. In the figure, again, is possible to observe that the material's fluorescence peak is close to 430 nm. The

efficiency rate of the TPB conversion of a 350 nm photon to a 430 nm is approximately 80%.

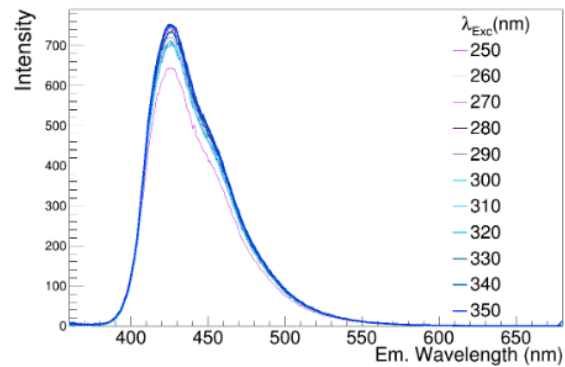


Figure 24 – TPB's fluorescence spectrum [9]

Both TPB and PTP, for this ability to convert a spectrum to another, are called wavelength Shifter (WLS).

The probability of a scintillation photon to pass through a window is given by the equation 3.10.

$$\epsilon_{window} = \frac{p_{PTP}}{2} p_{TPB} \cdot p_{dichroic} \approx 0.5 \times 0.8 \times 0.95 = 0.38 \quad (3.10)$$

In equation 3.10 the term PTP is divided by two because the reemitted photon can be emitted in arbitrary directions, therefore, only half of the photons go towards the inside of the ARAPUCA.

In the inner region of the ARAPUCA is placed - on the walls - the VIKUITI ESR, this material has a reflectivity of 100% to wavelength greater than 400 nm, as shown in figure 25.

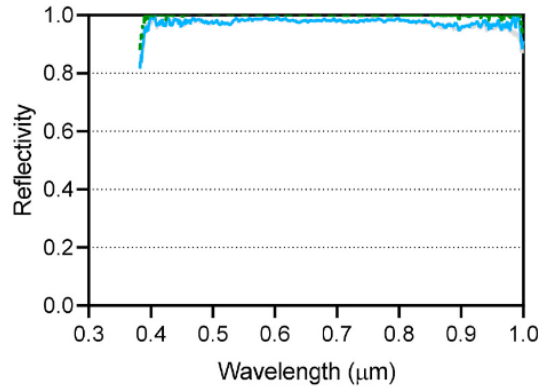


Figure 25 – VIKUITI ESR's reflectivity spectrum [17]

With everything explained, is easier to comprehend how the ARAPUCA works. The 127 nm photon, originated in LAr scintillation, when reaching the acquisition window of the ARAPUCA arrives in the S1 layer of the PTP - in figure 18 - is reemitted with a wavelength of 350 nm. This photon pass through a dichroic filter, that blocks photons with wavelength greater than 400 nm, then upon arriving TPB (S2 layer) it is converted to 430 nm. The photon, in this process, is reemitted and can go in two directions: towards the dichroic filter and towards the cavity of the ARAPUCA. The photons that goes towards the dichroic filter is reflected by it, being directed towards the inside of the ARAPUCA.

The photons stay in the inner region of the ARAPUCA being reflected by the VIKUITI until reach the SiPM's window. The ideal is that the chosen SiPM has a high quantum efficiency around that wavelength (more details in D.2).

When the photon arrives the interior of the ARAPUCA it has a f probability of reaching the SiPM's window and $(1 - f)$ of not reaching the window right at the beginning, in which f is the ratio of the area covered by the SiPM's windows with the total inner area of the ARAPUCA. The $(1 - f)$ photons that does not reach the window, will be reflected by the VIKUITI with a efficiency of almost 100 % and by the dichroic filter with probability equal to R . And, this way, the cycle restart.

Therefore, the inner efficiency of the ARAPUCA can be calculated as the sum described by the equation 3.11.

$$\epsilon_{inner} = \sum_{i=0}^{\infty} f(1 - f)^i R^i = \frac{f}{1 - (1 - f)R} \quad (3.11)$$

The term f can be calculated as described by the equation 3.12.

$$f = \frac{A_{SiPM}}{A_{inner}} = \frac{\alpha \cdot 4A_{lateral}}{4A_{lateral} + 2A_{base}} = \frac{\alpha 4Lh}{4Lh + 2L^2} = \frac{\alpha}{1 + \frac{L}{2h}} \quad (3.12)$$

In which L is the width and length of the inner part of the ARAPUCA and h is its height. While α is the percentage of the lateral area covered by the SiPM's windows.

The total efficiency of the device is given by the product of the window efficiency (3.10) with the inner efficiency (3.11) with the efficiency of the SiPM (probability of the photon generate a electric sign when absorbed by the SiPM), as shown in equation 3.13.

$$\epsilon_{ARAPUCA} = \epsilon_{inner} \cdot \epsilon_{window} \cdot \epsilon_{SiPM} \quad (3.13)$$

The original ARAPUCA's efficiency is equal to 1.5 % [52] utilizing a SiPM sensL MicroFC-60035-SMT.

3.3.1.2 X-ARAPUCA

The X-ARAPUCA is an upgrade of the ARAPUCA, uniting its concepts with a light guide.

The device still have a dichroic filter, the inner walls covered with reflective materials and the external WLS made of PTP. The difference is that the second WLS, the inner TPB layer is removed from the dichroic filter, and is placed in the middle of the X-ARAPUCA one light guide already embedded with TPB. This light guide is optically coupled with the SiPM. In the figure 26 it is shown a scheme of the X-ARAPUCA.

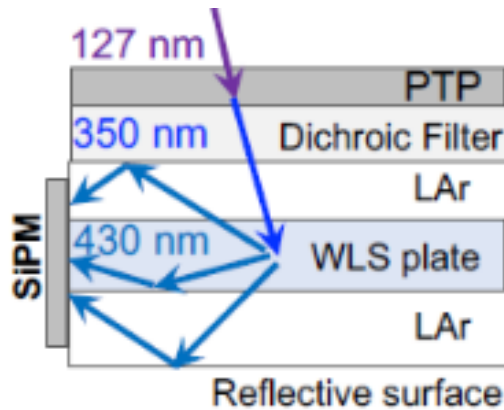


Figure 26 – Illustrative scheme of the X-ARAPUCA [18]

The Liquid argon's scintillation photon that pass through the PTP is converted to 350 nm and then crosses the dichroic filter, exactly as explained in 3.3.1.1.

When the photon arrives the light guide it is converted to a photon of 430 nm. When this photon is in the guide and argon interface, going out of the guide a total internal reflection happens once the refractive index of the argon is equal to 1,23 and the guide's is 1,5 [19]. According to the Snell-Descartes' law, the critical angle of refraction with the normal of the surface is given by the equation 3.14.

$$\theta_c = \sin^{-1} \left(\frac{n_{LAr}}{n_{guide}} \right) = \sin^{-1} \left(\frac{1,23}{1,5} \right) = 55.08^\circ \quad (3.14)$$

Therefore the photons in the inner side of the guide with an incidence angle with the normal greater than 55.08° in the guide and argon interface, suffers a total internal reflection and get trapped in its interior of the guide. Those photons keep suffering total internal reflection and reflections with the walls until they are guided to one of the SiPMs and thus being detected. This is the second detection mechanism of the X-ARAPUCA.

The first mechanism is when the incidence angle with the surface is smaller than 55.08° and the photon can get out of the guide. Since the reflection of the inner walls is specular, in other words, does not change the angle, this photon will keep crossing the guide and will be detected by the original ARAPUCA's mechanism, suffering reflections in the inner walls and in the dichroic filter until they are detected.

Therefore the photons that does not get trapped in the light guide, are the photons in the interior of the cone described by $55,08^\circ$, as shown in the figure 27.

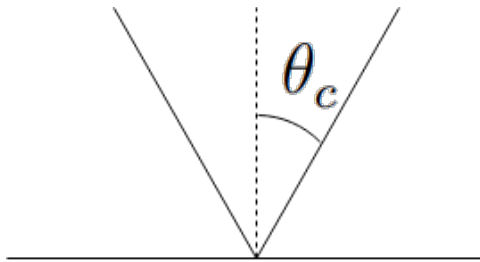


Figure 27 – Illustrative scheme of the cone that separates the photons that suffer total internal reflection and those who do not suffer

Hence the percentage of the photons that get into the light guide and does not get trapped by total internal reflection can be given by the ratio of the solid angle described by the cone and the superior total solid angle (2π), as shown in the figure 3.15.

$$\epsilon_{\bar{\theta}_c} = 1 - \epsilon_{\theta_c} = \frac{\Omega_{\theta_c}}{\Omega_T} = \frac{2\pi(1 - \cos(\theta_c))}{2\pi} = 1 - \cos(\theta_c) = 0.43 \quad (3.15)$$

Therefore 43 % of the photons does not get trapped in the light guide, while 57 % of the photons gets trapped by total internal reflection, and will be guided with greater efficiency to the SiPMs.

There is a third detection mechanism, that is when the photon of 350nm arrives for the first time in the interface with the wave guide. For greater incidence angles with the guide, the photon have better chances of being reflected. This photon will return to the dichroic filter with a big incidence angle and will be reflected by the same mechanism, once the refraction index of the filter is also close to 1.5. Hence the third mechanism is that the photons with a big incidence angle are reflected by the guide and the filter and get trapped in the superior part of the X-ARAPUCA until they are detected. These photon are not detected to a wavelength of 430 nm, once they do not get into the light guide.

In the figure 28 it is shown a diagram of three photon capture mechanism.

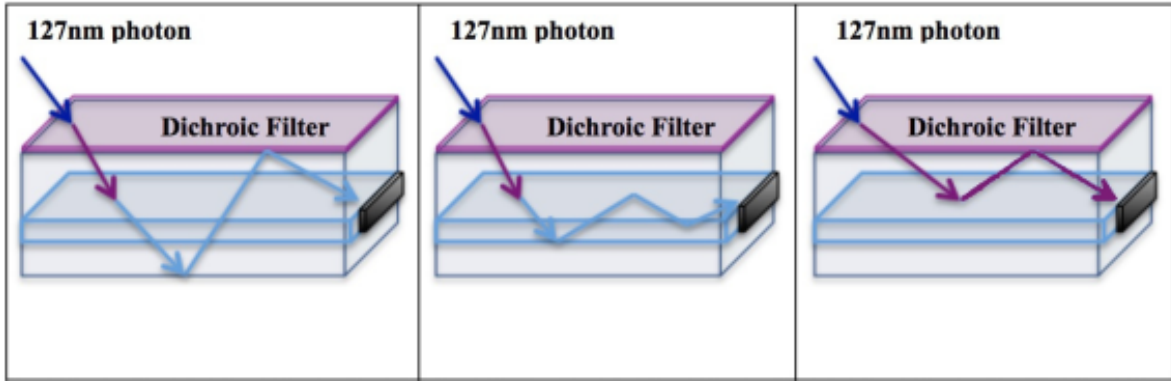


Figure 28 – Photon capture mechanism of the X-ARAPUCA [19]

The efficiency of the window in this scenario is given by 3.16.

$$\epsilon_{window_x} = \frac{p_{PTP}}{2} p_{dichroic} \approx 0.5 \times 0.95 = 0.48 \quad (3.16)$$

To calculate the internal efficiency, the efficiency of the third mechanism can be disregarded, once it is much smaller than the first two mechanism. The efficiency of the first

mechanism is the efficiency given by the equation 3.11. However the second mechanism's is given by the equation 3.11, adapting the value of f to f_{slab} and R to R_{slab} . The efficiency is given by the equation 3.17.

$$\epsilon = (1 - \epsilon_{\theta_c})\epsilon_1 + \epsilon_{\theta_c}\epsilon_2 = (1 - \epsilon_{\theta_c})\frac{f}{1 - (1 - f)R} + \epsilon_{\theta_c}\frac{f_{slab}}{1 - (1 - f_{slab})R_{slab}} \quad (3.17)$$

Hence the total efficiency is given by equation 3.18:

$$\epsilon = \epsilon_{SiPM}\epsilon_{janela_x}\epsilon_{TPB} \cdot \left((1 - \epsilon_{\theta_c})\frac{f}{1 - (1 - f)R} + \epsilon_{\theta_c}\frac{f_{slab}}{1 - (1 - f_{slab})R_{slab}} \right) \quad (3.18)$$

The term f is given by the equation 3.12, while the term f_{slab} is given by the equation 3.19.

$$f_{slab} = \frac{A_{SiPM}^{slab}}{A^{slab}} = \frac{\alpha \cdot 4A_{side}^{slab}}{4A_{side}^{slab}} = \alpha \quad (3.19)$$

In the equation 3.19, α has the same value of the equation 3.12, because the SiPM has the same height (h) of the internal volume, hence the occupation rate of the surface in relation to the total inner surface and the internal surface of the guide's bar is the same. The difference between the first and second mechanism equations are the bases, since the photon trapped in the interior when arriving the bar suffers total internal reflection, and therefore this area does not matter for the calculation of the total effective area.

Hence the ratio of the efficiency of the X-ARAPUCA with the original ARAPUCA can be given by the equation 3.20, assuming that R and R_{slab} are approximately equal.

$$\frac{\epsilon_X}{\epsilon} = (1 - p_{\theta_c}) + p_{\theta_c} \cdot \frac{\epsilon_2}{\epsilon_1} \quad (3.20)$$

For the ratio 3.20 be greater than 1, it is necessary that $\frac{\epsilon_2}{\epsilon_1}$ is also greater than 1. The efficiency of the X-ARAPUCA is equal to 3.5 % [53], greater than the original ARAPUCA.

3.3.2 Data Acquisition System

This section will talk about the data acquisition system of the photo detection system.

3.3.2.1 APSAIA

The UV APSAIA X-ARAPUCAs use an 400 nm cutoff wavelength dichroic filter from OPTO (Optical Glass substrate) with a substrate of PTP coated and uses the wavelength shift bar BLU from Glass to Power [54].

Meanwhile the light visible ones uses 450 nm cut-off wavelength dichroic filter also from OPTO and the wavelength shift bar GREEN from Glass to Power.

Each X-ARAPUCA have 4 SiPMs boards, more precisely 2 pairs of 2 SiPMs in parallel totalizing two outputs from ARAPUCA. The SiPM utilized are from Hamamatsu [29]. The two of the top on each side (four in total) are the model S14160-6050-HS with breakdown voltage of 38V at 25°C and gain of 2.5×10^6 . This SiPMs increases (or decreases) his breakdown voltage with the rate of $34mV/^\circ C$. The other X-ARAPUCAs use the S13360-6050-VE with 53V of breakdown voltage and a gain of 1.6×10^6 . In figure 123 are shown the photon detection efficiency of both SiPMs. The variation of breakdown voltage due to temperature of this SiPM is $54mV/^\circ C$

But what give the name to this system is the readout electronics: the APSAIA. The APSAIA is an amplifier developed to the ARAPUCAs responsible for amplifying the output signal of the X-ARAPUCAs and also giving to them the proper bias. The APSAIAs SBND are shown in figure 29.

The APSAIA is an acronym to ARAPUCA Power Source And Input Amplifier.

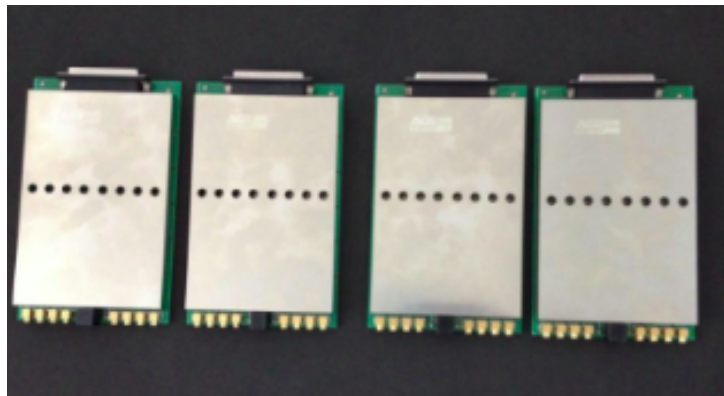


Figure 29 – The 4 APSAIAs of SBND

Each APSAIA have 8 amplifier inputs, so in the total there is $8 \times 4 = 32$ inputs. There is 16 APSAIAs X-ARAPUCAs, each with 2 outputs, totalizing 32 outputs. Also to each amplifier input there is an high voltage output to the SiPMs. The output amplified signal goes to 2 CAEN V1730 digitizer, each one with 16 input with 14-bits of ADC. This

digitizer is capable of sample with a frequency of 500MHz.

The APSAIA is powered up with 12V and have a typical current of 400 mA. The schematic of the amplifier system and supply voltage system are shown in figures 30 and 31.

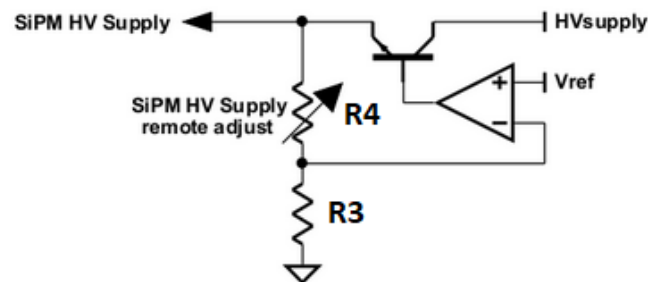


Figure 30 – High Voltage Supply electric schematic of APSAIA

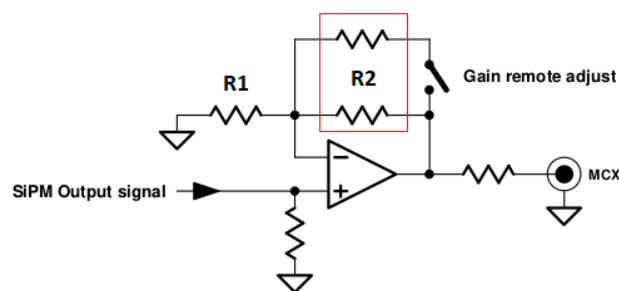


Figure 31 – Amplifier electric schematic of APSAIA

The high voltage output is adjustable from 20V to 60V with resolution of 100 mV. Who controls this HV supply is an internal microcontroller. The HV supply input in the figure 30 is 60V. The microcontroller remote adjust the potentiometer in the figure 30 and the V_{ref} to adjust the output to the user required voltage. The operational amplifier acts as an comparator, activating the transistor when the V_{ref} is greater than $HV \cdot \frac{R_3}{R_3 + R_4}$. When this happens the high voltage appears in the output. At this moment the voltage in the negative terminal of the op amp becomes higher than V_{ref} , switching off the transistor. This switching game is what makes the control of the output high voltage.

The amplification block have a 50Ω input impedance (the resistor connected to the positive terminal of the op amp). The op amp is operating with negative feedback and due to virtual short the gain is 3.21.

$$G = 1 + \frac{R2}{R1} \quad (3.21)$$

The gain can be remotely adjustable via the μC closing the switch of figure 31. When the switch closes the R2 becomes smaller, and the gain decreases. The gain can be 20 or 40 (13.01dB or 16.02dB).

The output impedance is the resistor further to the right in the figure 31 and its value is 50Ω , to do the impedance matching in the digitizer that also have an input impedance of 50Ω . The APSAIA is suitable for processing 30 ns rise-time signals, and has an output voltage range of 2V (positive or negative), and can handle 2A.

The input signal and output DC high voltage are in the DB37 connector, that connects to the flange in warm side of system as shown in figure 32.

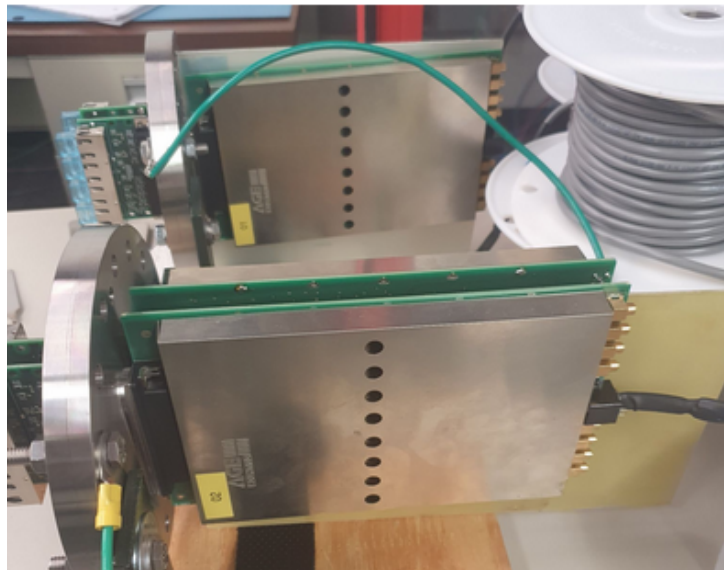


Figure 32 – The APSAIAs connected to the flange

In the other side of the flange (cold side) there is AAPI board that use RJ45 inputs that comes from the X-ARAPUCAs and convert to DB37 to connect in the flange and as consequence in the APSAIA board.

This flange are going to be on put on top of the LARTPC in the lateral feedthrough (in blue) shown in figure 33.



Figure 33 – The APSAIAs connected to the flange

The output amplified signal elears in the 8 MCx connectors shown in figure 29 (the yellow ones). The RJ11 is where the APSAIA receives the power voltage of 12V and the communication with the internal μC of the board, where the configuration are made.

The block diagram of the system is shown in figure 34. Each digitizer have a dedicated DAQ server connection and uses the private fiber optic protocol CONET.

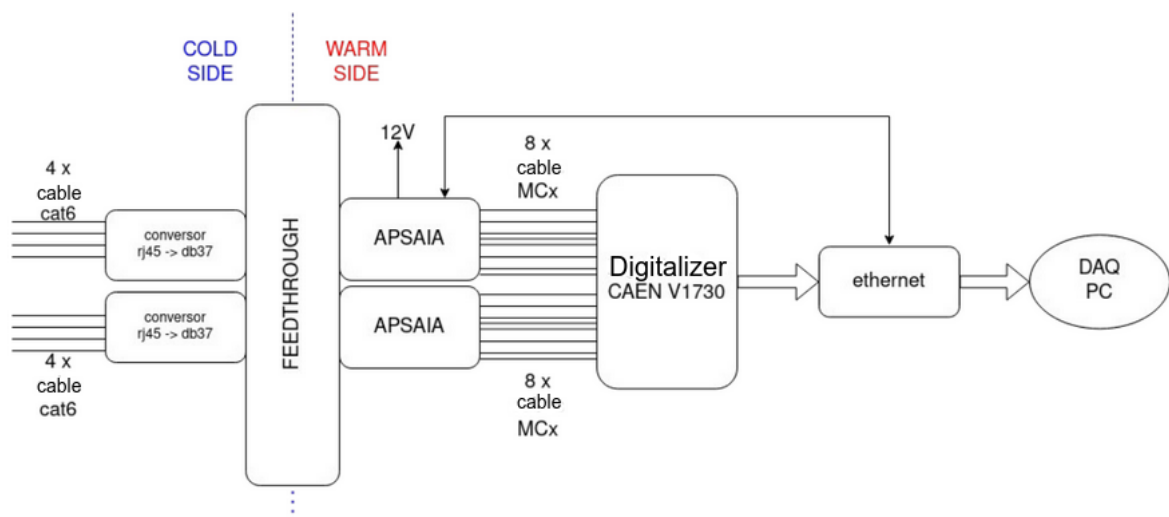


Figure 34 – Block diagram of the APSAIA readout electronics

3.3.2.1.1 APSAIA Test Stand

The APSAIA Test Stand is located at D0 assembly building at Fermilab. The schematic of the setup is shown in figure 35.

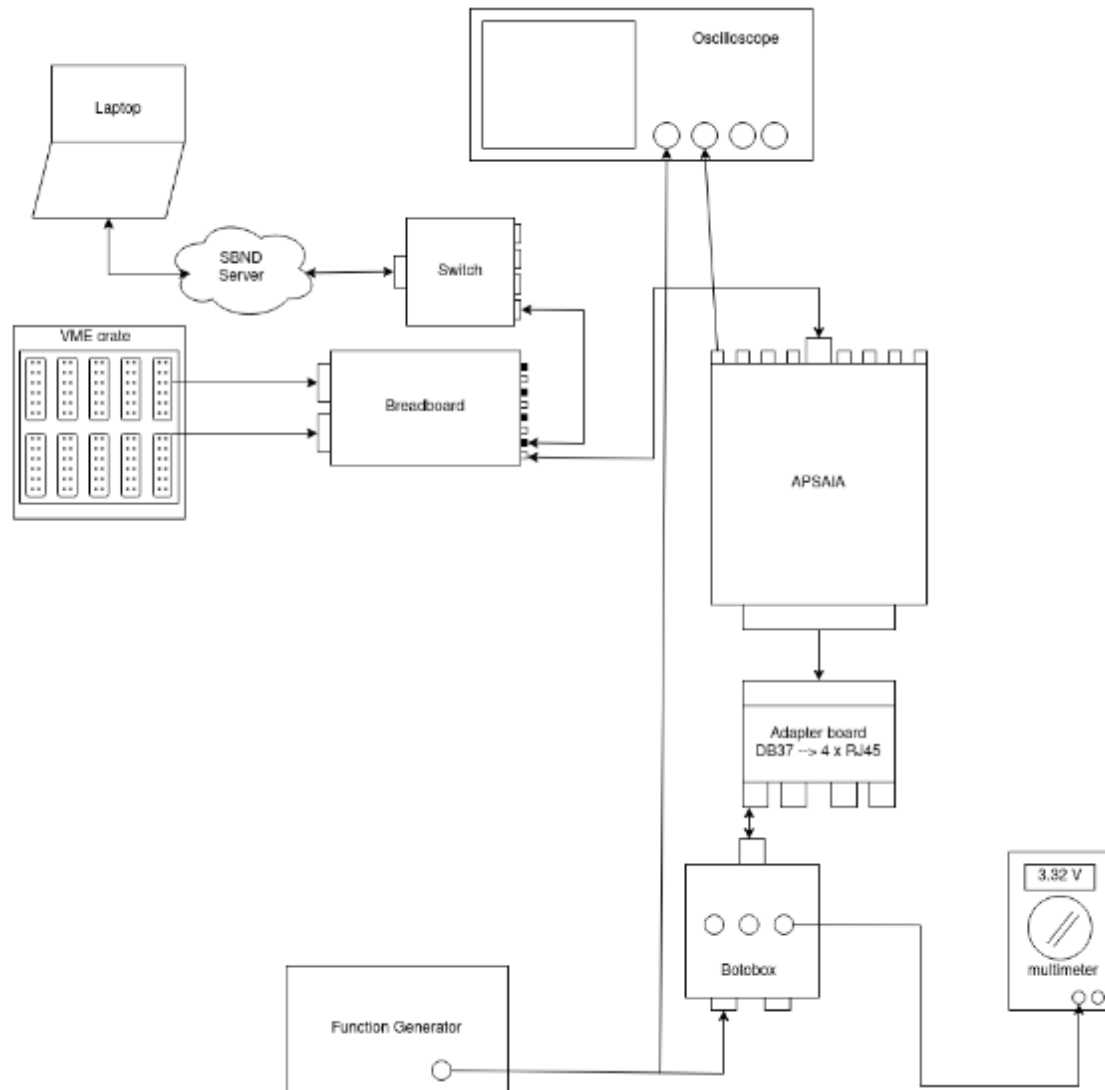


Figure 35 – Electric schematic of the setup

The made breadboard, shown in the figure 36 is responsible for supplying 12V to all the APSAIAs. In figure 36, the 4 power barrel connectors connect the breadboard to the switch shown in figure 37, and the LEMO connectors connect the breadboard to the APSAIA. The breadboard is connected to one of the existing VME crates at D0. There is also a 2A fuse in the board, to protect from high current coming from the crate.

The boards have 5 fuses: one of 2A near the VME pins, and 4 of 3/4A in each APSAIA connection.

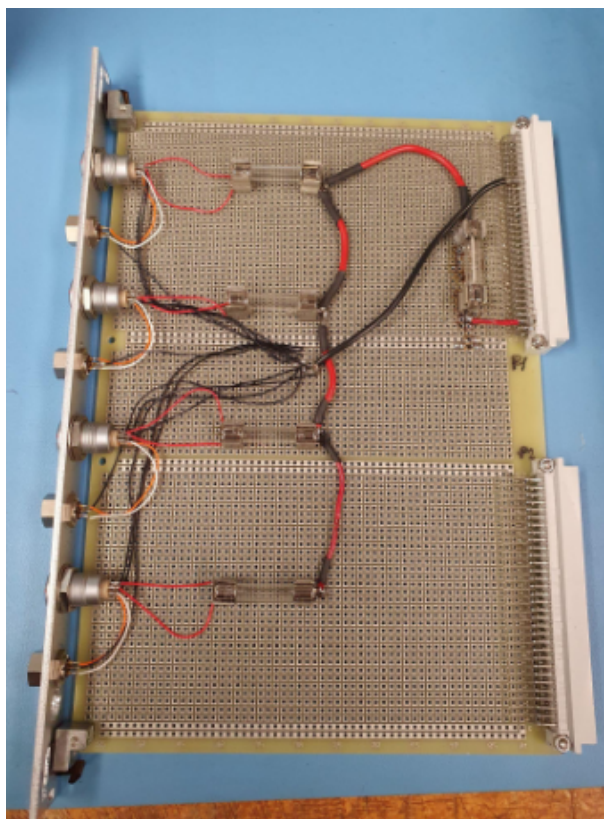


Figure 36 – Breadboard made to power supply all the APSAIAs and communicate them to the SBND server

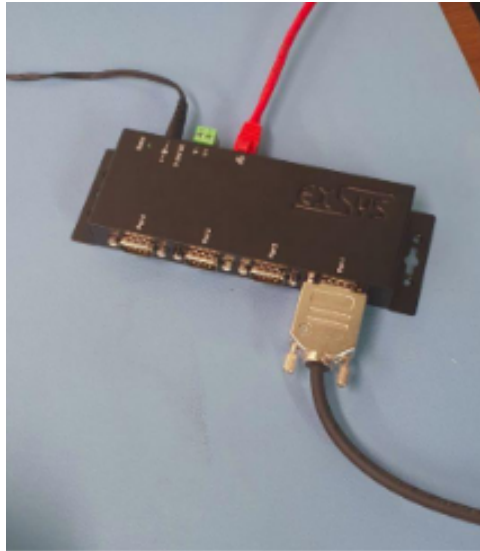


Figure 37 – Switch utilized to communicate the APSAIAs to the server

The connection is made by the 4 port RS232 switch shown in figure 37, with a single network connection serving the four APSAIAs. To communicate with the APSAIA a personal computer connected to the network was used.

The adapter board shown in figure 35 is the AAPI board already mentioned. To read the high voltage output and to send the signal from oscilloscope to the input of the amplifier was first intended to use an adapter board that converts the port RJ45 to 9 independent cable/connector. The adapter is shown 38. But this board, since it is not shielded, was injecting a lot of noise in the setup. To solve this problem a little metallic box was made, called Botobox. The Botobox has an RJ 45 connector, 3 female banana connectors for reading the high voltage output of the APSAIA, and finally 2 BNC connectors for input signals. The figure 39, shows the box made for the setup.

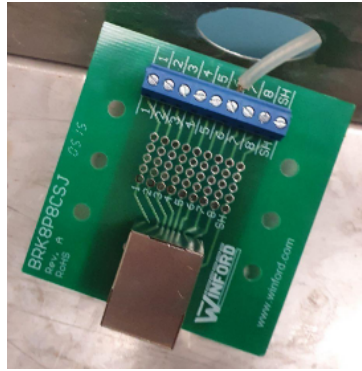


Figure 38 – Adapter board
from 8 wires to
RJ45

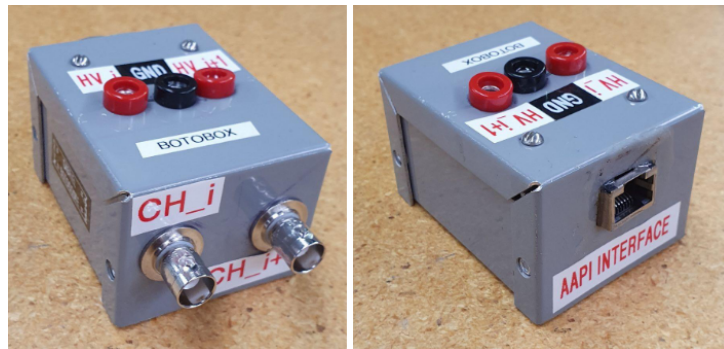


Figure 39 – Botobox

Using a wave generator, it was defined a square pulse with $500 \mu\text{s}$ of duration and amplitude of 10mV to test the gain of the two possible gain configuration. This pulse was inserted in the APSAIA amplifier input. The wave amplified with low and high gain is shown in figure 40. In yellow (ch1) is the input wave and in blue (ch2) the output wave. It was used a impedance matcher in the BNC connection between the cable and oscilloscope, since the cable is cable is 50Ω and the input impedance of the scope is $1\text{M}\Omega$. The low gain is 20 and the high gain is 40, as already mentioned.

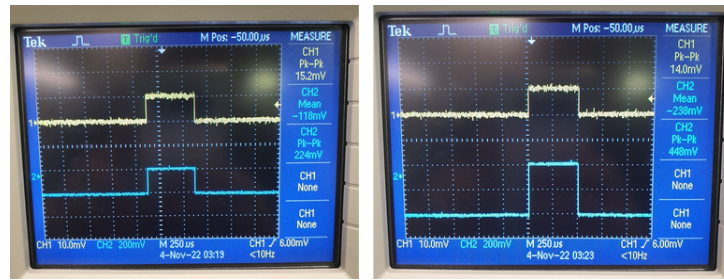


Figure 40 – APSAIA gain configuration. Left: Low Gain Right: High Gain

The gain in function of the signal frequency was also tested and the results are shown in table 5. The cut-off frequency (where the gain is $20/\sqrt{2}$) happens between 10MHz and 15MHz, near 11.7MHz.

Frequency (Hz)	Gain	Gain (dB)
10	20.24	26.12
100	20.39	26.18
1k	20.39	26.18
10k	20.2	26.12
100k	20.0	26.02
1M	19.8	25.93
10M	16.8	24.42
15M	6.47	16.11

Table 5 – Frequency Response

The bode plot is shown in figure 41. So the gain-bandwidth product of the APSAIA is $20 \cdot f_{cut} \approx 234 \times 10^6$. So the cut of frequency for the high gain configuration is half of 11.7MHz, that is 5.85 MHz.

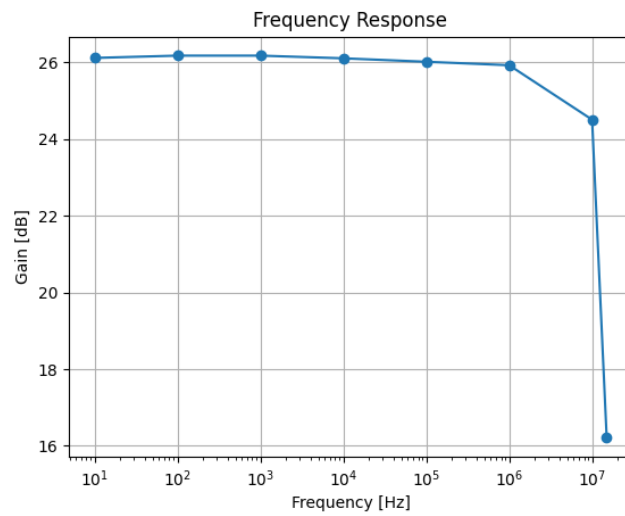


Figure 41 – Bode plot of the frequency response of APSAIA

The delay in the APSAIA response also was tested and are show in figure 42. The delay in response is 36 ns.

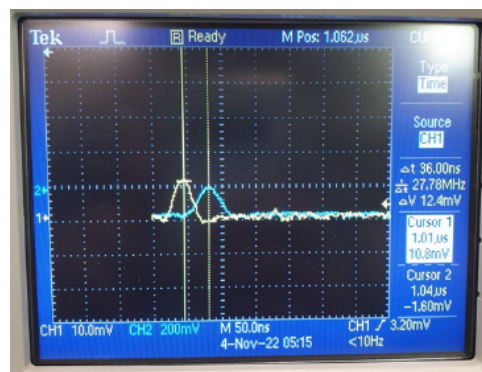


Figure 42 – APSAIA delay, in yellow the input signal in blue the output signal

So using all this information its possible to estimate the transfer function of the system in the Laplace domain, and is shown in equation 3.22.

$$H(s) = \frac{G}{1 + \frac{s}{2\pi f_{cut}}} e^{-st_{delay}} \quad (3.22)$$

3.3.2.2 DAPHNE

The UV DAPHNE X-ARAPUCAs use an 400 nm cutoff wavelength dichroic filter with PTP and the wavelength shift bar EJ286 from ENJEN [28]. Meanwhile the light visible ones use 450 nm cutoff wavelength dichroic filter and the wavelength shift bar EJ280 from ENJEN.

In this X-ARAPUCA there are also 4 SiPMs board, but in this case, there are four output channel. The SiPMs used in the DAPHNE system are MICROFC 30050-SMD from ONSEMI [55]. The gain of this SiPM is 6×10^6 and it have a breakdown voltage of 21.5V. The variation of that voltage with temperature is $21.5 \text{ mV}/^\circ\text{C}$.

Differently from APSAIA, there is no readout electronics in the flange that connects the warm side with the cold side. The wires get out from the cold side from the superior feedthrough (red one) show in figure 33.

The interface boards are the CASTOR and POLLUX boards, respectively for the cold and warm side. A schematic of those boards are shown in figure 43. The CASTOR is responsible to read the signals from SiPMs making the conversion from RJ-45 to db37. The POLLUX makes reverse procedure. Then the data is converted to HDMI.

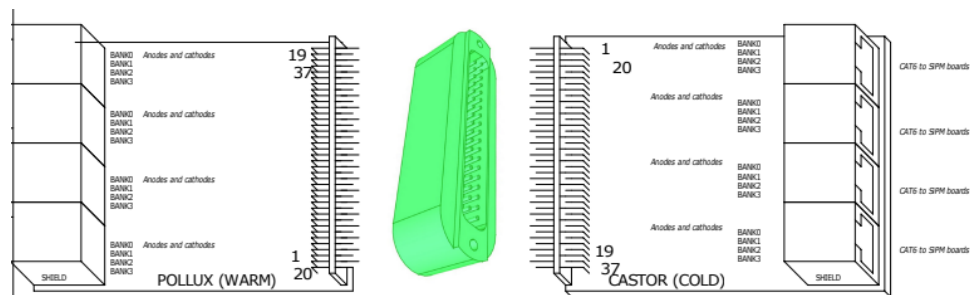


Figure 43 – Interface boards of the DAPHNE system (Jon Ameal)

DAPHNE is acronym to Detector electronics for Acquiring PHotons from NEutrinos. The electronics is based on the the electronics of the Cosmic Ray Tagger of the experiment mu2e, with the adequate modifications since the SBND PDS needs to read much more data. The DAQ of the DUNE and the ProtoDUNE are based on the DAPHNE system too. The system is composed of the controller and 12 Front End Board (FEB).

The FEB consists of 8 5807 TI ADC chips of 12 bits (80MHz), 4 Spartan 6 FPGAs, 4 LPDDR memories, and a Texas Instruments microcontroller. The FEB is responsible for digitizing the signals from the SiPMs. Each FPGA reads two ADCs and since each ADC has 8 channels, this corresponds to 16 channels per FPGA. Since each

FEB has 4 FPGAs, this corresponds to 64 ADC channels per FEB. The FEB can be seen in figure 44. The future aim is to upgrade the SPARTAN 6 FPGA to the SPARTAN 7.



Figure 44 – DAPHNE Front End Board

Each FEB have 16 HDMI input, so in total there is $16 \times 12 = 192$, more than enough to read the 176 DAPHNEs X-ARAPUCAs.

The Controller is in charge of providing trigger signals to the FEBs, collecting data from them, and transmitting the information to the server. This apparatus is made of four FPGAs, a microcontroller, three LPDDR memories, and an Ethernet chip, as shown in figure 45. The ethernet chip used is the Zest ETM 1, produced by Orange Tree. Although the Controller can retrieve data from 24 FEBs, only 12 of them are employed in SBND.

Of the four FPGAs, one is designated as FPGA 1 or APEX FPGA, while the other three are referred to as FPGA 2. The APEX FPGA communicates with the Ethernet chip and reads information from the FPGA 2s and send data over the ethernet, while the FPGA 2s receive data from the FEBs, store it in the memories, and transmit it to the APEX FPGA. Each FPGA 2 obtains data from eight FEBs ($24/3 = 8$).



Figure 45 – DAPHNE Controller

Since there is 64 ADC channels per FEM, and there is 12 FEM, in total there is 768 ADC channels. Each ADC is responsible for generating an 256 bit word. So in total the full event is 193536 bit long. This is much bigger than the FPGA buffer capability

(50000). The solution developed by Daniel Mishins was to split the read-out in four times as explained in the next paragraph.

When the controller receives an trigger request, it send an trigger to all the FEBs connected. The controller FPGA APEX first reads the data coming from the first FPGA of the FEB connected in the FPGA2(1), then reads all the data from the first FPGA of the FEBs connected to the FPGA2(2) and them the same thing for the FEBs connected to the the FPGA2(3). Then do it again for the second FPGA of the FEB, then for third and for the last the fourth.

Since the DAPHNE uses FPGA in can work fast with a lot of parallel digital data. The schematic of the setup is shown in figure 46.

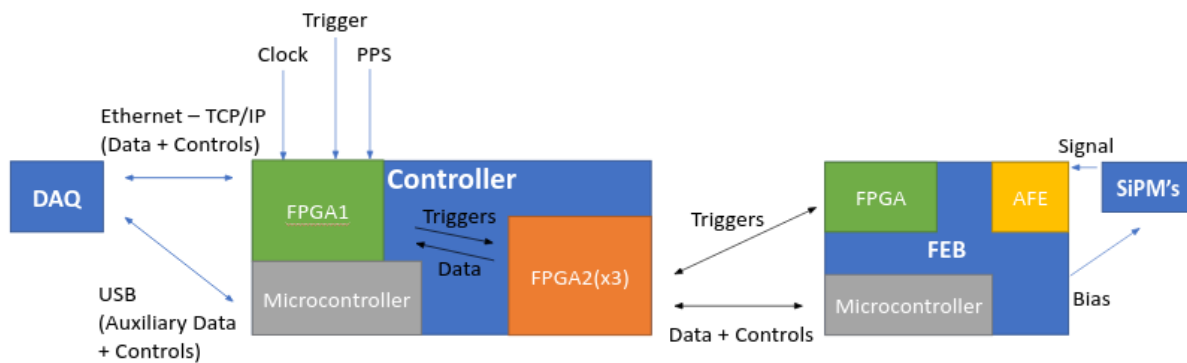


Figure 46 – DAPHNE setup Diagram (Daniel Mishins)

3.3.2.2.1 DAPHNE Test Stand

The setup is found at the 14th floor of Wilson Hall in Fermilab. To program and compile the VHDL script to SPARTAN 6 it is needed the program ISE from Xilinx. However this program is old and not receive more updates. So for this reason it was installed the operational system Scientific Linux 6 (SL6).

It was connected two FEMs in the controller, and to communicate with it, it was used the software MINICOM that allows serial communication. The main problem is that the MINICOM don't work properly with SL6. The issue isn't fully solved, but one thing that help is the command *stty* in terminal.

In minicom its necessary to set the baudrate to 460800, 8 bit data, odd parity and 1 stop bit. Also its needed to set no hardware and no software flow control.

There are 3 VHDL projects, the one from APEX FPGA, the FPGA 2 of the controller and one for the FPGAs in the front end boards.

The setted trigger to the system it is a NIM trigger, with -1V of amplitude and 50ns of length. This pulse is generate in a function generator and its delivered to the trigger input of the controller.

The first step to start the communication is to use minicom to write in the registers of the controller the initial configurations and to enable trigger. This start script (called csNew) it was developed by Daniel Mishins.

To listen to the digitalized output is used the command netcat, in a second terminal. More specifically its used : nc 192.168.10 20443 | xxd. The first address is the Orange Tree IP address and the 20443 is the port number. The xxd prints the result in hexadecimal.

In the figure is shown an example of the data out from the controller [47](#).

```

0004 0100 0000 0000 0004 0100 0000 017b
0000 0000 0004 8054 550e da22 0526 00f6
0100 0000 0004 0000 800e ffc0 0ff3 0ff3
0ff4 0ff3 0ff3 0ff3 0ff3 0ff3 0ff1 0ff2
0ff3 0ff3 0ff2 0ff1 ffc1 000d 000c 000d
000c 000c 000b 000d 000c 000d 000e 000d
000d 000d 000e ffc2 0ff0 0ff0 0ff1 0ff1
0ff1 0ff1 0ff0 0ff1 0ff1 0ff1 0ff1 0ff0
0ff1 0fef ffc3 0ff5 0ff4 0ff4 0ff6 0ff5
0ff3 0ff4 0ff4 0ff4 0ff5 0ff4 0ff5 0ff5
0ff5 ffc4 0002 0000 0001 0000 0001 0000
0001 0001 0000 0001 0001 0001 0000 0001
ffc5 0ffc 0ffc 0ffb 0ffb 0ffc 0ffc 0ffc
0ffb 0ffb 0ffb 0ffb 0ffc 0ffd 0ffa ffc6
0ff9 0ff9 0ffa 0ff9 0ff9 0ff9 0ffa 0ffa
0ff9 0ff9 0ffb 0ffa 0ffa 0ffb ffc7 0005
0005 0006 0004 0004 0005 0004 0005 0005
0005 0004 0005 0004 0003 ffc8 0009 000a
0009 0008 0008 0009 0008 0008 0009 0009
0009 000a 000a 0007 ffc9 0fff 0fff 0ffe
0fff 0fff 0fff 0ffd 0ffd 0ffd 0fff 0ffe
0ffe 0000 0000 ffc9 0fff 0fff 0fff 0000
0ffe 0ffd 0ffe 0ffe 0ffe 0fff 0fff 0ffd
0ffd 0ffe ffc9 000b 000a 000a 000a 000a
0008 0009 000a 000b 000a 0009 0009 000a
0009 ffc9 000a 000b 000c 000a 000b 000a
000b 000b 000c 000c 000c 000c 000c 000c
ffcd 0002 0003 0002 0002 0002 0001 0001
0001 0002 0002 0002 0001 0002 0002 ffce
0fe8 0fea 0fe9 0fe8 0fe9 0fe9 0fe8 0fe9

```

Figure 47 – DAPHNE data out, using a trigger of 1Hz

The data is organized is the form shown in figure [48](#). In figure [47](#) its possible to note that the data its a collection of the data format explained in the last figure. Each

data block have 14 words of 32 bits.

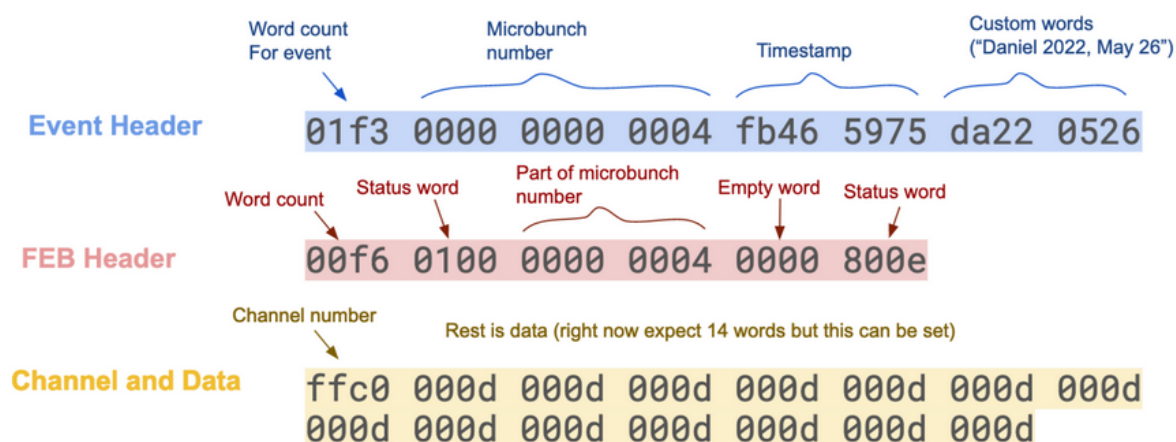


Figure 48 – DAPHNE data format (Polina Abratenko)

The issue to be solved at this moment is that at long time the hardware running the system crashes and stop of sending the requested data. At high trigger rate the problem is much more accentuated.

To run the ISE program its needed first to load the correct licenses from Fermilab. One other thing that is very important is to do the map register of each FPGA code. The registers can be found in the Project_devs.vhd file of each project. In figure 49 is shown one part of the definition of the registers of the FEB FPGA. The main structure of each register address is a vector of 10 bits. Each register have a size of 16 bits. Some registers are the combination of two basic registers, so it have a size of 32 bits.

```

14  Subtype AddrPtr is std_logic_vector(9 downto 0);
15
16
17  -- Control and status register
18  constant CSRRegAddr : AddrPtr := "00" & X"00";
19  -- SDRAM related pointers are 30 bit byte address pointers
20  -- Given the 32 bit wide data I/O registers of the LPDDR interface
21  -- the lower order two bits should be zero.
22  -- LPDDR write address register
23  constant SDRamWrtPtrHiAd : AddrPtr := "00" & X"02";
24  constant SDRamWrtPtrLoAd : AddrPtr := "00" & X"03";
25
26  -- LPDDR read address register
27  constant SDRamRdPtrHiAd : AddrPtr := "00" & X"04";
28  constant SDRamRdPtrLoAd : AddrPtr := "00" & X"05";
29
30  -- Port for microcontroller read/write of SDRAM data
31  constant SDRamSwapPort : AddrPtr := "00" & X"06";
32  constant SDRamPortAd : AddrPtr := "00" & X"07";
33
34  -- DDR status bits, read and write counter

```

Figure 49 – Registers Definition of FEB FPGA

The main logic of each project is defined in the behavioral file, and as an VHDL file it has the port and the entities definition, then the signals definitions and for the last the logic definition.

To compile the code it is used the ISE program and to upload a new code to the FPGAs it is needed to type FL1 or FL2 in minicom to tell the board that we want to load a new code to FPGA 1 or FPGA 2 in the controller. And then it is needed to type the command: `cat compiled_script.bin » port`. When the code of the FPGA 2 is uploaded, the code is written in the 3 FPGA 2. To program in the FPGA FEB it is needed to type just FL.

To check the current status of the binary file it is possible to check the checksum. The actual checksum of the FPGA Apex is 0xFC17 and for FPGA2 is 0x2B99.

3.3.3 Light Monitoring System

The light monitoring system was developed with the aim of detecting light entering the detector during its transfer from the D0 building to the SBND building. Four detection systems were assembled, and they are presented in the figure 50.



Figure 50 – Light Monitoring System

The system consists of:

- One Arduino MKR Zero module
- One 3.7V battery
- One micro SD card
- And one HC-05 Bluetooth module

The Arduino MKR Zero module was chosen over other Arduino systems because it already has a slot for the micro sd card input (used to store data), 12 bits in the ADC

register (as opposed to the standard 10 bits of other Arduinos) allowing for greater reading precision of $3.3V / (2^{12}-1) = 0.0008V$. It also has an integrated battery input and the microcontroller can charge it when connected to another power source. It also has a time counting system, allowing for precise measurement of the time for each reading. Its operating frequency is 48MHz, allowing for higher sampling rates than other Arduino models. Finally, it has a power-saving mode of operation, allowing it to operate for long durations when being powered by a battery.

The HC-05 Bluetooth module communicates serially with the Arduino and was used in Master mode. The communication protocol used by the Bluetooth module uses 3.7V as the logic level '1', which is another advantage of the Arduino MKR Zero.

The MAC address of each of the 4 modules that was used in each of the boxes is:

- Box 1: 00:0E:EA:CF:6D:E2
- Box 2: 00:0E:EA:CF:6E:A1
- Box 3: 00:0E:EA:CF:6D:5C
- Box 4: 00:0E:EA:CF:6D:2B

These addresses are extremely important to determine which box we are communicating with during the transportation process. In the figure 51 is shown the electrical diagram.

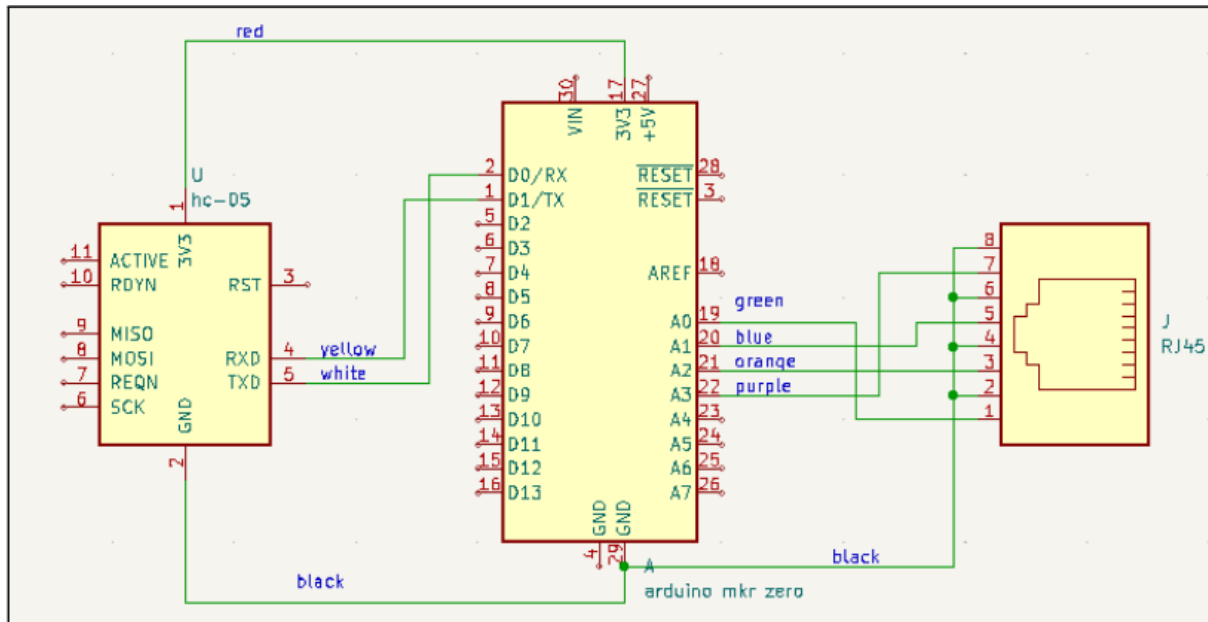


Figure 51 – Electric diagram of the light monitoring system

Four pins of the Arduino were programmed for ADC mode and each one communicates with a DAPHNE ARAPUCA through an RJ-45 port. To read the light being detected, the voltage value between the anode and cathode of each of the 4-SiPMs inside the ARAPUCA was measured. Since SiPMs are sensitive to light, their voltage varies with the amount of light present. Two of the assembled boxes were placed on the west side of the PDS and the other 2 on the east side. Two real-time data reading modes were implemented, the first was done in python and can be used with a computer. In the figure 52 is a screenshot of the software.

```
Monitor 1 :  
26/11/22 04:59:53  
Channel 0: 1176.56 mV  
Channel 1: 1399.78 mV  
Channel 2: 568.13 mV  
Channel 3: 1116.12 mV  
  
File in: 22_11_26/04_59.txt  
  
Monitor 2 :  
26/11/22 04:59:54  
Channel 0: 1005.71 mV  
Channel 1: 1000.51 mV  
Channel 2: 353.77 mV  
Channel 3: 930.02 mV  
  
File in: 22_11_26/04_59.txt  
  
Monitor 3 :  
26/11/22 04:59:55  
Channel 0: 967.04 mV  
Channel 1: 968.64 mV  
Channel 2: 440.81 mV  
Channel 3: 814.73 mV  
  
File in: 22_11_26/04_59.txt  
  
Monitor 4 :  
26/11/22 04:59:56  
Channel 0: 1301.47 mV  
Channel 1: 1228.94 mV  
Channel 2: 462.56 mV  
Channel 3: 930.77 mV  
  
File in: 22_11_26/04_59.txt
```

Figure 52 – Python software of the light monitoring system

For this application it was utilized 4 Threads one to each channel, responsible for reading the data and sending the data to a fifth thread responsible to aggregating the data and sending to a final thread responsible for printing the data in the terminal console.

Another software was developed using Java for Android devices, and here is an image 53 of the program in action.



Figure 53 – Java software of the light monitoring system

For this software it was utilized also 4 thread to reading the data. Each thread sends the data to a unique thread responsible for processing the data and printing in an unique graphic window in the screen.

Finally, the data was saved in ADC channels on the SD card for future analysis. In figures from 54 to 57 it is shown the plots of the saved data on the day of the move, for all the boxes.

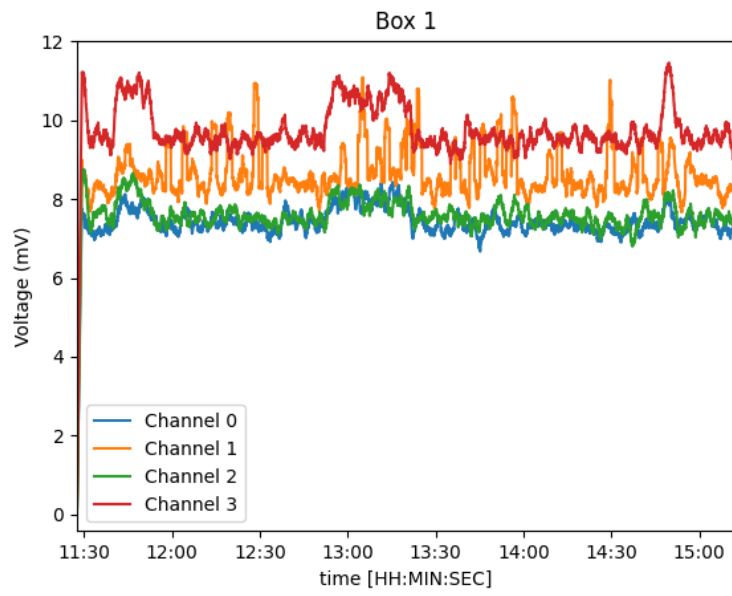


Figure 54 – Light data for Box1

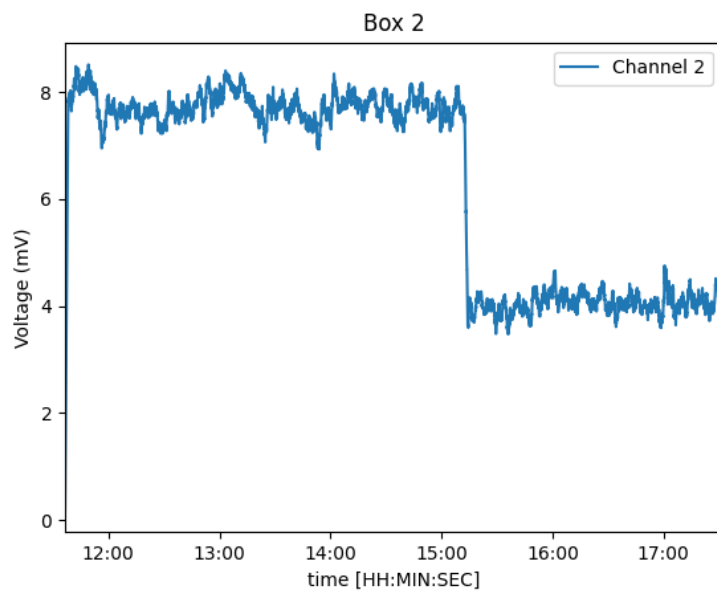


Figure 55 – Light data for Box2

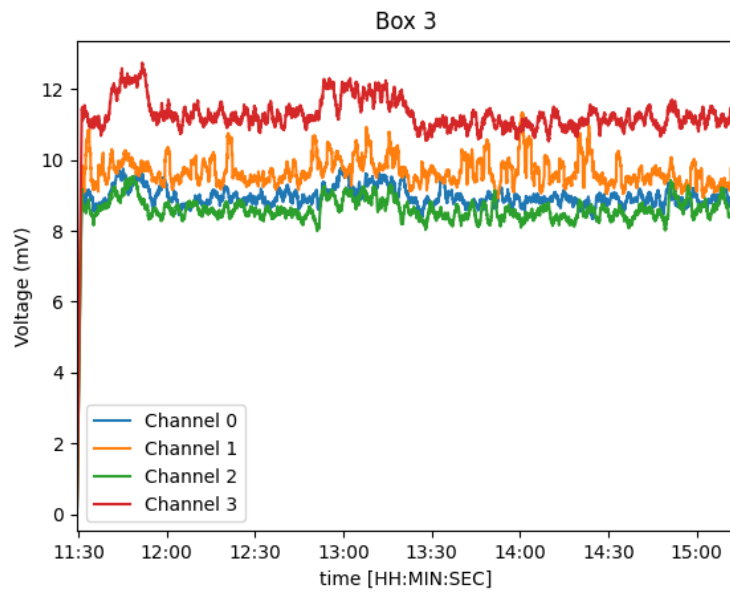


Figure 56 – Light data for Box3

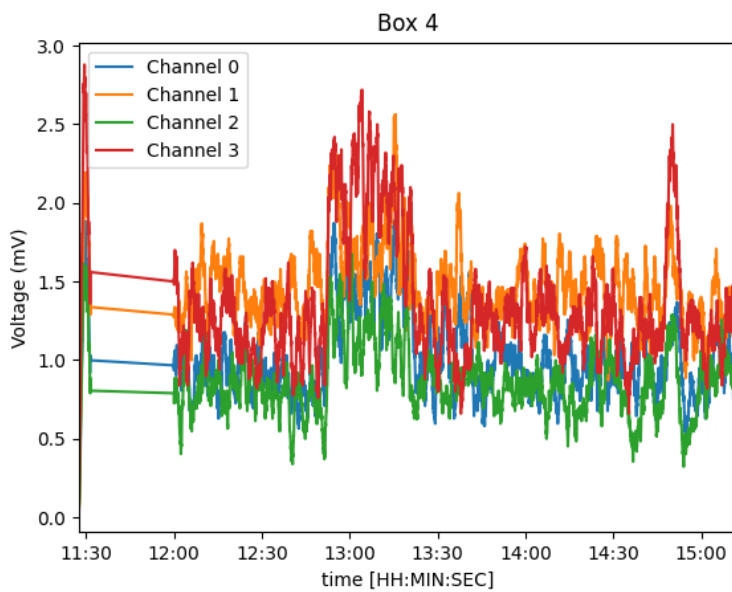


Figure 57 – Light data for Box4

The voltage in the SiPMs stayed around 10mV with little fluctuations. This the voltage at low light, so its possible to conclude that the light didn't entered in the detector.

In Box2 happened an connection problem, and only one channel worked. Meanwhile the Box4 happened the RJ45 cable was bad connected in the starting, but it was later fixed.

Another project carried out was the development of a software, also for Android using Java, for measuring the angles and inclinations suffered by the PDS frame. Four WT901BLECL sensors from WitMotion were used. The data was saved on the smartphone itself. In the figure 58 is shown the screen of the software working.

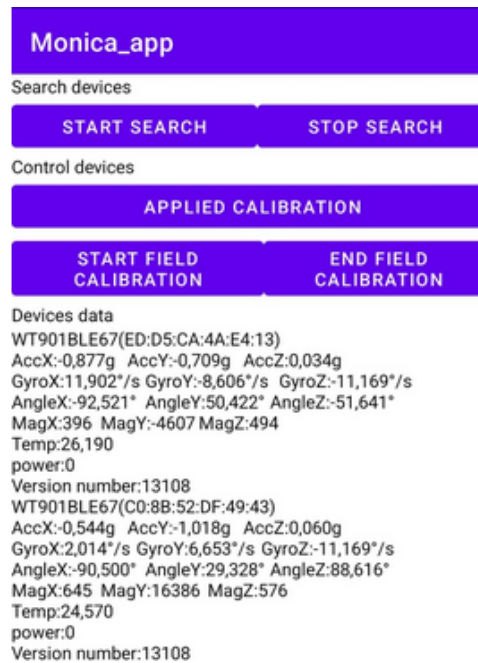


Figure 58 – Angle software

The software measures angles, angular velocity, angular acceleration, and temperature. To use the software, the user must enter 2 out of the 4 sensors that they wish to use. The code is an adaption of the program available in the GitHub account of the company.

4 First Estimation of VIS X-ARAPUCA detection efficiency

In this section, the efficiency measurement of the X-ARAPUCA sensitive to visible light will be presented. The mechanical structure and the SiPMs (Silicon Photomultipliers) used are the same as those in the traditional X-ARAPUCA. However, there is no need for the deposition of the wavelength shifter on the filter since the photons that reach the filter window have already been converted to visible light. The dichroic filter used has an upper cutoff (around 460nm), and the light guide bar is made with a wavelength shifter that has a higher value than the cutoff of the filter.

This measurement was carried out in the Leptons Laboratory at UNICAMP (University of Campinas) using a small cryostat with liquid argon, with two possible sources of light: a blue LED and an alpha source.

4.1 The X-ARAPUCA

The X-ARAPUCA have a dimension of (100x130x20)mm. In the figure 59 is shown a picture of the device.



Figure 59 – X-ARAPUCA used in this experiment

The dichroic filter have an cutoff wavelength of 460nm with dimensions of 77x100 mm. In figure 60 is show a picture spectre of transmittance.

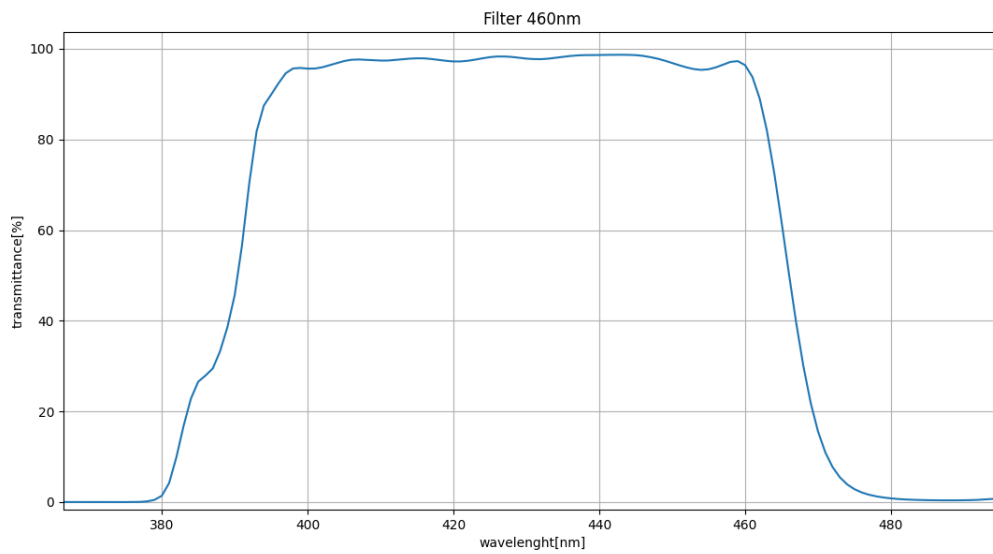


Figure 60 – OPTO dichroic filter spectrum

The lightguide is the GREEN from Glass to Power and is shown in figure 61.



Figure 61 – Lightguide from glass to power

The SiPM boards contains 4 SiPM windows. This SiPM is the S14160-6050HS model explained in more details in 3.3.2.1.

4.2 The Setup

It was used to the experiment the cryostat shown in figure 62.



Figure 62 – Cryostat

It was made a support for the X-ARAPUCA using a 3d printer. The X-ARAPUCA with the support was placed above of another support made of PVC, serving as a base. In the lateral pillar it was put a foil of VIKUITI with TPB evaporated. Two other foils was put in the inferior and superior base covering all the front part of the ARAPUCA setup. The VIKUITI is fastened in the support with the help of screws. In figure 63 is shown the support and the VIKUITI with TPB.



Figure 63 – Support for the X-ARAPUCA and VIKUITI with TPB embedded

Together with the setup it was made another support, but this time to accommodate α -source disk 59. The disk is made of an alloy of uranium and aluminium. The uranium from the disk decays to alpha particles (equation 4.1), that in contact with the liquid argon causes scintillation as explained in section 3.2.1. This photons of 127 nm can be detected by the ARAPUCA after they are shifted by the TPB in the walls. The disk was covered in its edge surface by aluminium paper, to reduce the intensity of particles ejections from the Uranium disk.



In the middle of the main setup it was put a resistor of 10Ω and in top a platinum sensor known as PT-1000. Both were used to detect the level of the liquid argon inside the cryostat, since when the liquid argon at 87K touches the sensor, the temperature of the device will decrease and as consequence his resistance will also decrease. So if we have a voltage source connected to the sensor, the current will increase almost instantaneous when the cryogenic liquid reaches it.

The resistance at 0°C of the PT1000 is $1k\Omega$. The equation of resistance in function of temperature in $^\circ\text{C}$ (when the temperature is below 0°C) of the PT1000 [56] is given by 4.2.

$$R(T[^\circ\text{C}]) = 1 + 3.9083 \times 10^{-3}T - 5.772x \times 10^{-7}T^2 - 4.2735 \times 10^{-12}(T - 100)T^3 [k\Omega] \quad (4.2)$$

So the resistance at 87K($-186,15^\circ\text{C}$) is 220Ω . Applying a voltage of 20V in the PT1000, the current expected at this temperature is around 90mA.

Then this whole setup it was put inside the cryostat and the cryostat closed. Before closing it was also put an optical fiber entering the cryostat through the top flange. The goal of the fiber is to driven the light signal from an external blue LED to inside the cryostat. Since this photons already are blue, they don't need to be converted by the TPB to be detected by the X-ARAPUCA.

With help of two pumps (one normal and one turbo) it was made, as far it was possible, an vacuum environment inside cryostat, arriving in the pressure of 1.1×10^{-4} mbar. To read this pressure it was used the pressure sensor Maxigauge TPG 256A of the Pfeiffer Vacuum, capable of reading pressure from 10^{-12} to 50 bar, depending of the manometer connected [42]. There is exclusive flange in the cryostat to the sensor level and another flange to the electrical cables of the X-ARAPUCA/SiPM.

With the X-ARAPUCA, the supports, the sensors and the optical fiber inside the cryostat and the cryostat is closed at vacuum the next step is to give a thermal bath with liquid argon in the cavity outside the cryostat. The goal of this bath is to help maintain the pressure low inside the cryostat in the next step and help with thermal isolation. When the thermal bath starts the pressure inside the cryostat starts to decrease more, since temperature inside starts to decrease and by the ideal gas law, pressure is proportional to temperature.

The next step is to start filling the interior of the cryostat with argon. To do that a valve its open allowing argon gas 6.0 (the concentration of impurities is at the

six house after the decimal dot , which means 0.000001%) at higher pressure enter the interior of cryostat.

Since more molecules are entering, the pressure starts to increase quickly and it can become greater than the external ambient pressure P_o . So to not let the cryostat explode it is checked in an analog pressure gauge if the pressure inside isn't higher than $1.5P_o$. If this happens the external bath of liquid argon must be redone to reduces the internal pressure.

While the argon gas enters the cryostat it exchange heat with the outside thermal bath and start to liquefy, filling the cryostat with LAr. Approximately after 2 hours of the start of the process of filling with argon gas, the liquid argon reaches the top of internal setup and the valve can be closed.

A diagram of the setup is shown in figure 64.

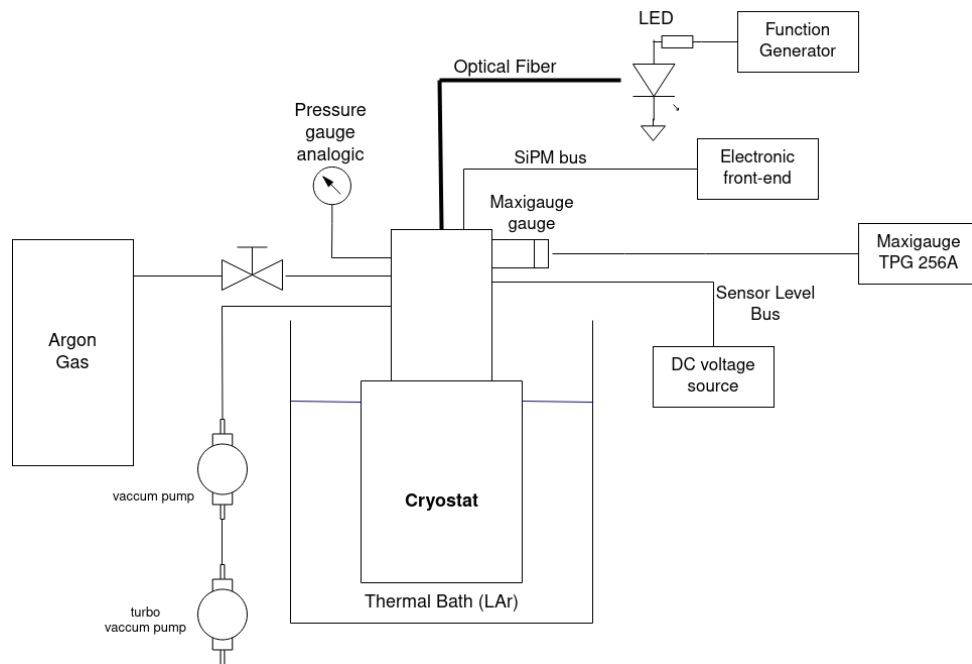


Figure 64 – Diagram of the experimental setup

4.3 Electronics

The SiPM board is made of the 4 SiPM windows and they are connect in parallel, so the current is summed from both of them. The electric diagram of the SiPM board is show in figure 65. The capacitor in the figure 65 of 100 nF

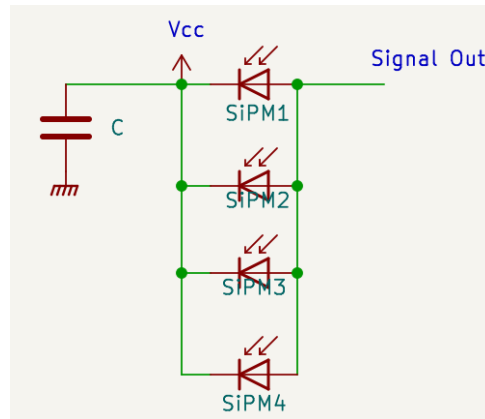


Figure 65 – Electrical configuration of the SiPMs

The signal of each SiPM boards goes to a channel of the APSAIA, totalizing two channels used. The APSAIA is used to power supply the SiPM and to amplify the input signal, as explained in 3.3.2.1. The gain was put in low (20 or 13.01dB).

The breakdown voltage at ambient temperature ($26\text{ }^{\circ}\text{C}$) of the HS SiPM is 38V, and the variation of the breakdown voltage in relation of the variation of the temperature is $34\frac{\text{mV}}{\text{K}}$ [32]. So at 87K the variance in temperature was 213.15K, giving a breakdown voltage difference of $34 \times 214.15 = 7.25\text{V}$. So the breakdown voltage at this cryogenic temperature is around 31V.

Then the amplified signal goes to the digitizer CAEN V1730, with 8 channels and a frequency sampler of 500MHz and with 14 bits in each ADC channel. The max range is 2Vpp.

The data is collected to a laptop using the software Wavedump. An schematic of this setup is shown in figure 66.

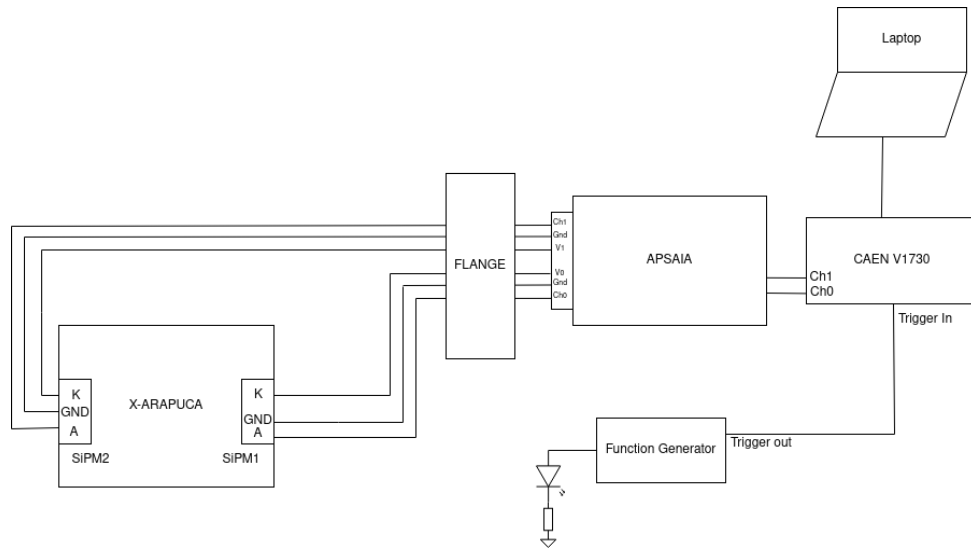


Figure 66 – Electrical diagram of the setup

4.4 Simulation

It was simulated in Geant4 the setup, and its shown in figure 67 the modeled setup.

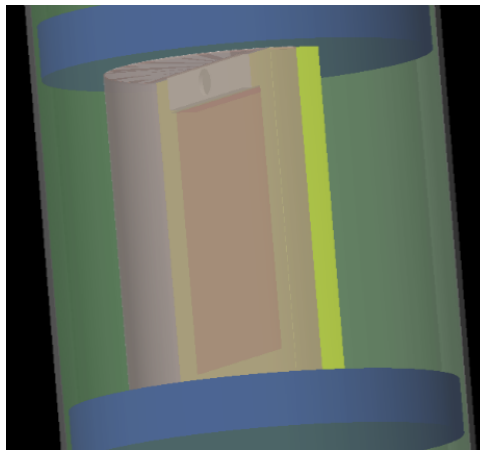


Figure 67 – Simulated setup of the experiment

The VIKUITI was assumed to have an reflectivity of 95%. The source consists of an aluminum disk where alpha particles with random position and momentum direction are generated. This leads to a continuous emission spectrum from the source.

The distance travelled by photons in TPB before are absorbed are found in figure 68. In figure 69 is shown the reemitted spectrum of TPB.

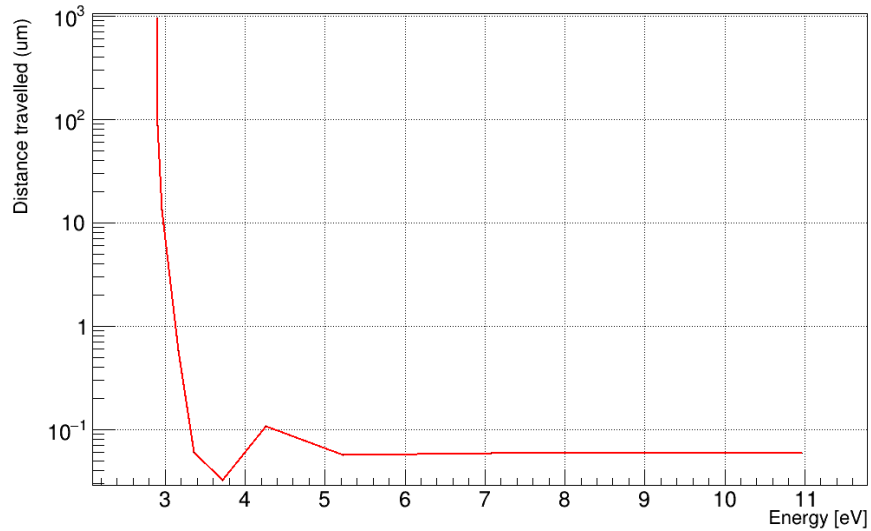


Figure 68 – Distance travelled by photons in TPB before being absorbed

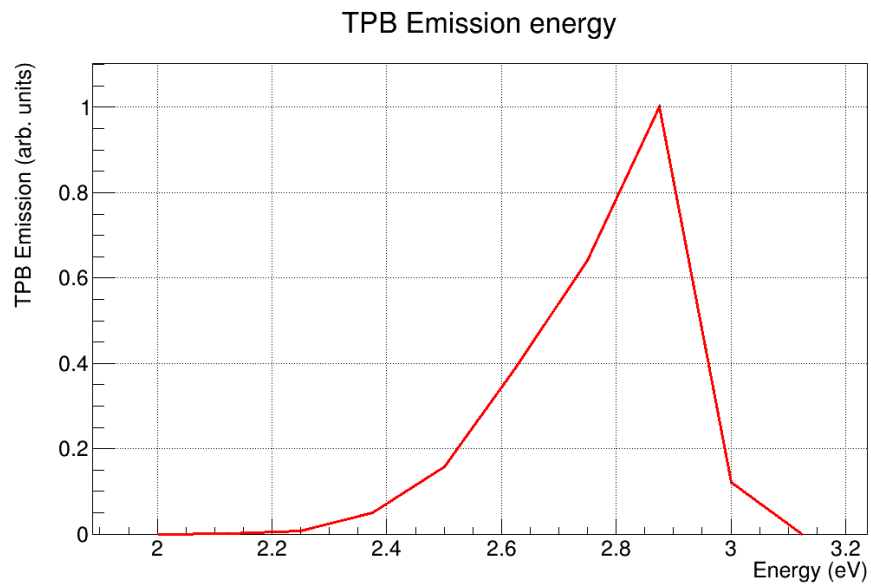


Figure 69 – TPB Specrum of reemision

In the simulation it was generate 250000 alphas with the energy spectrum shown in figure 70 an only 48567 were able to leave the source.

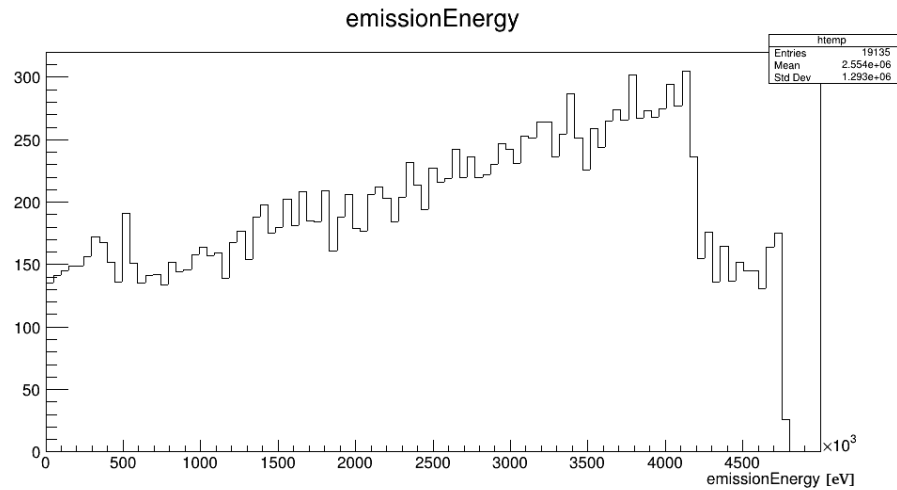


Figure 70 – Energy spectrum of emitted alphas

The result histogram of the number of photons that arrived the ARAPUCA window is shown in figure 71.

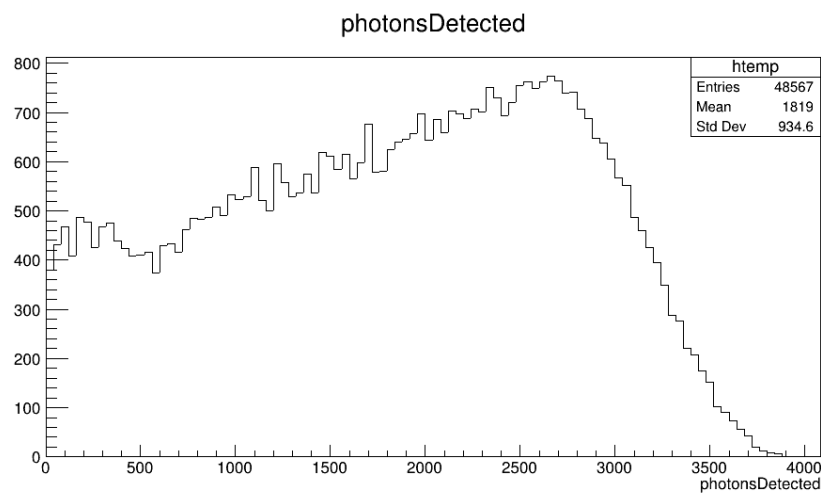


Figure 71 – Histogram of photons that arrived in the window per alpha emitted

4.5 Data Acquisition

The acquisition was made using the software Wavedump, from CAEN itself [57]. To use the program it is needed to correct fill the parameters. For all the runs was setted pulse polarity positive and a baseline of 10.

The baseline varies from 0% to 100%, and its value means the percentage of the max ADC scale $2^{14} - 1 = 16383$. A baseline of 10 means that the 0V equals to $\approx 16383 * 0,1 = 1638$ ADC channels. But the max range it still 2000mV. A schematic of the conversion from mV to ADC channels is shown in figure 72.

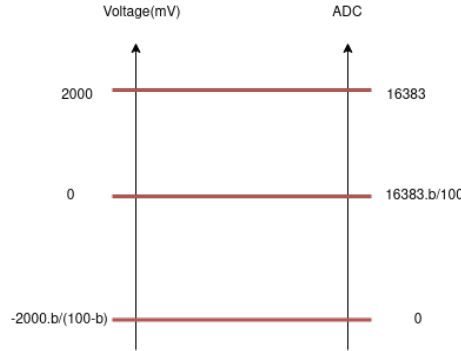


Figure 72 – ADC CAEN equivalence to mV. The value b means the baseline put in the Wavedump configuration file (0 to 100)

So with a baseline of 10, the range in mV goes from -222.22 mV to 2V. And one variation of ADC channel means a variation of $\frac{2000mV}{16383(1 - b/100)} \approx 0,14mV$.

The equation 4.3 gives the relation between value of ADC channel to mV.

$$[mV] = \frac{2000}{16383(1 - b/100)}[ADC] - \frac{2000.b}{100 - b} \quad (4.3)$$

So for a baseline of 10, this is equal to: $[mV] \approx 0.14[ADC] - 222.22$.

The sampler frequency is 500MHz. By Nyquist theorem this gives the maximum frequency of the sampled signal that its possible to acquisitive without ambiguity of $500MHz/2 = 250MHz$, which is much higher than maximum frequency of an SiPM $\approx ((R_q + Z_{in}).C_j)^{-1}$ (see more in 148). The sample time is equal to $1/250MHz = 2ns$.

For the analysis of the α particles it was configured the Channel 1 as source of the trigger acquisition. The value of threshold of the trigger can be setted from 0 to ADC full scale (16383). And this value is relative to the baseline, so this means that a conversion from threshold to mV is given by equation 4.4.

Run	α (internal trigger) or LED (external trigger)	V_{SiPM}	Trigger Threshold (ADC / mV)	V_{LED}	Number of trigger events	Number of Samples (RECORD LENGTH / time)	LED Frequency(Hz)
1	LED	36V	X	5.1V	53204	2000=4 μ s	100
2	LED	36V	X	5.2V	69153	2000=4 μ s	1000
3	LED	36V	X	5.3V	60490	2000=4 μ s	1000
4	α	36V	500 = 61.04mV	X	56435	6000=12 μ s	X
5	α	36V	300 = 36.62mV	X	50396	6000=12 μ s	X
6	α	36V	200 = 24.41mV	X	55020	6000=12 μ s	X
7	α	36V	3500 = 427.27mV	X	1653	6000=12 μ s	X
8	LED	36V	X	5.1V	89231	1000=2 μ s	1000
9	LED	36V	X	5.2V	76327	1000=2 μ s	1000
10	LED	36V	X	5.3V	100343	1000=2 μ s	1000
11	LED	34V	X	5.1V	92777	1000=2 μ s	1000
12	LED	34V	X	5.2V	68874	1000=2 μ s	1000
13	LED	34V	X	5.3V	64433	1000=2 μ s	1000
14	α	34V	200 = 24.41mV	X	41485	6000=12 μ s	X
15	α	34V	100 = 12.21mV	X	59717	6000=12 μ s	X
16	α	34V	300 = 36.62mV	X	52982	6000=12 μ s	X
17	α	34V	1200 = 146.49mV	X	967	6000=12 μ s	X
18	LED	34V	X	5.1V	85141	1000=2 μ s	1000
19	LED	34V	X	5.2V	60599	1000=2 μ s	1000
20	LED	34V	X	5.3V	53957	1000=2 μ s	1000
21	LED	38V	X	5.1V	53701	1000=2 μ s	1000
22	LED	38V	X	5.2V	57152	1000=2 μ s	1000
23	LED	38V	X	5.3V	57878	1000=2 μ s	1000
25	LED	36V	X	5.1V	62003	1000=2 μ s	1000
26	LED	36V	X	5.2V	53419	1000=2 μ s	1000
27	LED	36V	X	5.3V	61579	1000=2 μ s	1000
28	α	34V	200 = 24.41mV	X	62889	6000=12 μ s	X

Table 6 – Information of each data run

$$threshold[mV] = \frac{2000}{16383} threshold \quad (4.4)$$

To study the system response to photons of the LED it was used a function generator. The function generator powered up the LED with a pulse width of 170ns, a frequency of 1kHz and voltage of 5.1V or 5.2V or 5.3V. To trigger the digitizer, it was used the trigger output of the function generator.

The RECORD LENGTH option defines the number of samples per trigger. The total signal then have an duration of RECORD LENGTH $2ns$.

In total it was a total of 27 runs of acquisition, with different parameters setted as shown in table 4.5.

4.6 Data Analysis

The next section will talk about the data analysis. To the analyses was used the software ROOT from CERN [58]. Its a program with the paradigm of programming know as object-oriented. The ROOT program is widely used to analyse a lot of data and have an incredible capability of compressing and linking different types of data.

Also it was used some of the codes used by Henrique de Souza in his PHD thesis [12] with modifications, together with other scripts, that was made with the knowledge learned while working with the C-Arapuca project (7).

4.7 Filtering the signal and Baseline

The implemented algorithm to filter the noise is the filter 1D total variation denoise filter explained in [59]. The goal of this filter is to minimize the function defined in equation 4.5. In the equation, the sequence x is the solution for the problem and y is the input noised signal. The term λ is an Lagrange multiplier given by the user.

$$\frac{1}{2} \sum_{i=0}^{N-1} |y[i] - x[i]|^2 + \lambda \sum_{i=0}^{N-2} |x[i+1] - x[i]| \quad (4.5)$$

In this analysis it was choose a lambda of 14. In the figure 74 and 73 is shown the result in the channel 0 in the run 27.

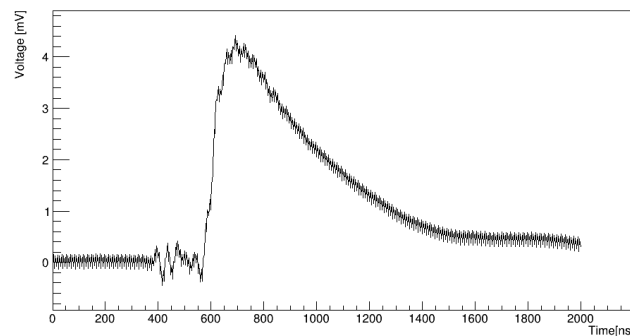


Figure 73 – Signal without the filter

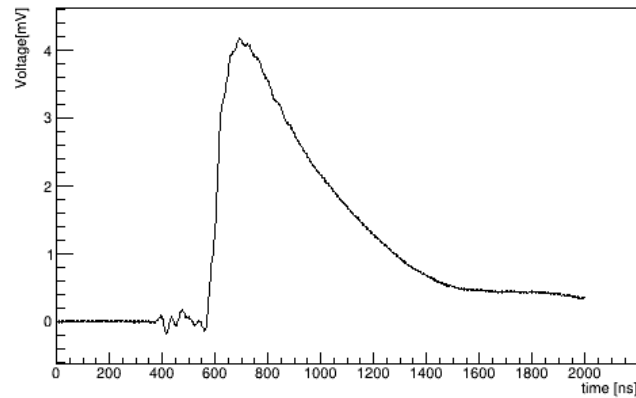


Figure 74 – Signal with the filter

To calculate the baseline its calculated the mean signal in a window of time before the pulse start. To choose this window its looked in the persistence of a larger number of waves to look for the best end point.

Also if some peak above some threshold is found while evaluating the baseline a time window is jumped and is not going to be used to evaluated the baseline.

4.8 LED light

The power applied in the LED is given by $P = V_{blue}I$, where V_{blue} is the knee voltage of a blue LED around 3,6V. So the mean power can be given by equation 4.6. In the equation R is the resistor in parallel with the led, and V is the applied voltage in the set.

$$\langle E \rangle = \alpha V_{blue} \cdot \frac{(V - V_{blue})}{R} \quad (4.6)$$

In the figures 77 and 78 for the SiPM powered up with 36V, in 75 and 76 is for 34V and in 79 and 80 is for 38V.

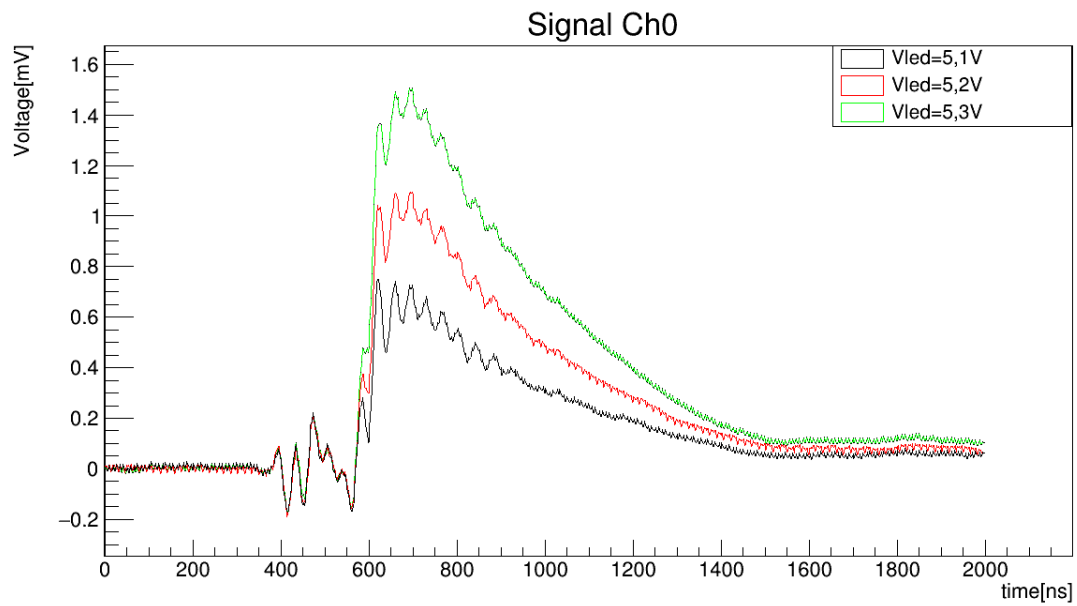


Figure 75 – Mean Signal of the SiPM from channel 0 with 34V

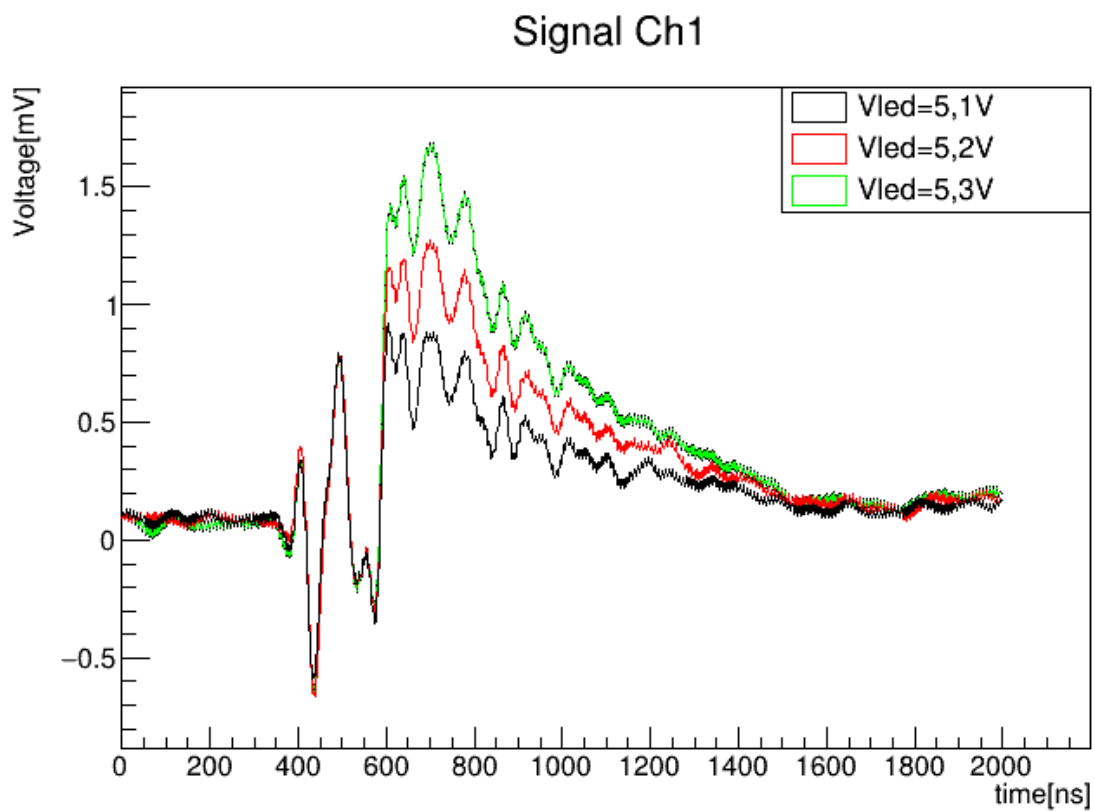


Figure 76 – Mean Signal of the SiPM from channel 1 with 34V

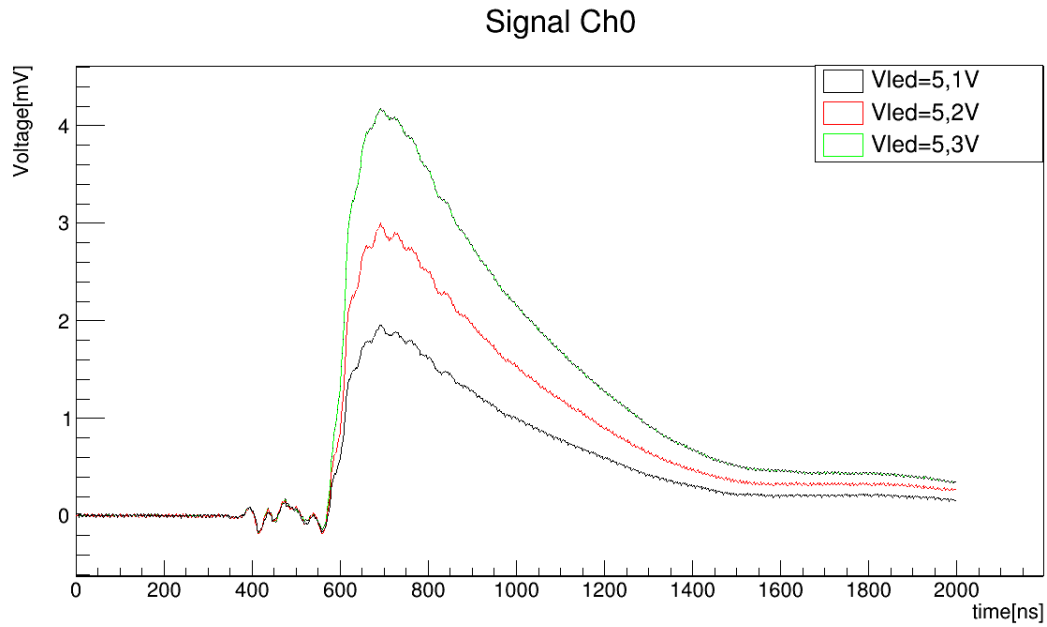


Figure 77 – Mean Signal of the SiPM from channel 0 with 36V

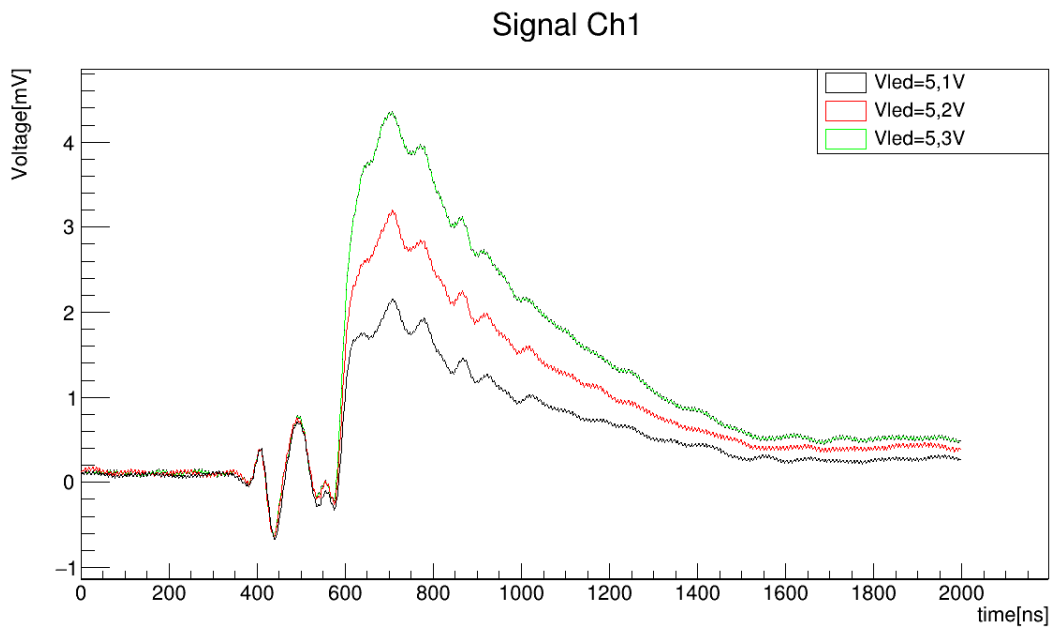


Figure 78 – Mean Signal of the SiPM from channel 1 with 36V

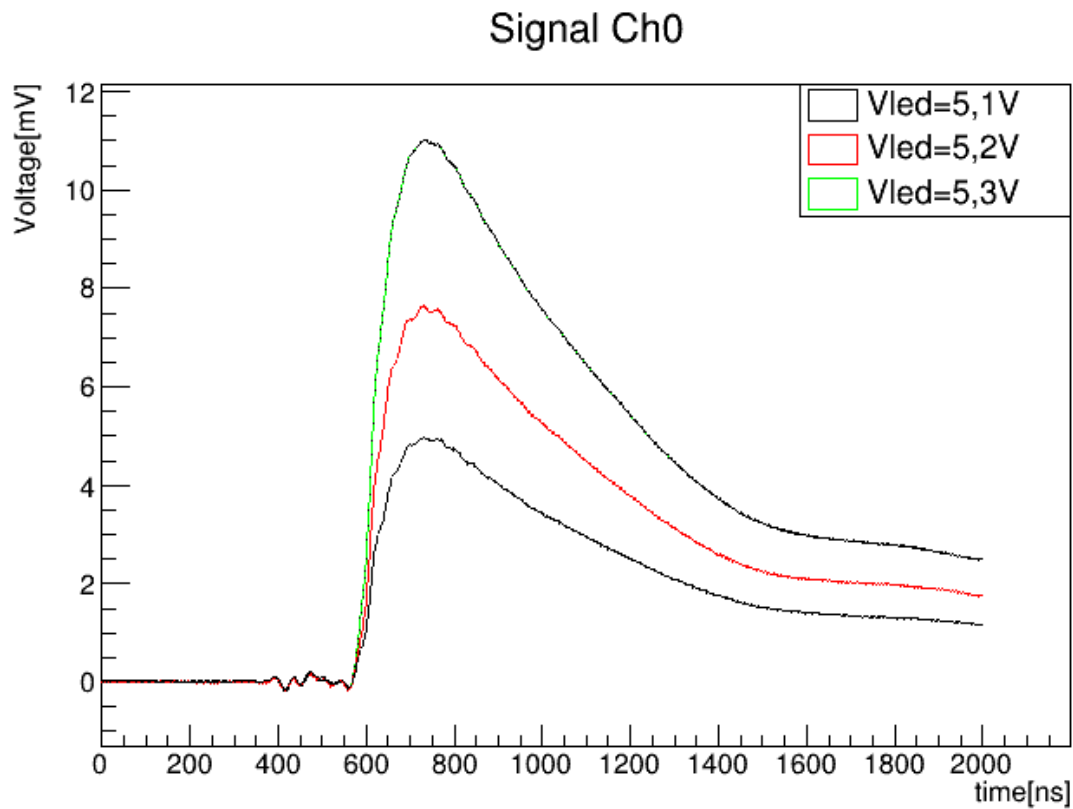


Figure 79 – Mean Signal of the SiPM from channel 0 with 38V

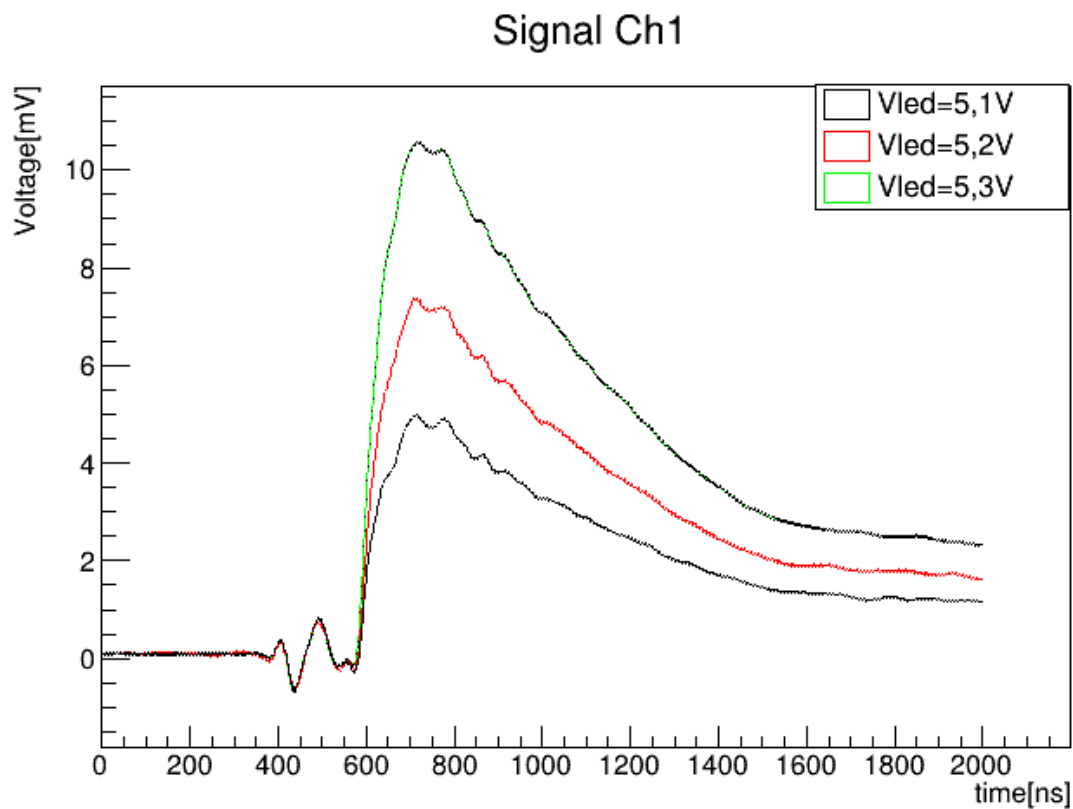


Figure 80 – Mean Signal of the SiPM from channel 1 with 38V

What is possible to notice is that for the same overvoltage in the SiPM, the bigger the luminosity intensity higher will be the output signal. This is expect, since more photo-electrons are being generated. Also channel 0 response is more behaved than channel 1. So because of this all the analysis that will be discussed beyond this point are going to use only channel 0.

For the same power applied in the LED (same applied voltage in R/LED) the output voltage increases as the SiPM overvoltage increases (as expected in equation D.15).

If we integrate all the signal and divide by the input impedance of the digitizer(50Ω) its obtained the signal's charge as shown in equation 4.7.

$$Q = \frac{1}{Z_{in}} \int_0^T v(t) dt \quad (4.7)$$

In figures 81 from to 83 are shown the histogram of charge for Channel 0 for 9 distints configurations, SiPM 34V, 36V and 38V, and LED voltage 5.1V, 5.2V or 5.3V.

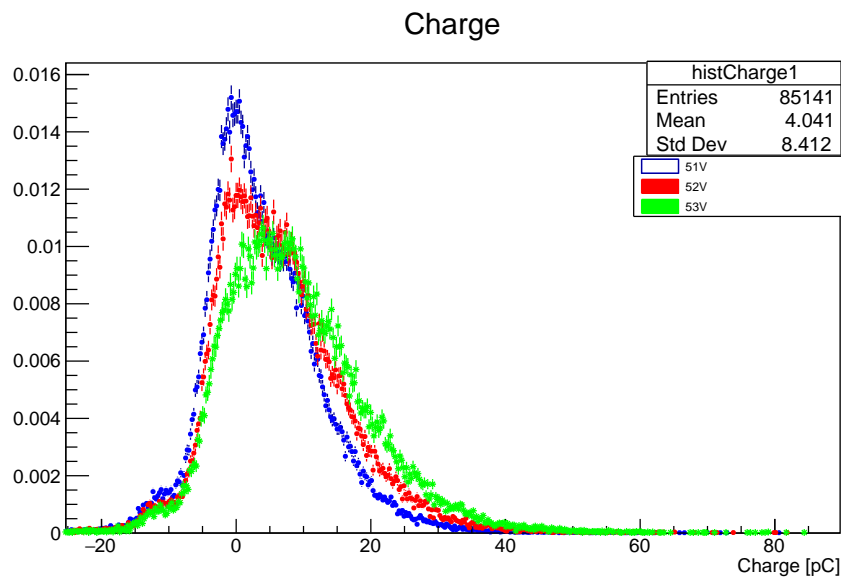


Figure 81 – Histogram for 34V

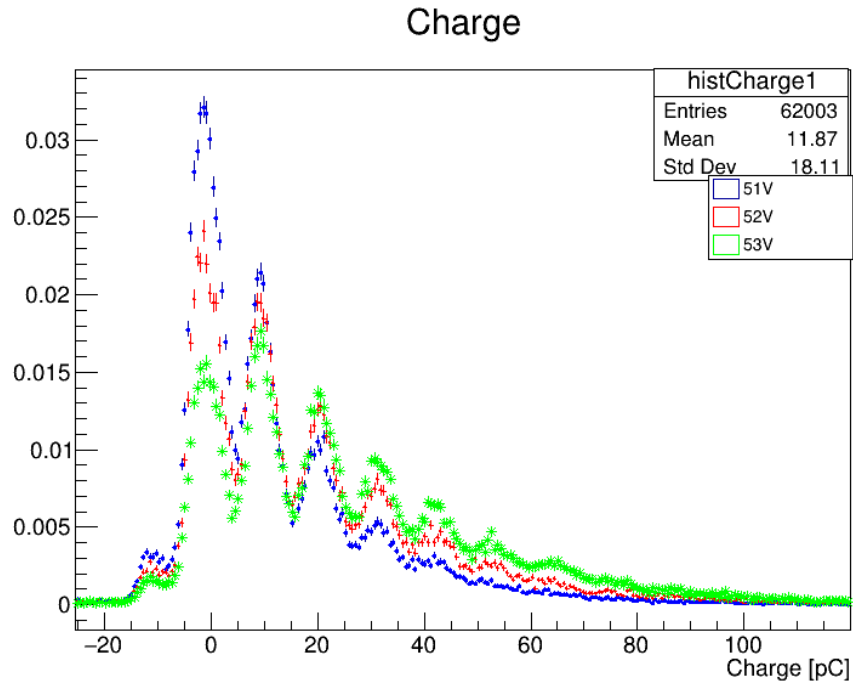


Figure 82 – Histogram for 36V

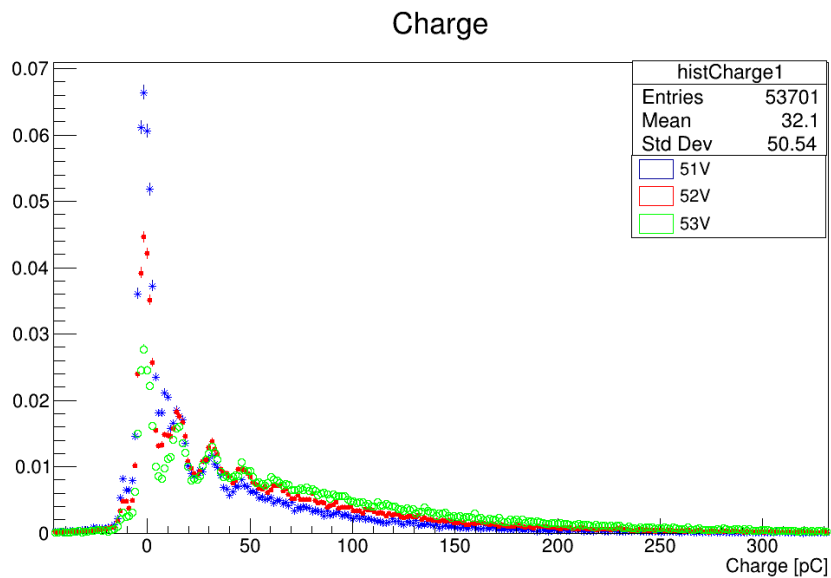


Figure 83 – Histogram for 38V

In the histogram as the SiPM voltage increases more larger become the right tail of the histogram. Also its possible to note that as the the voltage increases, more peaks appear and they tend to stray from the central peak in 0.

Each peak in the histogram are the distribution of an certain number of photon-eletrons generate in an event trigger. The first peak is the baseline noise, the second peak is distribution of the first photo-electron, in other words an event trigger just one photon was converted to a photo-electron. The third peak is the second photo-eletron, in an event trigger two photons were converted to two eletrons. The fourth peak is the third photo-electron and this logic goes on. The distance between the peaks is the photo-electron charge.

4.9 Single Photon Eletron

The probability of detecting one photon and photoeletron being generate is p , and the reverse probability (the single photon electron not being generate) is $q=(1-p)$. Since each event of trigger generates a large number of photons n , each one independent of each other, and each each one of them have a low probability p of generating a photo-eletron, the number of photons being detected by the X-ARAPUCA can be modeled as a poisson distribution, as shown in equation 4.8.

$$P[i] = \lambda^i \frac{e^{-\lambda}}{i!} \quad (4.8)$$

In the equation, i is the i th photoeletron and λ is the mean of the distribution (and also the standard deviation) and equals to $p.n$.

Also the measured charge(q) of an single photon electron is equation $q = q_1 + q_n$, q_1 , where q_1 is the expected signal charge of the photo-eletron (mean) and q_n is the noise. Moddeling the noise as AWGN(Additive White Gaussian noise), the distribution of an single photon electron is an gaussian with mean q_1 and standard deviation σ_1 , or $\mathcal{N}(q_1, \sigma_1^2)$.

The distribution of two generated photo-electron is the distribution of the variable x equals to $q + q'$,since each detected photon is independent of each other. The mean of the variable x are calculated in equation 4.9 and in equation 4.10 is calculated the variation.

$$\langle x \rangle = \langle q \rangle + \langle q' \rangle = 2q_1 = q_2 \quad (4.9)$$

$$\begin{aligned} \sigma_x^2 &= \langle x^2 \rangle - \langle x \rangle^2 = \langle q^2 \rangle + \langle q'^2 \rangle + 2 \langle q.q' \rangle - 4 \langle q \rangle^2 = \\ &= 2(\langle q^2 \rangle + \langle q \rangle \langle q' \rangle - 2 \langle q \rangle^2) = 2(\langle q^2 \rangle - \langle q \rangle^2) = 2\sigma_1^2 \end{aligned} \quad (4.10)$$

The distribution of the second photo-electron is also a gaussian, written as $\mathcal{N}(2.q_1, 2.\sigma_1^2)$. So doing the same process for the next peaks, the nth photo electron is the normal distribution $\mathcal{N}(n.q_1, n.\sigma_1^2)$.

So to fit the histogram, first is fitted an gaussian (Multiplication constant with three free parameter saverage and standard deviation) in the charge baseline. The next step is to fit a gaussian in the first single photon-electron peak (second peak) also with three parameters free. Next its fitted the combination of this two gaussian with the initial parameters collected in the two first fits.

Now for the third peak, its fitted the conjunt of three gaussian (baseline, first photo-electron and second-photo-electron), with the initial parameters of the first two gaussians collected from the previous fit, and for new gaussian, the initial parameter for the mean is $2.q_1$ and the standard deviation is $\sqrt{2}\sigma_1$. This process is repetead again for the next peaks, remembering that each peak follows the normal distribution $\mathcal{N}(n.q_1, n.\sigma_1^2)$.

In figure 84 are show the fit for the case of the figure ??, the case where peaks are more clear.

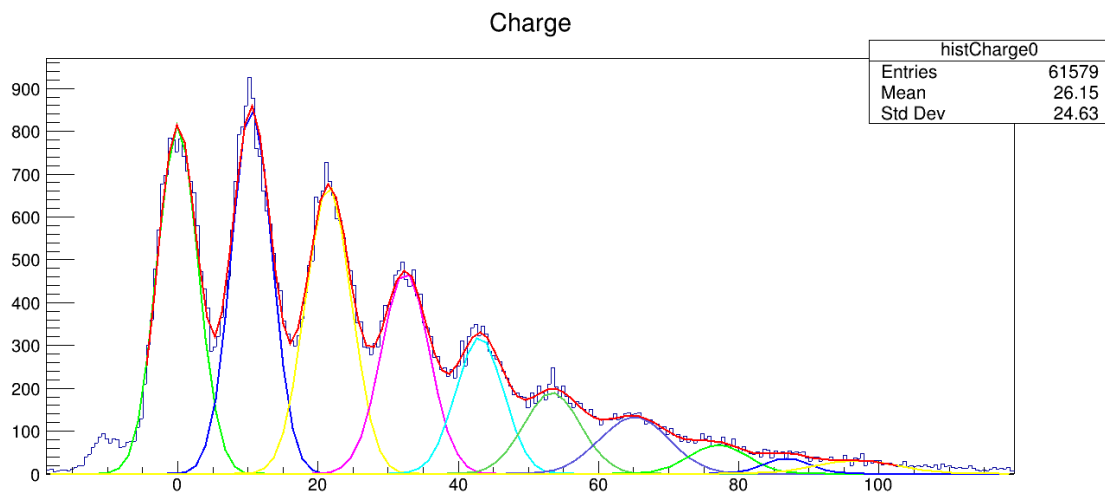


Figure 84 – Fitted single-photon electron peaks

In table 4.9 are shown the fitted values with the respective errors. The probability gaussian distribution for the nth photo-electron is defined as show in equation 4.11.

$$p_n = A_n \cdot e^{-\frac{(x-\mu_n)^2}{2\sigma_n^2}} \quad (4.11)$$

n	Multiplicative constant (An)	Mean (μ_n) [pC]	error [pC]	Ratio Mean/ q_1	Expected Ratio	Standard deviation (σ_n) (pC)	error [pC]	Ratio σ/σ_1	Expected Ratio
0	814,404 \pm 14,309	-0,084	0,0785	-0.008 \pm 0.007	0	3,0205	0,0905	1.059 \pm 0.038	X
1	857,543 \pm 14,429	10,531	0,04575	1 \pm 0.006	1	2,8535	0,056	1 \pm 0.028	1
2	671,987 \pm 8,075	21,4835	0,064	2.040 \pm 0.011	2	3,288	0,0885	1.152 \pm 0.038	$\sqrt{2} = 1.41$
3	470,705 \pm 6,887	32,446	0,064	3.081 \pm 0.015	3	3,4335	0,1515	1.203 \pm 0.058	$\sqrt{3} = 1.73$
4	319,086 \pm 7,951	43,033	0,1915	4.086 \pm 0.025	4	3,4215	0,2695	1.199 \pm 0.097	$\sqrt{4} = 2$
5	188,409 \pm 13,751	53,3825	0,4265	5.069 \pm 0.046	5	4,0665	0,699	1.425 \pm 0.247	$\sqrt{5} = 2.24$
6	132,767 \pm 6,506	65,109	0,6045	6.183 \pm 0.063	6	4,976	1,4	1.744 \pm 0.492	$\sqrt{6} = 2.45$
7	67,3079 \pm 16,630	77,0835	1,1485	7.320 \pm 0.114	7	4,212655	1,135	1.476 \pm 0.399	$\sqrt{7} = 2.65$
8	35,2716 \pm 18,230	86,798	1,098	8.242 \pm 0.110	8	3,46542	0,633	1.214 \pm 0.223	$\sqrt{8} = 2.83$
9	30,7253 \pm 2,266	96,789	1,067	9.191 \pm 0.109	9	6,116	1,2465	2.143 \pm 0.439	$\sqrt{9} = 3$

Table 7 – Experimental data of the run 27

So the photo-electron charge for this configuration is 10.531 pC, and this information are going to be used in the next section 4.11. So the gain in charge for an single photon electron can be calculated as:

$$G = \frac{Q}{eG_{APSAIA}} = \frac{10.531 \times 10^{-12}}{20 \times 1.6 \times 10^{-19}} = (3.291 \pm 0.014)10^6 \quad (4.12)$$

Also the distance between the peaks almost follows what was expect with little deviation. However the standard deviation as the we go further to higher photo-electrons peaks, is starts to deviate more and more of expect value. The origin of this can be that the noise don't really follow an gaussian distribution, and in the signal are other forms of noise like crosstalk, afterpulses and darnnoise. Also for the distribution of larger photon-electron converted (peaks more to right in the plot), the distributions starts to mix and becomes more harder to the software analyze each one.

With each peak fitted, its possible to separate the pulse of the single-photon electron, from the baseline noise and from high orders of photo electron detected. To do this, its only take the signal with the total charge being greater than the point where the first two gaussians intercept and lower than the point where the second and third distribution intercepts each other. This value that separates both gaussians can be found by finding the minimal of the total fit between the two peaks in question. Analytical this means the ethe point where two gaussian intercepts as shown in equation 4.13.

$$A_m e^{-\frac{(x-\mu_m)^2}{2\sigma_m^2}} = A_n e^{-\frac{(x-\mu_n)^2}{2\sigma_n^2}} \quad (4.13)$$

The solution to this equation is shown in 4.14, if the standard deviation of the both gaussian are not the same.

$$x_{\pm} = \frac{\mu_m \sigma_n^2 - \mu_n \sigma_m^2 \pm \sigma_m \sigma_n \sqrt{(\mu_m - \mu_n)^2 + (\sigma_n^2 - \sigma_m^2) \ln \left(\frac{A_m}{A_n} \right)^2}}{\sigma_n^2 - \sigma_m^2} \quad (4.14)$$

Using the equation 4.14 and taking the correct value, with as taken the signal with charge in the interval shown in

$$5.33pC < q < 15.83pC \quad (4.15)$$

With this procediment, some wrong signal are going to be peaked. But the numbers of signals that are not single photon electrons response are far less than the ones that are in the same interval of the histogram.

The mean single-photon electron signal, together with the mean signal of two and three photo-electrons signal are shown in figure 85.

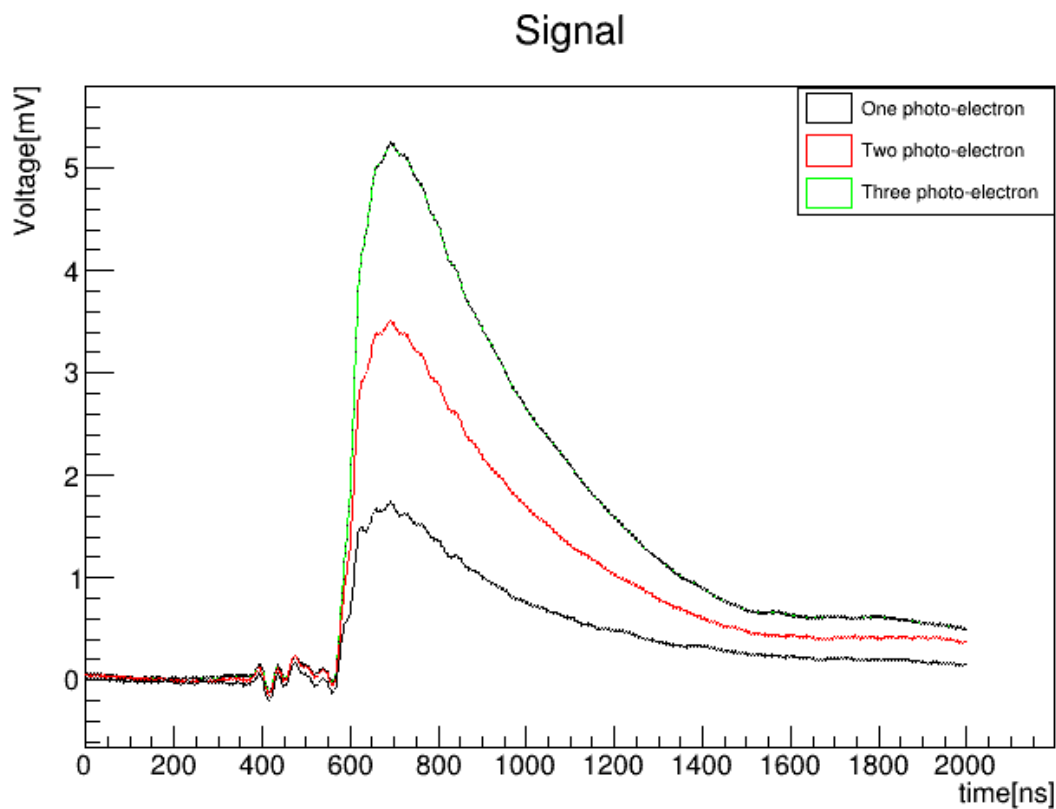


Figure 85 – Mean signal of one, two and three photo-electron generated

4.10 X-ARAPUCA response

The photons when its emitted by the argon it passes by the remission of TPB in the walls of cryostat, then the reemission of the PTP material in the light guide and its absorbed by the SiPM.

Mathematic this means that output voltage is shown in equation 4.16, where the symbol $*$ is the convolution symbol.

$$v_o(t) = I(t) * h_{TPB}(t) * h_{PTB}(t) * h_{SiPM}(t) \quad (4.16)$$

Where $h_{SiPM}(t)$ is the equation given in equation D.13, with the modification written in D.2.4.

The response from TPB and PTP can be written in a similar form of 3.1. The slow and fast component of TPB is 22 ns and 2.2 ns, respectively while the PTP slow component is around 50 to 300 ns and the fast less than 5 ns. ([60],[61],[62]).

The $I(t)$ is the luminosity intensity from argon and also can be given in the form 3.1, with slow component 1600 ns and fast around 6ns. Meanwhile the SiPM is around 10 ns.

Its possible to solve equation 4.16 using laplace transformation as shown in equation 4.17

$$V_o(s) = I(s)H_{TPB}(s)H_{PTB}(s)H_{SiPM}(s) \quad (4.17)$$

Using that the laplace transform of an exponential is given by equation 4.18.

$$e^{at} \longleftrightarrow \frac{1}{s - a} \quad (4.18)$$

Then equation 4.17 becomes 4.19

$$V_o(s) = \frac{A}{s + \frac{1}{\tau_s^{TPB}}} + \frac{B}{s + \frac{1}{\tau_f^{TPB}}} + \frac{C}{s + \frac{1}{\tau_s^{PTP}}} + \frac{D}{s + \frac{1}{\tau_f^{PTP}}} + \frac{E}{s + \frac{1}{\tau_s^{LAR}}} + \frac{F}{s + \frac{1}{\tau_f^{LAR}}} + \frac{G}{s + \frac{1}{\tau^{SiPM}}} \quad (4.19)$$

Each term in the equation is the an independent exponential, when applying the inverse laplace transform. The dominant term is the slow component of the argon.

4.11 Alphas and Muons

In the data sections which the trigger as via software (interal trigger) the trigger'source can be three: noise, alphas and atmospheric particles, most atmospheric muons 5.1.

To differentiate between the two types of particles (α and μ) its possible to calculate the charge in in the start of signal, going to called q_f (fast charge) and divide this value for the total charge of the signal. More specific the ratio shown in equation 4.20, where t_f is lower than T.

$$q_{ratio} = \frac{q_f}{q} = \frac{\int_0^{t_f} v(t)dt}{\int_0^T v(t)dt} \quad (4.20)$$

For particle like alphas where the singlet contribution is higher than the triplet contribution (3.2.1), the charge should be almost concentrate in the start of the signal. Meanwhile for muons the charge is more distributed along the signal.

The plot of the this ratio charge in relation of total charge is shown in figure 4.20 with 36V as bias. This ratio was chosen as the start integrating time as $4\mu s$, $t_f = 3.2\mu s$ and $T = 7\mu s$.

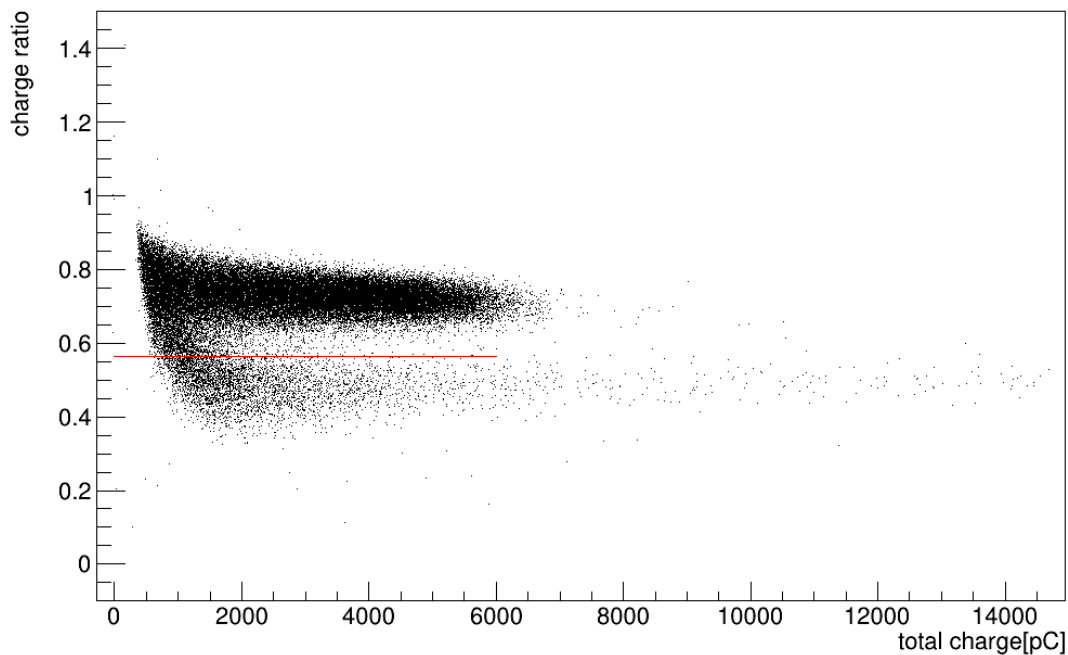


Figure 86 – Ratio charge in function of total charge

In the figure its possible to see a division that separates the alpha particles from muons. The point that separates both particles is choose making a histogram of the the ratio charge and finding the minimum between the two gaussian formed. In this case, the point that separates both particle is 0.564313.

In figure 87 show the plot for mean signal for alpha and muon.

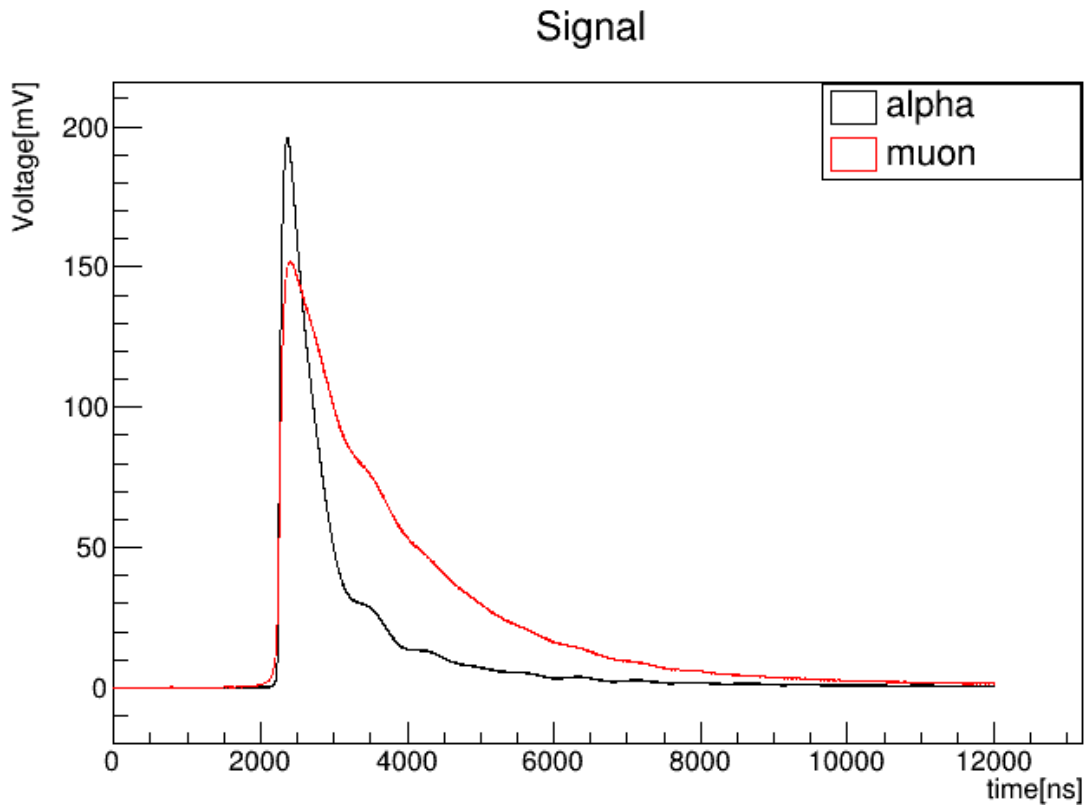


Figure 87 – Mean signal for muons and alphas

Using what was told in 4.10, fitting an exponential in the tail of the exponential we can estimate the slow constant time of the argon.

Making this fit in the muon waveform its found 1773 μs . While in the alpha its found 1753.5 μs .

4.12 Light Signal

The single photon electron ($h(t)$) response found nothing more is than the response of the system due to an unitary impulse ($\delta(t)$).

So given an light input ($l(t)$), its possible to find the output voltage making the convolution as shown in equation 4.21.

$$v(t) = h(t) * l(t) \quad (4.21)$$

To find the light input, given an output its possible to make a deconvolution to find what its seeked.

Other option is make a fourier transform of equation 4.21, giving equation 4.22

$$V(\omega) = H(\omega)L(\omega) \quad (4.22)$$

Isolating the fourier transform of the light input its obtained 4.23.

$$L(\omega) = \frac{V(\omega)}{H(\omega)} \quad (4.23)$$

And to obtain the input in time domain, its only needed to do a reverse fourier transform.

This procediment is more easier than doing the deconvolution algorithms. But there are two problems with this procediment, that arise from the fact that the time domain variable is discrete.

Since the time domain is discrete, its substituted the traditional fourier transform by the discrete fourier transform. The fourier transform of N samples in time domain will have N samples in frequency domain. Also the fourier transform of a sampled signal with frequency f_s , will be periodic from $-f_s$ to f_s .

Two signals with different number of samples and same sample frequency, in the frequency domain each point will be referent to differents frequency, and the division shown in 4.22 will not be valid. As consequence if the output signal and the impulse response have different number of samples, its needed to expand the lower one to the same number of samples of the larger one, putting a lot of zeros in the end of signal. This process is called zero padding.

The second problem is that the discrete fourier transform assumes that the time domain signal is periodic with period $\frac{N}{f_s}$. So the division in 4.22 will assume that the original signal is periodic and will give the wrong answer. To overcome this, its made a second zero padding expanding both signal with N samples to a size of minimum of $2N-1$.

Making the zeropadding in the mean muon signal, alpha mean signal and in the single photon eletron mean signal, its calculated the light input for the α particles and for the μ . This is shown in figures 89 and 88 for muons and alpha respectively.

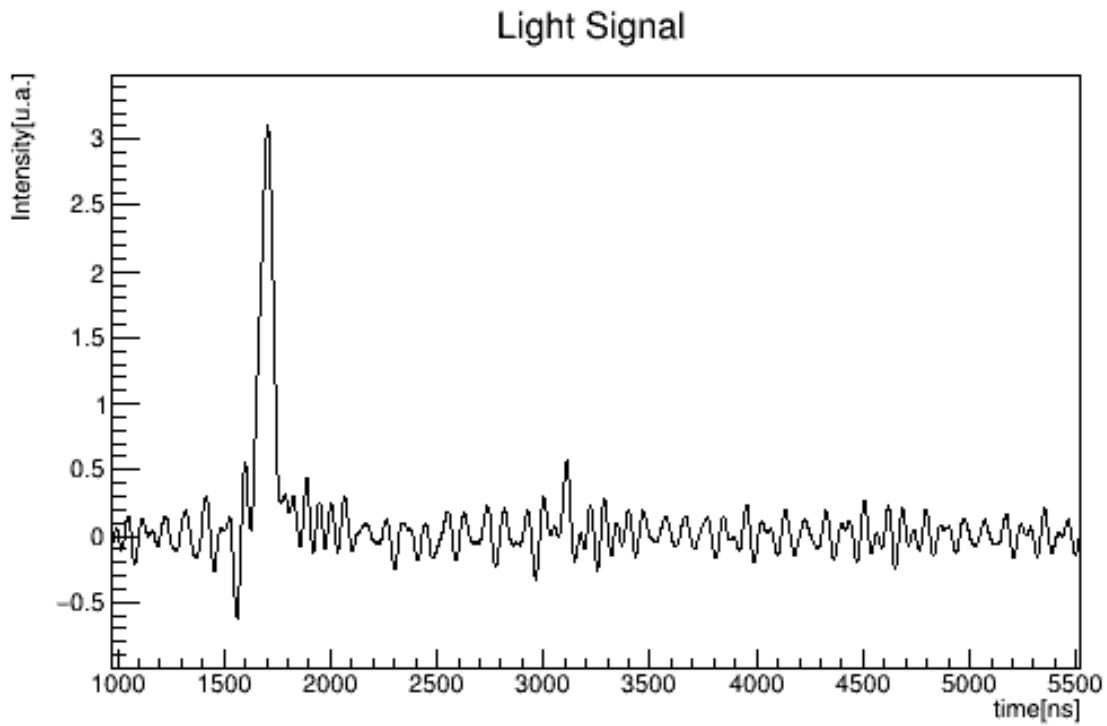


Figure 88 – Light signal for the alphas particles

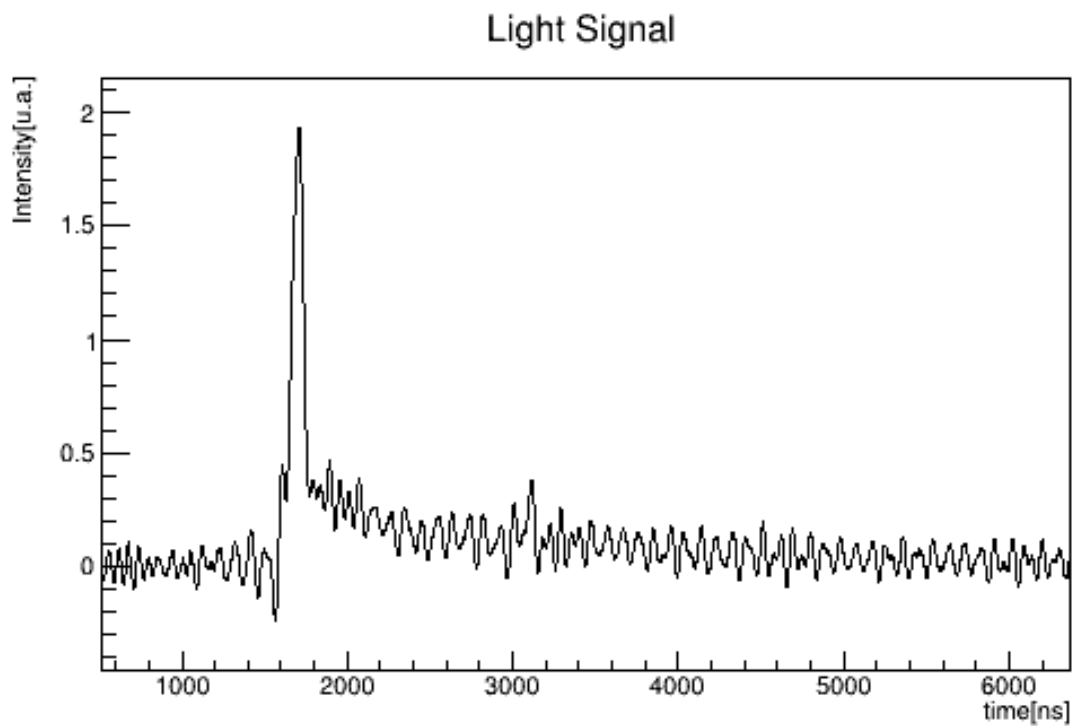


Figure 89 – Light signal for the muons

Fitting the sums of exponential slow and fast, for the muons it was found $24.43 \pm 0.08ns$ for the fast component and $1595.5 \pm 36.44ns$ for the slow component. Meanwhile for alphas $24.22 \pm 0.07ns$ for the fast component and $1659.62 \pm 39.18ns$ for the slow component.

4.13 Crosstalk

The notion that the peaks of the photon-electrons in the histogram presented in 4.8 follows an poisson distribution is only true in the absence of crosstalks. When we take the crosstalk along the distribution follow the generalized poisson [63].

The experimental probability for each photo-electron peak can be found integrating the respectively each gaussian of figure 84 .

The probability of each peak can be seen in table 8.

peak(k)	Integral(n event)	Integral error	percentage (%)	percentage error (%)
0	12037.4	67.1906	19.548	0.1091
1	12434.7	76.7709	20.193	0.1247
2	11266.2	80.0172	18.296	0.1299
3	8120.79	97.5873	13.188	0.1585
4	5451.55	121.367	8.853	0.1971
5	4071.61	168.126	6.612	0.2730
6	3227.6	188.611	5.241	0.3063
7	1452.35	112.642	2.359	0.1829
8	740.58	70.7882	1.203	0.1150
9	853.159	41.4057	1.385	0.0672
Total	61579	0	100	0

Table 8 – Table with integral and percentages of each photon electron

The generalized poisson distribution can be written as equation 4.24, where p is the probability of crosstalk and λ is the same presented in 4.8.

$$P[k] = \frac{1}{k!} \left(\frac{d^k}{ds^k} \left(e^{\frac{\lambda(s-1)}{1-ps}} \right) \right) \Big|_{s=0} \quad (4.24)$$

From this definition we can calculate $P[0]$ and $P[1]$ as shown in equations 4.25 and 4.26.

$$P[0] = e^{-\lambda} \quad (4.25)$$

$$P[1] = e^{-\lambda}(1 - p) \quad (4.26)$$

So the mean of photoelectrons detected, without counting overvoltage can be calculated as shown in 4.27.

$$\lambda = -\ln P[0] = 1.63 \pm 0.01 \quad (4.27)$$

Meanwhile the probability of cross talk can be found as shown in equation 4.28.

$$p = 1 - \frac{P[1]}{\lambda P[0]} = 0.3671 \pm 0.0026 \quad (4.28)$$

So this means that each trigger event, a mean of 1.63 photons were detected, and the crosstalk probability is given by $(36.71 \pm 0.26)\%$.

To get a better result its possible to fit the experimental probabilities peak each the teorical ones and get the best result for p and λ . The result of the fit is shown in figure 90.

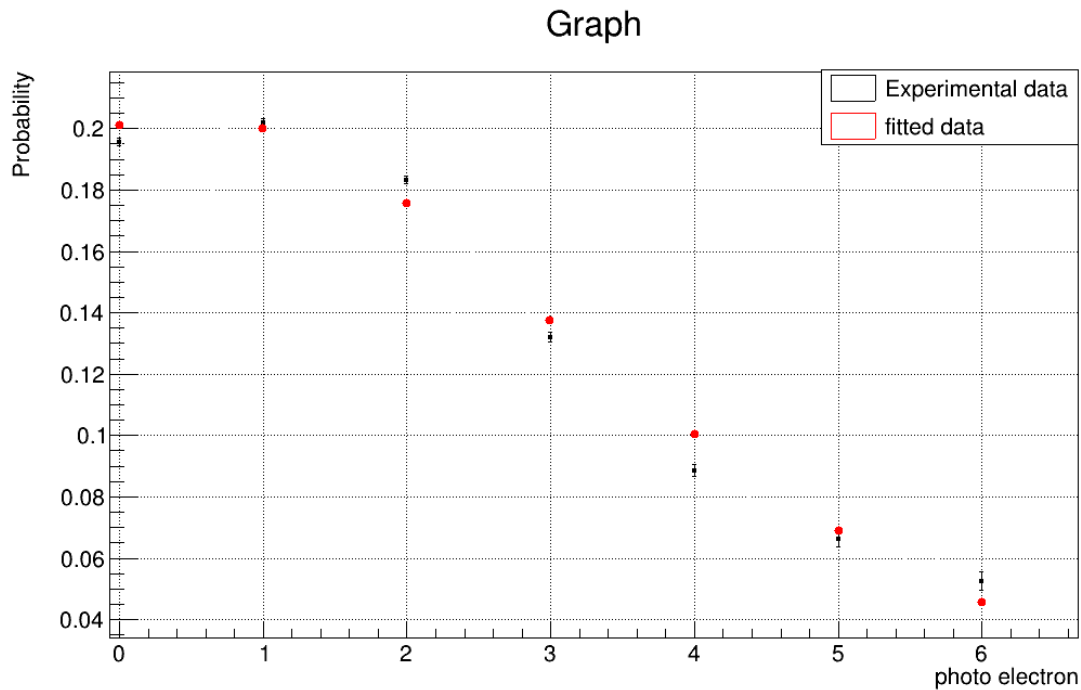


Figure 90 – Crosstalk fit

The crosstalk probability is $38.11 \pm 1.43\%$.

4.14 Efficiency

Its possible to calculate the efficiency of the X-ARAPUCA, plotting the charge histogram of alpha particle and comparing with the simulated data presented in 4.4. The plot of the the mentioned histogram is found in figure 91, where the charge its divided by the photo-eletron charge ($10,032pC$), to the x-axis becomes photo-electrons detected. The initial peak in the histogram is background noise.

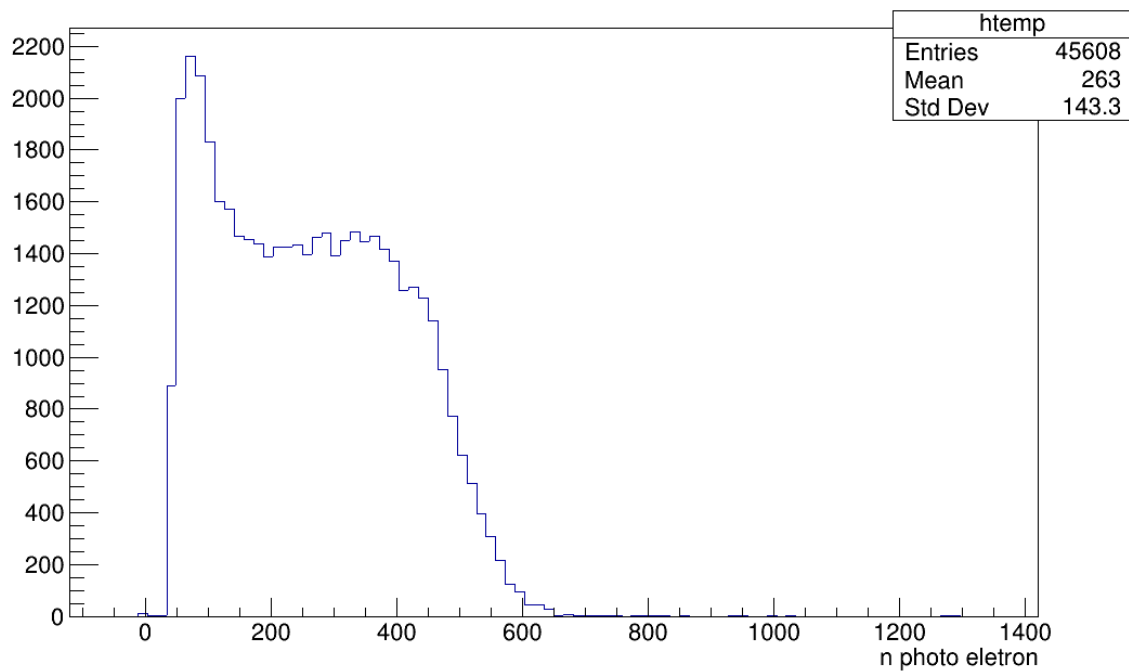


Figure 91 – Histogram of detected photo-electron for the case of the alpha particles

The goal is to fit the simulated histogram to the experimental histogram using this equation 4.29.

$$h_{fit}[\alpha n] = \beta \cdot h_{sim}[n] + A \cdot e^{-\tau n} \quad (4.29)$$

What this function do is to convert a bin of the original simulated histogram to an inferior bin, since α must be less 1. Actually α is nothing more than the efficiency of the device. It is also added an exponential in the start of the histogram to fit with the noise in experimental setup. In the experimental histogram there is the effect of the threshold that cuts the start of the histogram, so to take that in account in both histogram, the fitted and the experimental, it was filtered the entries less than 200 photo-electrons.

Using the MINUIT package (MInimization by NUnused Information Theory) it was fitted using χ^2 method the best result for the free parameters (α, β, A and τ). The result of the fit is shown in figure 92.

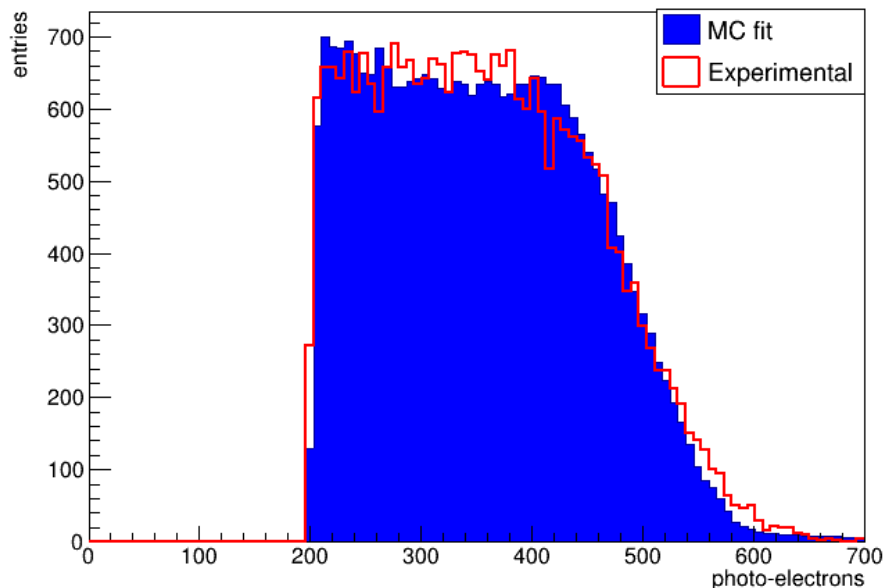


Figure 92 – Efficiency fit

Also for the explained fit, it was used a fifth fit parameter named σ , that to each bin "n" a new set of bins is created following the equation shown in equation 4.30. The final fit is then the sum for all the n of the equation 4.30, as shown in equation 4.31.

$$h_{fit}^n[k] = h_{fit}[n] e^{-\frac{[k-n]^2}{2\sigma^2}} \quad (4.30)$$

$$h_{final}[k] = \sum_n h_{fit}^n[k] \quad (4.31)$$

The values of the fit are shown in 4.32.

$$\begin{aligned} \alpha &= 0.0155 \\ \beta &= 0.5001 \pm 0.0009 \\ A &= 969 \pm 54 \\ \tau &= 0.0080 \pm 0.0002 \\ \sigma &= 4.41 \pm 0.04 \end{aligned} \quad (4.32)$$

So the efficiency is (1.55%). But since there are two channels it's needed to multiply by 2 for the result. To take into account the crosstalk, it's needed to divide the result by 1+0.38. For last, since the simulation didn't assume the efficiency of TPB as 70%, it's needed to divide this value. The final efficiency is 3.2%, as calculated in equation 4.33.

$$\epsilon = \frac{0.0155 \times 2}{1.38 \times 0.7} = 0.032 \quad (4.33)$$

The error can be found propagating the error of the crosstalk and the single photon-electron charge. The error is 0.0003. So the efficiency is $(3.20 \pm 0.03)\%$.

5 Cosmic Rays

This section will talk about the atmospheric muons, the particles that are going to be used to test the C-Arapuca prototype.

Muons are leptons with a negative charge, as explained in section 2.1. The main difference with the electron is that it's 207 times heavier. For this reason, muons are unstable particles and decay on average in $2.2 \mu\text{s}$ in an electron, an electron neutrino, and anti muon neutrino as can be seen in Feynman diagram of figure 93.

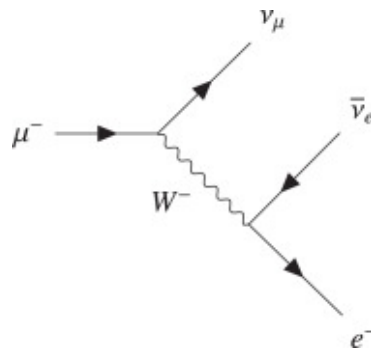


Figure 93 – Muon Decay

The main source of muons on Earth is the Cosmic Rays, which are separated into primaries and secondary particles. The primaries are particles that come from outside Earth's atmosphere. The sources can be the Sun, galactic (coming from the milk way), or extragalactic (coming outside the milk way).

The main part of the cosmic rays originate outside our solar system and are composite of stable particles, the main compound being protons. In figure 94 it's possible to see the flux of protons (and another nucleons) in the cosmic rays as a function of energy.

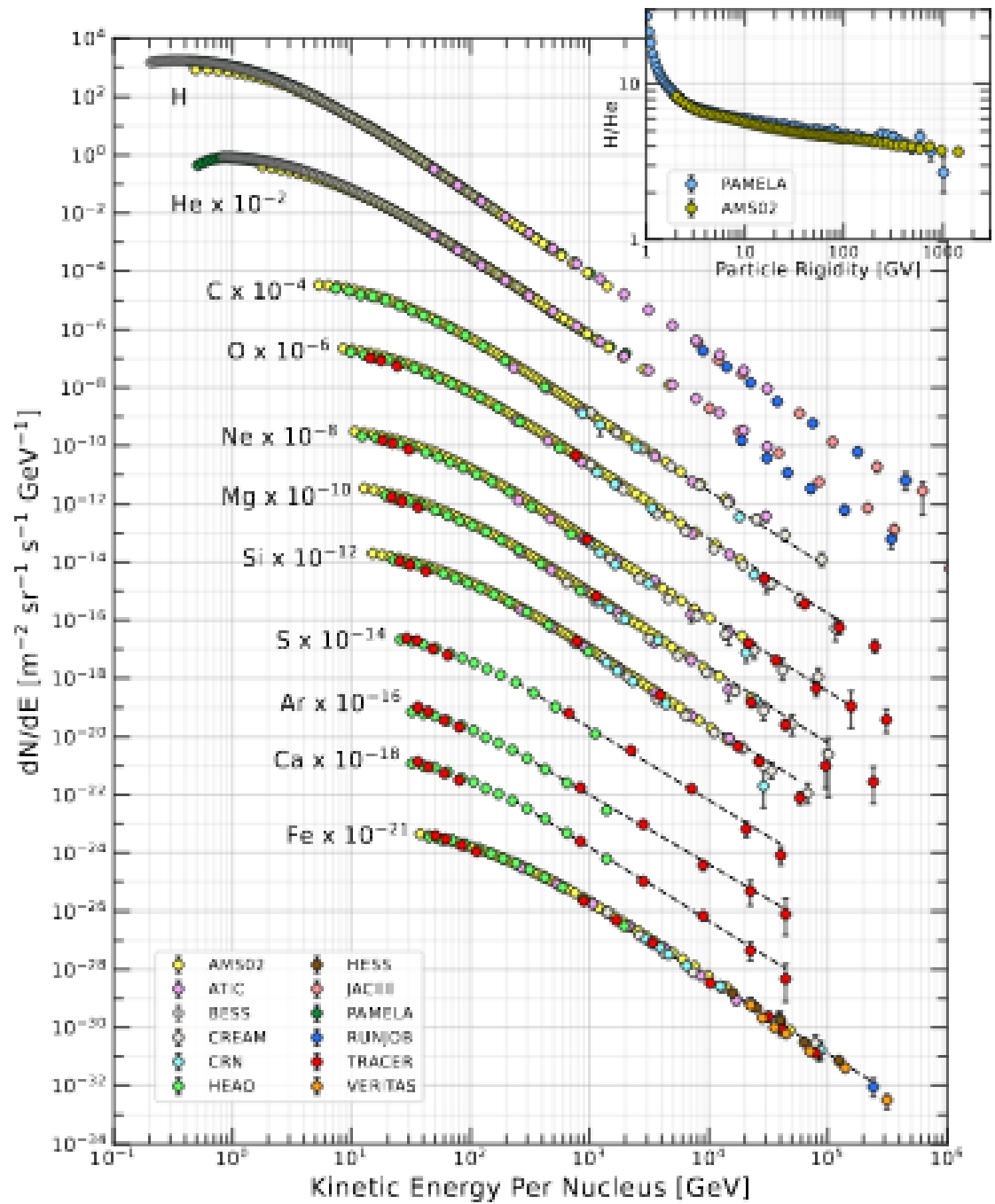


Figure 94 – Flux of cosmic rays protons as a function of energy [20]

In the figure, it's possible to note that for higher energy, the distribution follows a power law in the form of equation 5.1. The α exponent is approximately 2.8.

$$\Phi(E_p) \propto E_p^\alpha \quad (5.1)$$

The secondary particles are formed when the primaries interact with the Earth's atmosphere. This interaction produces other baryons (protons and neutrons), charged pions, neutral pions, charged kaons, and neutral kaons. The baryons continue to interact with the atmosphere, producing more particles. The charged pions decay quickly (26 ns) mostly in neutrinos and muons as shown in equations 5.2.



Meanwhile, the neutral pions decay most in photons as shown in the equation. 5.3.



The kaons decay in muons and pions, which will decay in muons and neutrinos as explained above.

The particles created in the interaction interact again with the atmosphere and this generates a cascade process, named extensive air shower, a schematic diagram of this process be seen in figure 95.

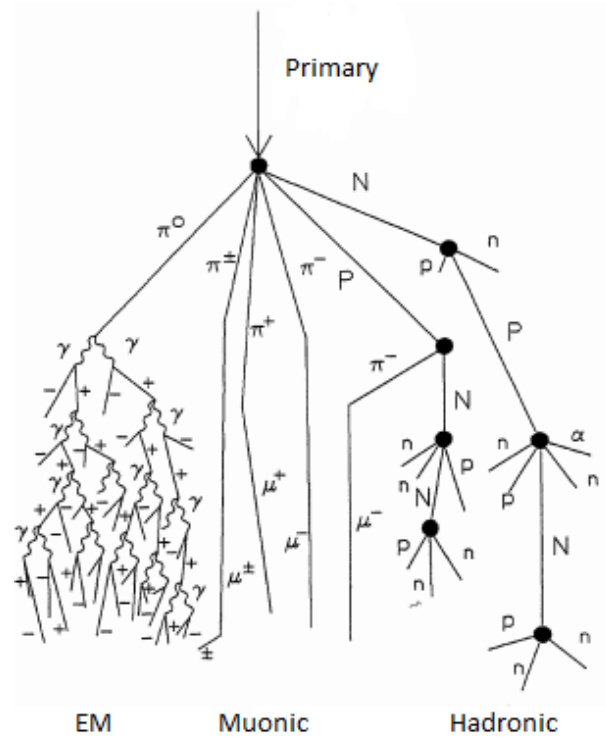


Figure 95 – Primaries cosmic rays creating secondaries [21]

5.1 Atmospheric Muons

The muons practically travel in a straight line in direction of the Earth. This happens because since the muons are leptons, they don't interact with the nucleus in the atmosphere via the strong force. Also since it's 200 times heavier than the electrons, they just push away the electrons of the atmosphere out of the way.

Most of the muons are created at 15 km with a mean energy of 6 GeV. This gives him a start velocity given by equation 5.4.

$$\beta = v/c = \sqrt{1 - \left(\frac{E_0}{E}\right)^2} = \sqrt{1 - \left(\frac{105.66}{6000}\right)^2} = 0.99984 \quad (5.4)$$

And the Lorentz factor can be calculated as equation 5.5 shows.

$$\gamma = \frac{E}{E_0} = \frac{6000}{105.66} = 56.79 \quad (5.5)$$

Since the velocity is relativistic, to calculate the depth that the muon can travel

before it decays, it needed first to calculate the decay time in a referential inertial seeing the muon with the speed calculated in equation 5.4. The decay time in this referential is given by equation 5.6.

$$\Delta t = \gamma \tau_{\mu} = 56.79 \times 2.2 \mu s = 125 \mu s \quad (5.6)$$

So the mean depth with the muon can travel, assuming no energy loss in the travel is given by equation 5.7.

$$\Delta x = v \cdot \Delta t = c \cdot \beta \cdot \Delta t \approx 38 km \quad (5.7)$$

This value is enough for the mean muon to travel 15 km of the Earth's atmosphere and arrives at sea level.

The muon flux as a function of muon energy at sea level can be seen in figure 96

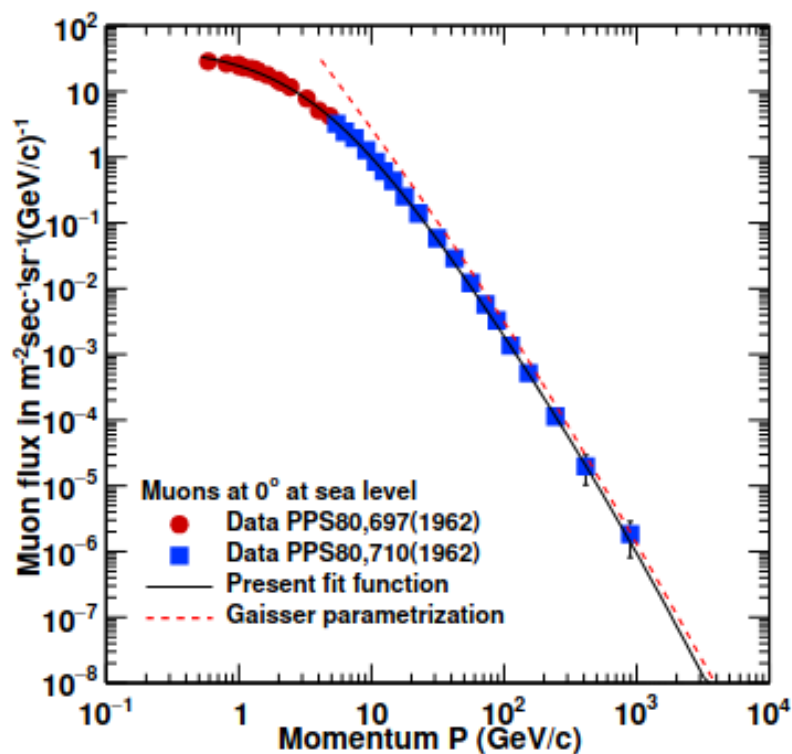


Figure 96 – Vertical muon flux as a function of momentum [22]

As expected the muon flux also follows a power law like the cosmic rays seen in figure 94.

5.1.1 Energy Loss

As the muon travels in the atmosphere it lost energy due to stopping power. This can be written as shown in equation 5.8.

$$\frac{dE}{dx} = a(E) + b.E(E) \quad (5.8)$$

Where the term "a(E)" is the term related to electronic interactions (inelastic scattering with electrons) and b is the term related to energy loss due to radiation.

At low to medium energies the term that dominates is electronic interactions. At medium energies, the electronic loss is modeled by the Bethe Bloch equation [8].

At high energies, the term that dominates is radiative loss. The radiative term is the sum of three components: bremsstrahlung, pair production and photonuclear interactions.

For the atmospheric muons, the main reason for the energy loss in the atmosphere is due to electronic interactions. Figure 97 is shown the energy loss of a muon in copper as a function of its kinetic energy.

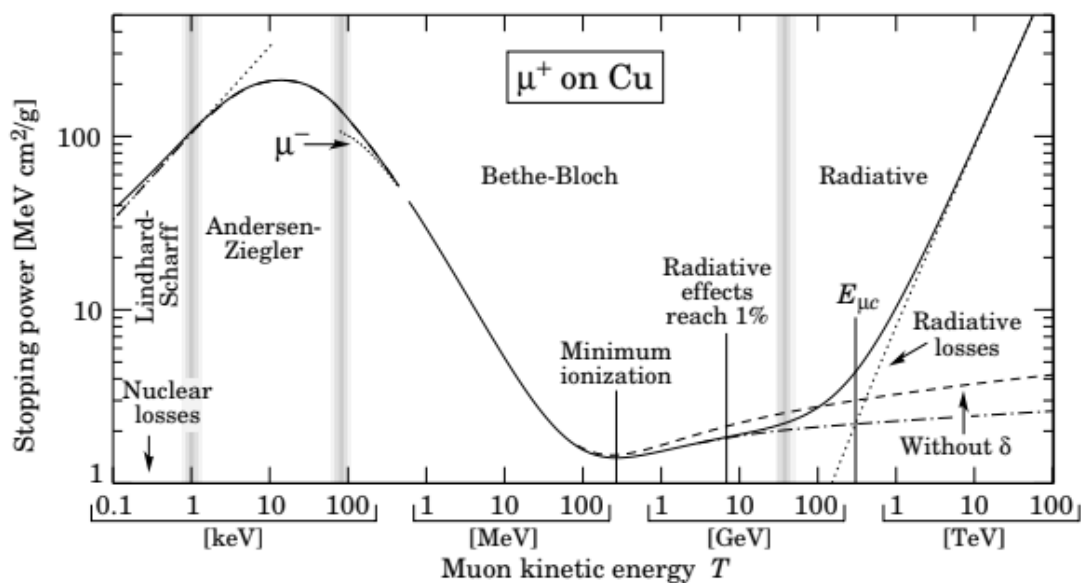


Figure 97 – Stopping power of muon in cooper [23]

Most of the muons encounter themselves in the central plateau or near the plateau in figure 97, losing almost the same quantity of energy per distance traveled per density of the medium.

The muons lost around 2 GeV of energy during the travel to the surface of the Earth. So the muons arriving at the surface have a mean energy of $6\text{GeV} - 2\text{GeV} = 4\text{GeV}$ and encounter themselves in the region of minimum ionization.

In figure 98 it is possible to see the vertical flux of the muons at different altitudes.

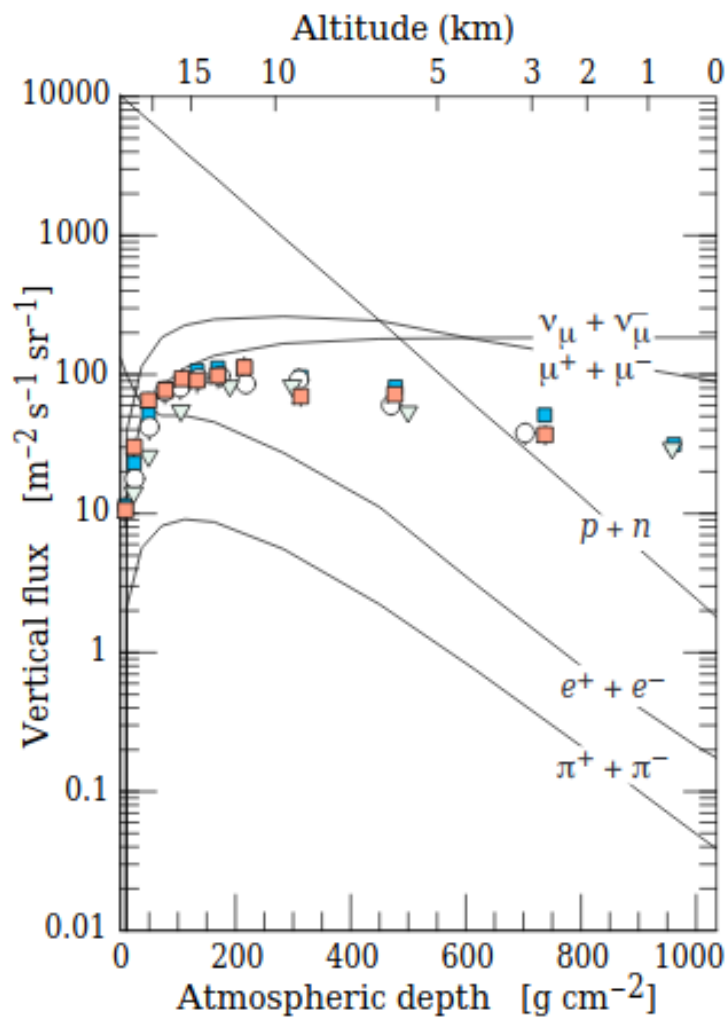


Figure 98 – Flux of vertical muons and another particle as function of altitude [20]

At the graph above the height of 15km the muon flux increase, because the cosmic rays are interacting with more layers of the atmosphere and creating more muons in the process. However the flux doesn't increase forever, and as those muons come to the direction of the surface the fewer energetic ones start to decay. So that's why the flux decreases when altitude decreases.

The flux is also strongly dependent on the zenith angle. For higher the zenith angle more the muons travel in the atmosphere to arrive at the surface, so more energy is lost and less is the flux expected. Figure 99 is show the plot of the zenithal muon flux to vertical muon flux in the function of zenith angle to different energy.

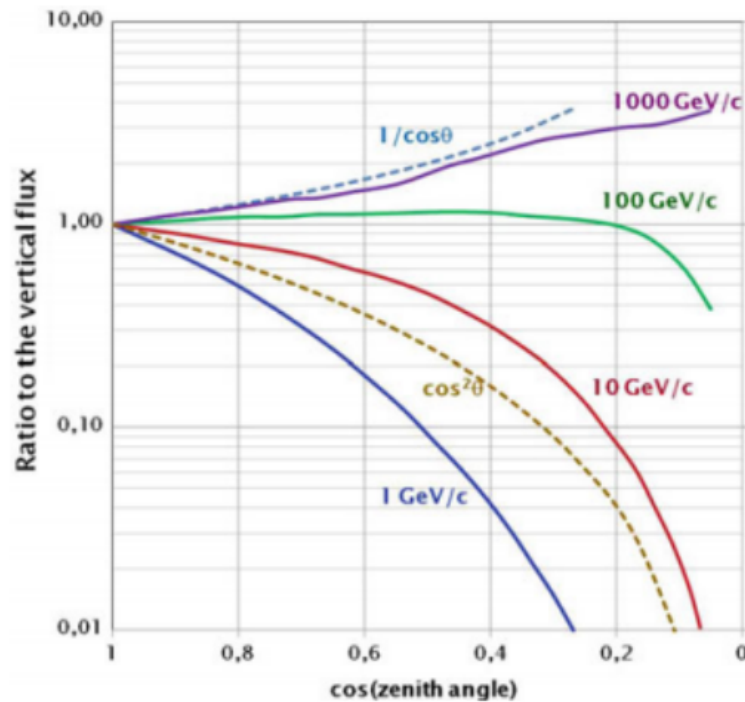


Figure 99 – Ratio of zenith muon flux to vertical flux [24]

For momento lower than 100 GeV/c the zenithal flux lowers with energy. For muons next to 3GeV of energy the flux can be approximated by a \cos^2 dependence as can see in equation 5.9 [64]. The muons used in this work have about this angular distribution.

$$I(\theta) = I(0) \cdot \cos^2(\theta) \quad (5.9)$$

6 Cherenkov Radiation

Since the C-Arapuca will use Cherenkov radiation to detect particles, this section will explain the source of Cherenkov radiation and show its important characteristics about it.

The Cherenkov radiation is the radiation emitted by electric charges moving in a medium faster than the speed of light in that medium, emitting a light cone, very similar to the effect of a sonic boom. The geometry of the Cherenkov radiation can be seen in figure 100.

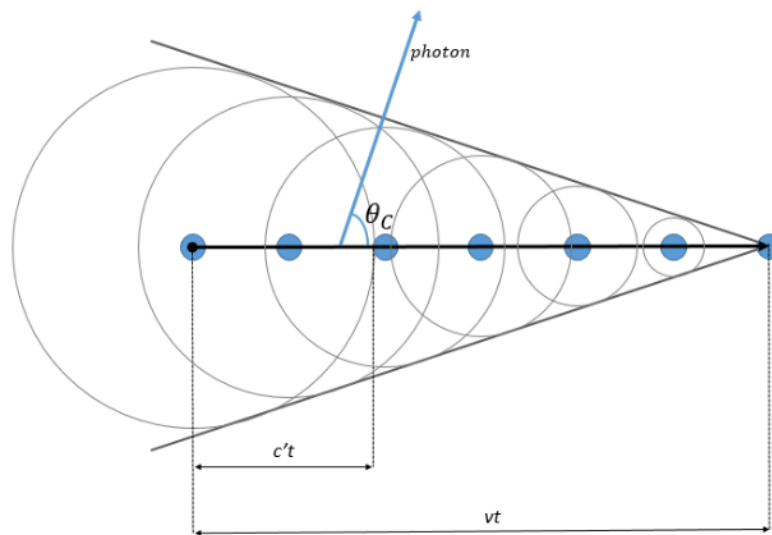


Figure 100 – Scheme of Cherenkov Radiation [21]

The speed of light in a medium is given by equation 6.1.

$$v_{medium} = \frac{c}{n_{medium}} = \frac{c}{\sqrt{\epsilon\mu}} \quad (6.1)$$

If a particle is slower than v_{medium} , the polarization in the medium is symmetric in the direction of the propagation of the particle. As result, the electromagnetic waves sum up destructively, so there will be no resultant wave.

But if the particle is faster than v_{medium} ($\beta > 1/n_{medium}$) the polarization is asymmetric and as a result, the waves sum up constructively and a wave appears.

The opening angle of the light cone (θ_c) is given by 6.2.

$$\cos(\theta_c) = \frac{\Delta x_\gamma}{\Delta x_q} = \frac{v_\gamma \cdot t}{\beta \cdot c \cdot t} = \frac{c}{\beta \cdot c \cdot n_{\text{medium}}} = \frac{1}{\beta \cdot n_{\text{medium}}} \quad (6.2)$$

By equation 6.2, it's possible to note that the faster the charged particle, the higher will be angle θ_c of the light cone. The max angle happens when the particle is near the vacuum speed of light ($\beta \approx 1$). For example, in water, the max angle is given by equation 6.3.

$$\theta_{H_2O}^{max} = \arccos \frac{1}{n_{H_2O}} = \frac{1}{1.33} = 41.24^\circ \quad (6.3)$$

It's also possible to calculate the minimum energy and momentum for a particle to emit Cherenkov photons in a medium. This is given by equation 6.4 and 6.5.

$$p_{min} = \gamma m \beta c = \frac{mc}{n_{\text{medium}} \cdot \sqrt{1 - \left(\frac{1}{n_{\text{medium}}}\right)^2}} \quad (6.4)$$

$$E_{min} = \gamma m c^2 = \frac{m c^2}{\sqrt{1 - \left(\frac{1}{n_{\text{medium}}}\right)^2}} \quad (6.5)$$

So for example the muon minimum momentum and energy for Cherenkov radiation is 120 MeV/c and 160MeV/c² respectively. For electron is 0.58 MeV/c and 0.77MeV/c².

The Cherenkov energy spectrum can be seen in figure 101. The full derivation of the Cherenkov spectrum is in Appendix C.

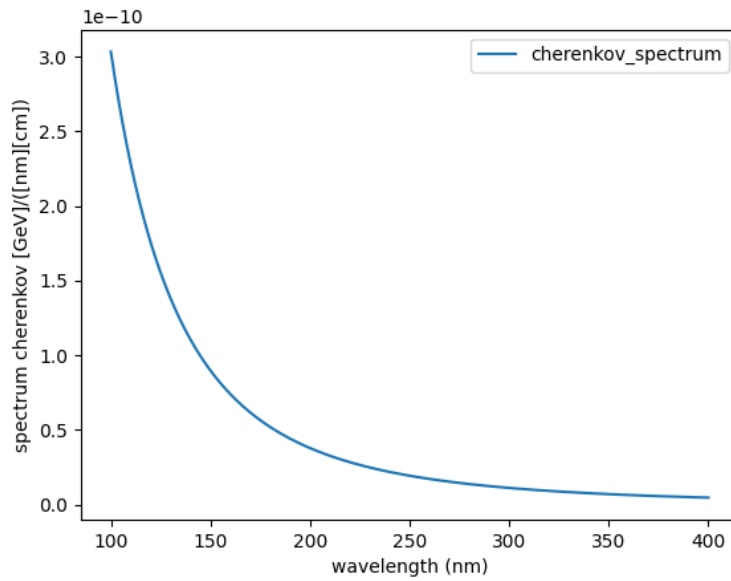


Figure 101 – Spectrum of Cherenkov radiation in water for a particle with charge e and $\beta = 0.9997$

So the energy radiated decreases as the wavelength increases. So a charged particle faster than the speed of light of the medium emits more blue, violet and UV photons. But at a wavelength lower than UV the equation derived starts to fail and the spectrum starts to decrease. This happens because the electric permittivity and magnetic permeability are functions of the frequency or wavelength. At lower wavelengths this causes the medium to start to absorb the photons emitted.

The density of emitted Cherenkov photons spectrum is shown in figure 102.

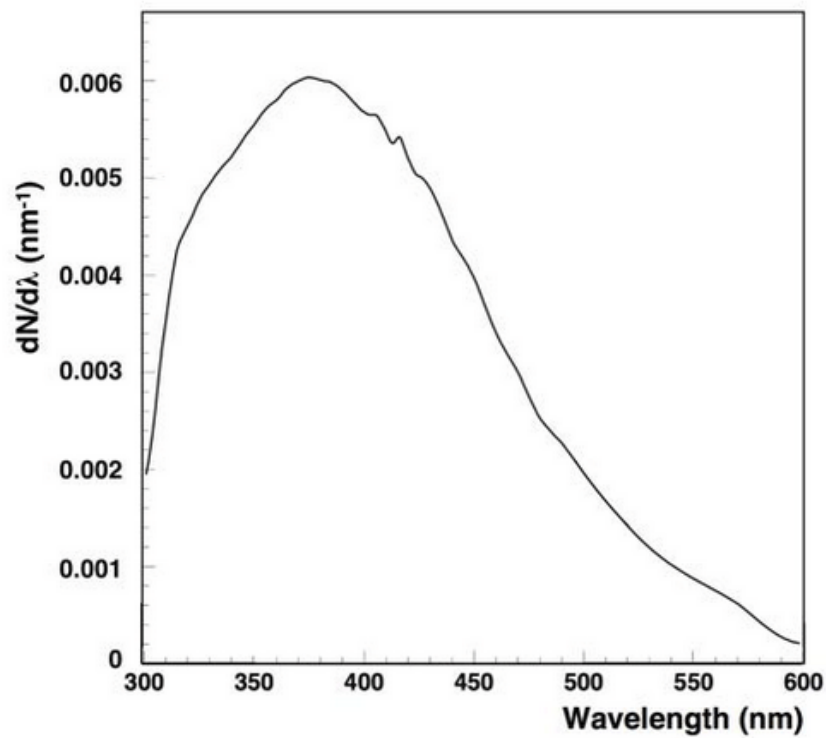


Figure 102 – Density of Cherenkov photons. In the plot we can see the effect of absorption in low wavelengths explained in the text [25]

One last thing, as the particles move around the medium, they lost energy in form of Cherenkov photons and their velocity decreases. But this loss of energy is so tiny about his energy, that we can consider the speed of the particle constant.

7 Test Stand for the characterization of C-ARAPUCA for water Cherenkov light

This section will explain the setup of the test of C-Arapuca. It is separated into two setups, the first one is the preliminary setup that was used to test the viability of the experiment using the muon peak, which are atmospheric muons of 4GeV in the region of minimum ionization (5.1). The second setup is the final setup to test the C-Arapuca itself. The results will be compared to a PMT that will be installed together with the C-Arapuca.

7.1 Preliminary Setup

7.1.1 The Barrel

For the C-Arapuca experiment, first, it was necessary to prepare the water barrel, seen in figure 103. The barrel is made of steel and has a height of 849 mm and a diameter of 610 mm, containing an internal volume of 200 liters.



Figure 103 – Preliminary barrel

Nineteen holes were made in the lid. Of these holes, the largest with a diameter of 51.6 mm is for the passage of the photomultiplier socket. Four holes with a diameter of

6.3 mm were drilled for the passage of the screws that will hold the PMT in place, all four equally spaced from each other and positioned on a radius of 75 mm from the center of the PMT hole.

For the passage of the signal and power cables of the C-Arapuca SiPMs, eight holes with a diameter of 9.5 mm were made. Half of them will be for the power supply signal and the other half for the signal generated by the device. Four holes of 5.5 mm were made for the fixation of the CArapuca support. A 16 mm diameter hole was made for fixing the temperature sensor connector. Finally, in the center of the lid, a 2 mm hole was made for the passage of the optical fiber

Next, the barrel was coated with Tyvek, a light-diffusing fabric. The Cherenkov photon produced by the muon inside the water is reflected in arbitrary directions. Therefore, there will be no privileged region to place the detectors. The Tyvek was attached to the bottom of the barrel using a metal ring. To fix the top part, the material was cut into strips as shown in Figure 104.



Figure 104 – Tyvek in the barrel

The purified water was produced at the *Centro de Tecnologia e Informação (CTI)* Renato Archer. The measured resistivity of the water was 18.2 M Ω .cm. Then, the barrel was filled with this water using 20-liter jugs. Water was transferred from the jug to the barrel 9 times, so the barrel was filled with a total of 180 liters of water. Since the volume is linearly proportional to the water column level, we can approximate the water column level as shown in equation 7.1.

$$h = \text{Barrel height} \times (\text{Water volume}) / (\text{Barrel volume}) = 764\text{mm} \quad (7.1)$$

7.1.2 Electronics and softwares

For the electronic and code tests, the 4-channel 12-bit, 250 MHz CAEN DT5720B digitizer is being used. How a PMT works is explained in Appendix D.1.

There are several ways to acquire the data, and they are:

- The DAQ Linux algorithm, which already saves data in .root format;
- The wavedump program provided by CAEN, which saves data in binary or text file formats.
- Finally, the Caenscope program provided by CAEN, which operates similarly to an oscilloscope.

For the last two options, an additional program is required to read the generated files and convert them to the root format. The digitizer has 12 bits of resolution and can sample signals up to 2 V in amplitude. Therefore, the digitizer has a precision of $2000\text{mV}/(2^{12} - 1) = 0.49\text{mV}$.

To amplify the signal the SiPM's signal is used the already explained APSAIA.

7.1.3 PMT

It was installed the Philips XP2040 photomultiplier tube (PMT) with a 110 mm photocathode, as shown in figure 105, on the barrel lid.



Figure 105 – PMT used in the setup

The PMT Spectral sensitivity is shown in figure 106. The gain of the PMT is in the order of 10^7 .

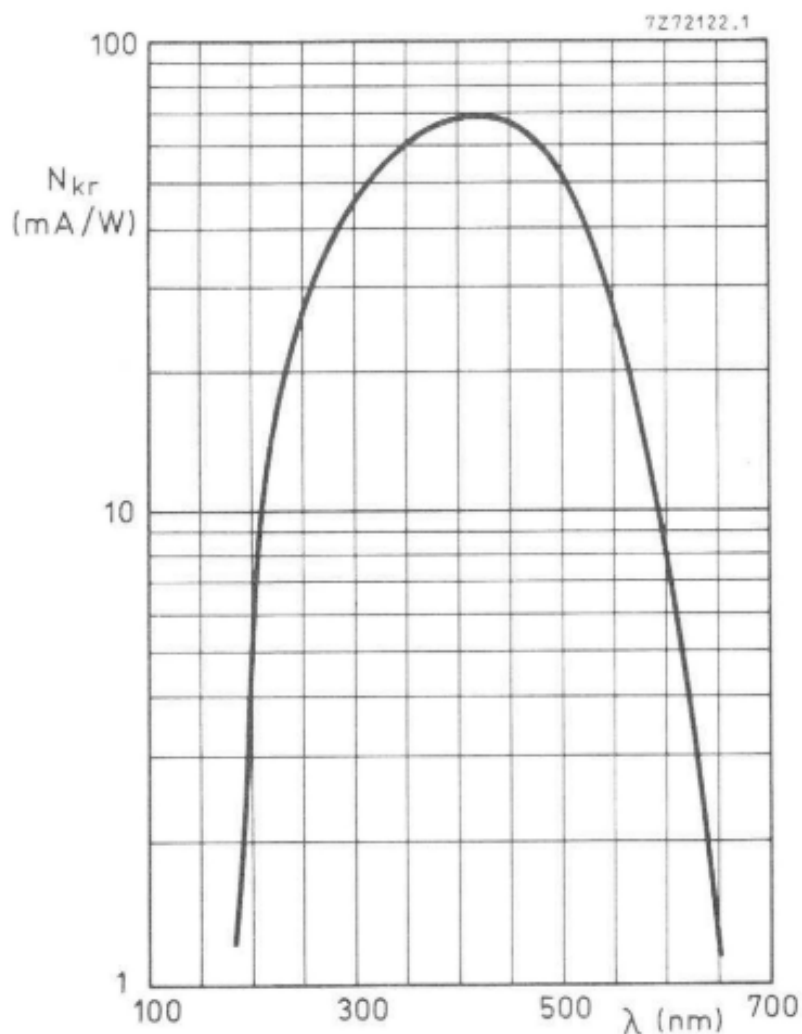


Figure 106 – Spectral sensitivity of the PMT [26]

The method used to ensure that no light was entering the interior of the barrel was through the voltage and current relationship applied to the PMT decoupled voltage divider. With this result, it is possible to verify if the system is optically isolated from external light, as we know that the electrical current that passes through the PMT is less than 1% of the total current.

When installing the PMT and conducting tests again, it was identified that the water drum was becoming charged, as a spark appeared when touching it. When measuring the voltage relative to the ground, it was identified that its voltage was practically the same as the voltage applied by the high-voltage source.

To solve the problem, the electrical diagram of the voltage divider shown in Figure 107 was made. In the figure, "Sx" are the dynodes of the PMT, "g1", "g2", and "acc"

are the PMT electrodes, "a" is the anode, and "k" is the cathode.

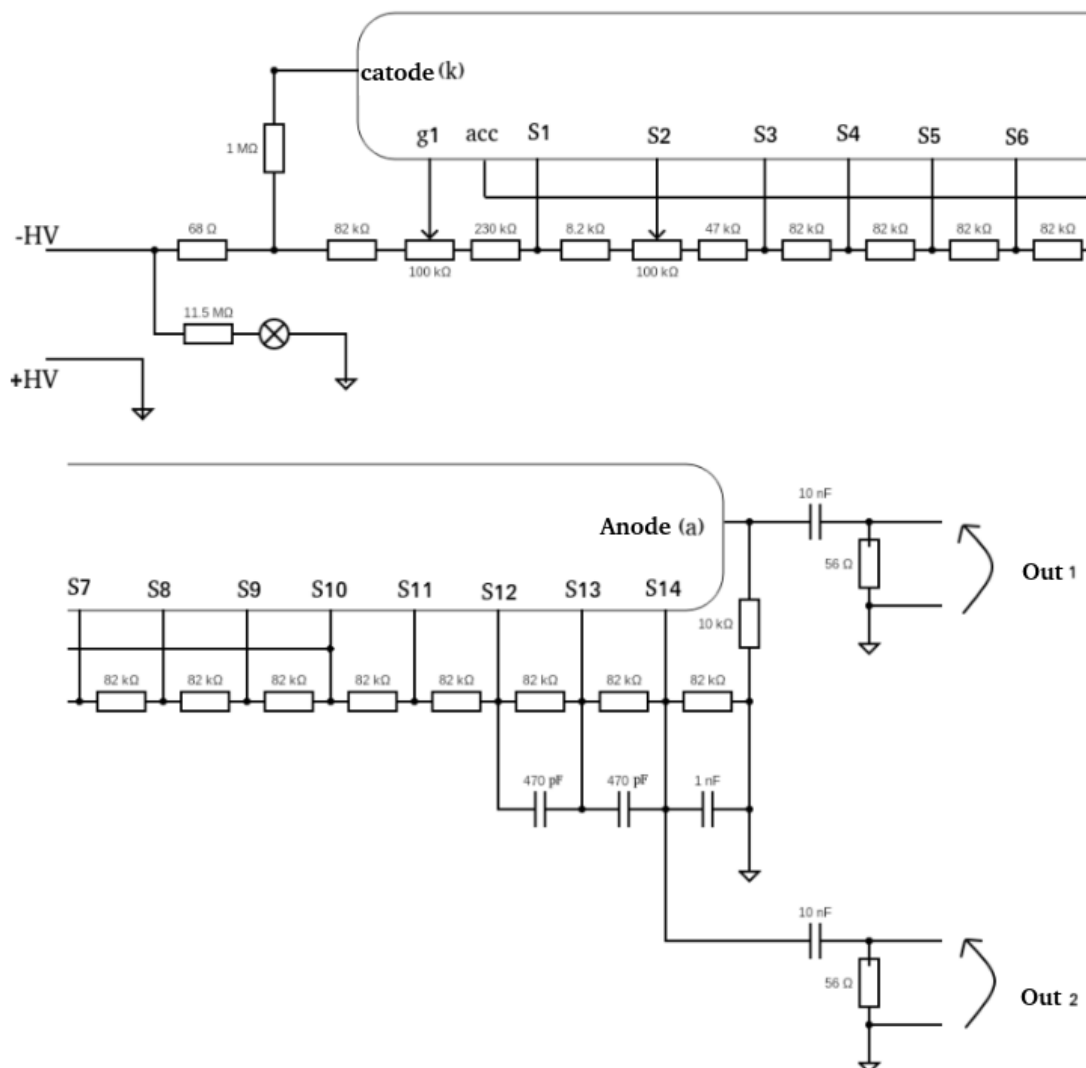


Figure 107 – Voltage divisor electric schematic

Observing figure 107, it was noticed that there is a high impedance of 1 M Ω between the negative high voltage and the cathode. Therefore, the voltage between "HV" and the cathode is almost the same. In addition, the existence of a conductive resin linking the cathode to the external point was observed externally to the PMT, as shown in figure 108. This external paint was verified to be a conductive material.



Figure 108 – Conductive material on PMT

Therefore, what was happening is that the external paint was charged with high voltage and in contact with the water, connecting the barrel to the cathode. To solve the problem, the conductive tape was scraped off and epoxy glue was applied to prevent water from coming into contact with any remaining traces near the black-colored raised area seen in Figure 108.

With all this procedure done and the barrel closed again, the light test was performed again, measuring the input voltage and current. The result is shown in table 9.

7.1.4 Muon peak

With the setup, it was configured the system to trigger with an internal baseline to catch the Cherenkov light emitted by the muons passing by the water in the barrel.

To study the system it is possible to make the charge histogram and the amplitude histogram. The results are shown in figures 109 and 110.

High voltage (V)	Current input with no PMT connected (μA)	Current input with PMT connected and barrel shorted (μA)	Current input with PMT connected and barrel no more shorted (μA)
100	57	56	57
300	204	204	204
500	351	351	351
700	498	498	497
900	644	646	645
1100	792	792	792
1300	940	940	940
1500	1089	1091	1088
1700	1238	1240	1239
1900	1387	1391	1389
2100	1537	1542	1538

Table 9 – Results of the values in the voltage divisor

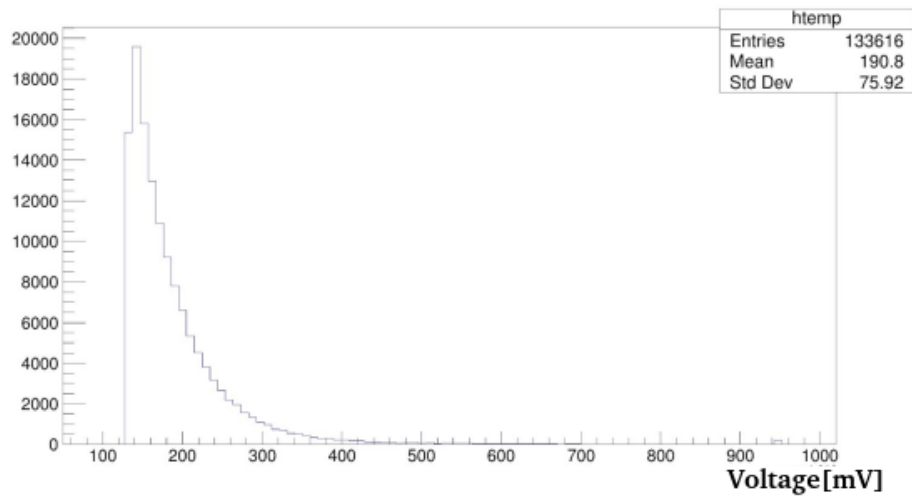


Figure 109 – Amplitude histogram

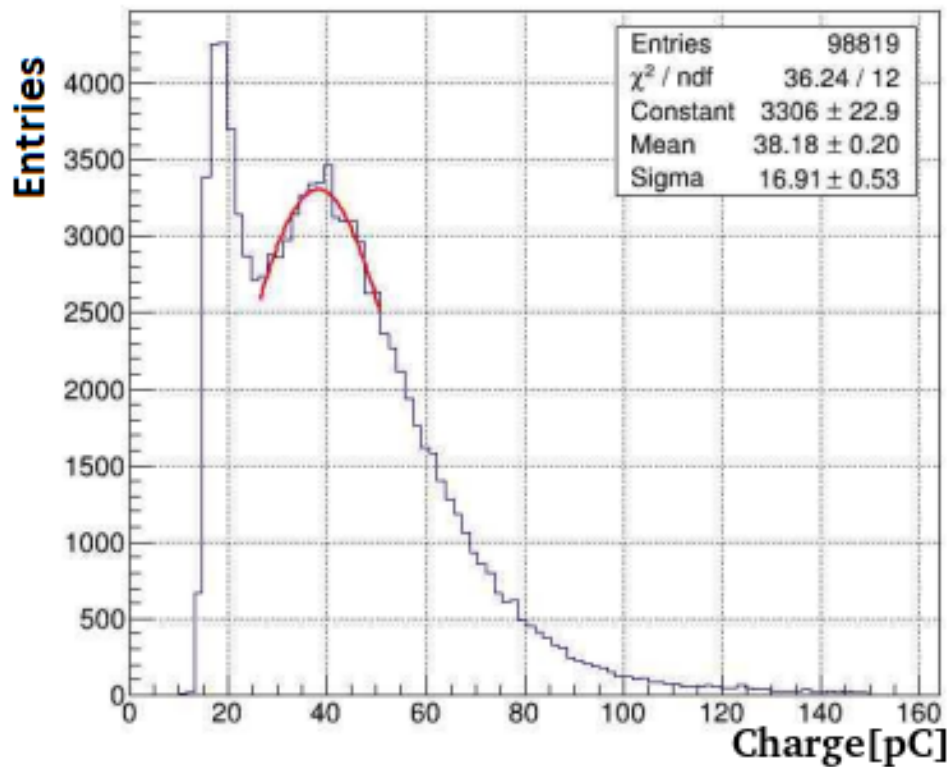


Figure 110 – Charge histogram. The parameters in table are the number of entries in the histogram, the value of the χ^2 fit using a gaussian fit (the red function), and the 3 fit parameters (constant, mean and standard deviation)

As can be seen from figure 110, there are two peaks in the charge histogram. The first peak is associated with noise, and the second peak is associated with muons.

To verify the quality of the water, a charge histogram was generated as a baseline model with a supply voltage of 2100 V and a trigger value of 100 mV. A Gaussian is fitted to this histogram, and the mean and standard deviation are observed. The mean charge is 38.18 pC with a standard deviation of 16.91 pC.

The expected charge of the mean muon (4GeV) coming vertically can be calculated as shown in equation 7.2. The result is in the same order of magnitude as the experimental value found.

$$\langle Q \rangle = G_{PMT} h \frac{A_{PMT}}{A_{barrel}} \int_{\lambda_1}^{\lambda_2} \eta(\lambda) \frac{d^2 n}{d\lambda dx} d\lambda \approx 10 pC \quad (7.2)$$

In the equation the term $\frac{d^2 e}{d\lambda dx}$ is given by C.38. This value, as seen in equation

7.2, is divided by the area of the base of the barrel to get the density of Cherenkov photons inside the barrel. Then is multiplied by the area of the PMT to get the photons that arrive at the window device.

The term $\eta(\lambda)$ is the quantum efficiency of the PMT, and is given using equation D.7 and figure 106. G_{PMT} is the gain of the PMT and h is the barrel height.

The expected trigger rate of the mean muon can be also calculated and is shown in equation 7.3.

$$\langle \phi \rangle = \int_0^{2\pi} \int_0^{\pi} \phi(\theta) \sin\theta d\theta d\phi \approx 50Hz \quad (7.3)$$

In the equation $\phi(\theta)$ is the flux of the mean muon that follows \cos^2 as explained in 5.1.

The next step is to determine the power supply voltage and the ideal threshold. For this, let's review a bit of theory. Noise signals ideally have a lower amplitude than muon signals. Thus, theoretically, it should be possible to find a trigger level that separates them.

To find this trigger level, it's possible to plot a graph of the number of events in a fixed time interval about the trigger level or the power supply voltage of the PMT. A simple sketch of the number of events as a function of the trigger level is shown in figure 111.

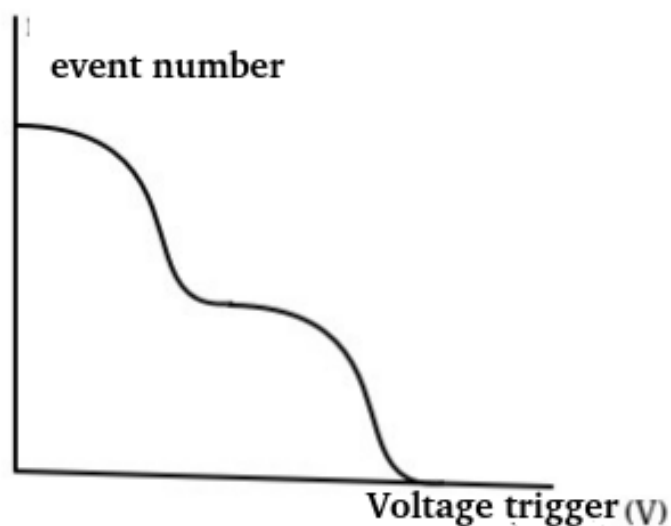


Figure 111 – Theoretically histogram in function of voltage trigger

What it needed to look for is the threshold that causes the plateau. This occurs because ideally the noise charge spectrum is separated from the signal spectrum, as shown in Figure 112. This figure also shows the effect of increasing the power supply voltage (gain increase) and the effect of increasing the threshold level.

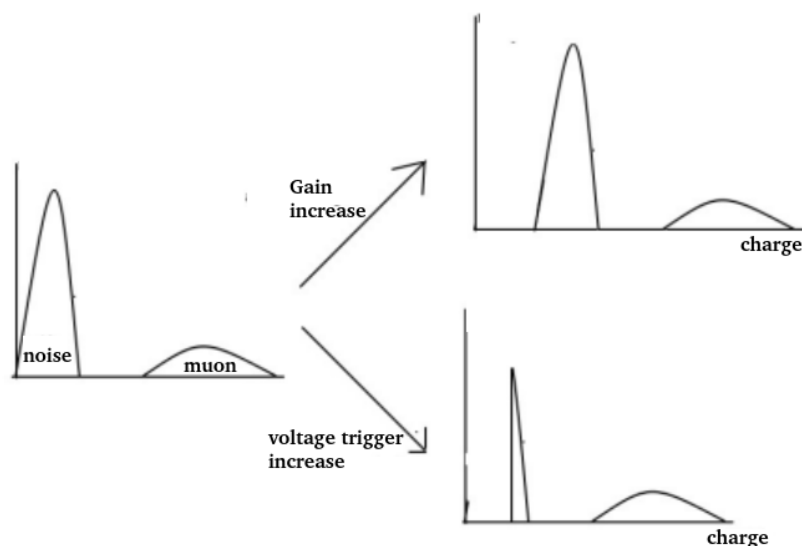


Figure 112 – Histogram of noise and the muons, and the effect of increasing the gain and trigger threshold

The effect of changing the gain is to shift the histogram to the left or right. The effect of changing the threshold is to cut part of the histogram. Figure 111 is nothing more than the integral of figure 112 for each threshold value. When the threshold value is in the middle of the two peaks, the first one is cut and the integral becomes only the area of the second peak. Around this region, the integral remains constant.

That is, in the region where the graph of 111 remains constant, the PMT noise is being filtered. However, in practice, the two spectra are not completely separated, as can be seen in figure 110. In these cases, we should look for the region where the curve is less steep.

The trigger rate found is around 80 Hz, in the same order of magnitude found in 7.3. With all those processes done, the viability of detecting muons in the setup was validated.

7.1.5 SiPM test

One important step was the immersion of the SiPM in water to test its response and durability. First, dry tests were performed using a blue LED coupled to an optic fiber and the dark bottle shown in figure 113. The result of this procedure is shown in Figure 114. The SiPM used is the VE explained 3.3.2.1 and was applied a bias of 57V.

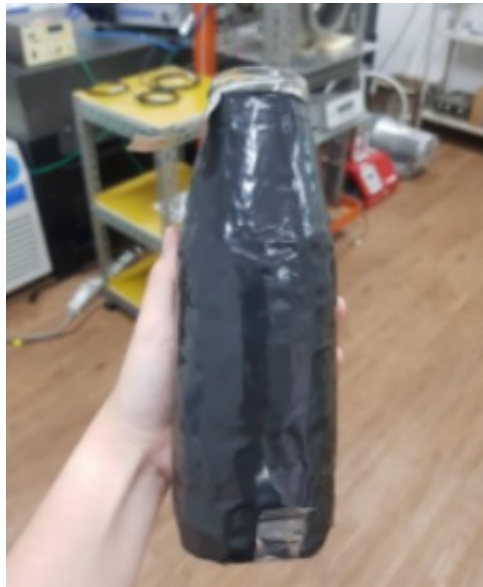


Figure 113 – Dark bottle

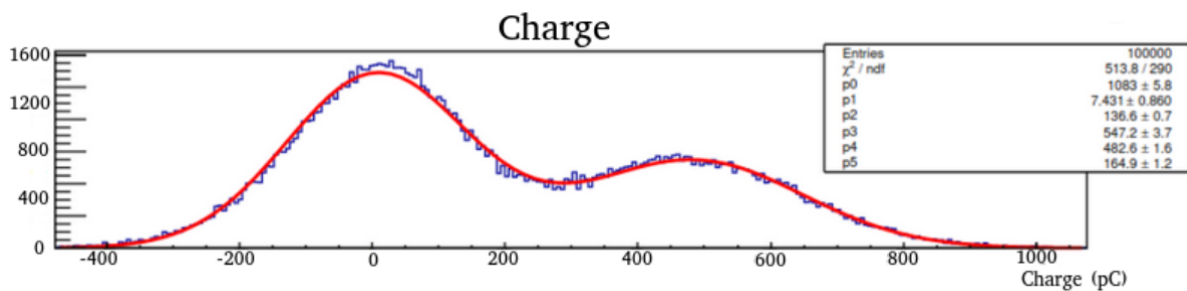


Figure 114 – Charge histogram of the dry SiPM using a blue led. The meaning of each fit parameter is: P0 is the constant that multiplies the normalized noise Gaussian, P1 and P2 are the mean and the standard deviation the same gaussian. Meanwhile, P3 is the constant that multiplies the normalized Gaussian of the LED light signal, and for last P4 and P5 are the mean and the standard deviation of the second gaussian

In this procedure, two triggers were defined. The first one is the signal from

the LED, which was applied a pulse of 82 ns with an amplitude of 3.95 V and a frequency of 4 kHz. The second trigger is a software trigger, also defined with a frequency of 4 kHz.

In the histogram of figure 114 show the charge histogram of the the 100000 waveforms acquired. The charge was calculated signal was plotted in a window of approximately 800 ns. The leftmost peak in corresponds to the noise signal obtained when the internal trigger was fired. The rightmost peak corresponds to the photons captured by the SiPM when the LED fires. It can be observed that the noise charge peak is centered at 7.41 pC (almost zero), while the signal peak is at 482.6 pC. This plot will be used as a reference for the proper functioning of the SiPM in later water immersion stage.

After completing this stage, the next step was to verify the functioning of the SiPMs submerged in water. The dark bottle was filled with deionized water, and the SiPM board was immersed inside it. Also, the SiPM was varnished, except in the collection window.

On the first day, the results were good, and the histograms showed a pattern very similar to the histograms in figure 114. Unfortunately, the electronic board with the SiPM burnt out when it stayed too long in the water, indicating that the board's protection against water was not effective.

A new solution was sought to drop the SiPM board on the water. At first, the solution that was planned was to varnish the SiPMs window with adequate material. But the final solution was to develop an impermeable ARAPUCA to not let the water enter in contact with the SiPM.

7.2 Current Setup

The current setup is an upgrade of the older, using a better barrel and a new design of the C-Arapuca, being water impermeable.

7.2.1 New Barrel

The new barrel is shown in figure 115. The barrel will contain approximately 550 liters of water.



Figure 115 – New barrel of the setup

In the barrel lid, together with the holes of the PMT it was made 3 holes of 13mm in diameter with a flattening of 12.3mm to connect the water proof connector SP1312, for the possibility of using 3 C-Arapuca in the setup. It was made a fourth hole to pass cables for humidity sensors and eventually other sensors needed. By last a central hole was made to pass an optic fiber.

In the lateral interior wall of the barrel was covered by Tyvek as shown in figure 116.

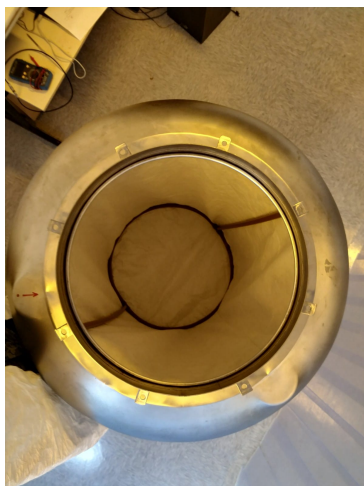


Figure 116 – Tyvek in the new barrel

The squematic of the setup can be seen in figure

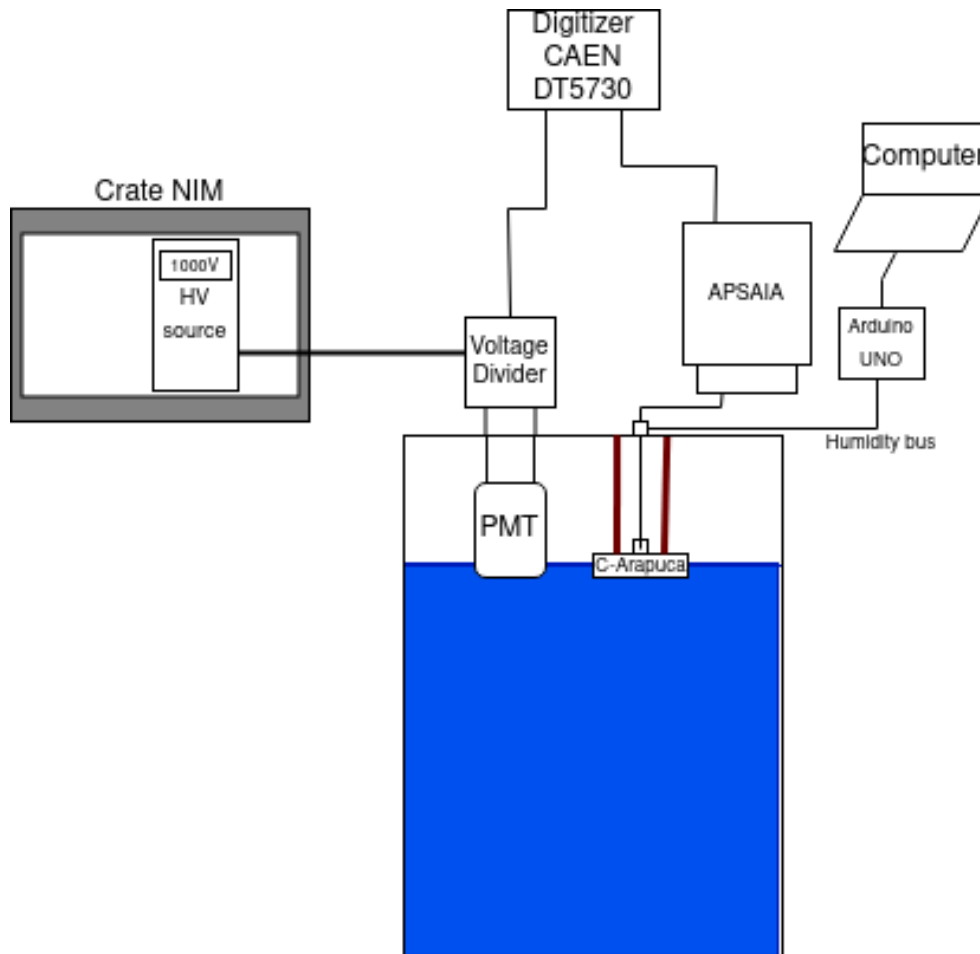


Figure 117 – Schematic of the C-Arapuca setup

7.2.2 The C-Arapuca

The C-Arapuca is an adaptation of the ARAPUCA device to get Cherenkov photons emitted in water. There are two main differences with the X-ARAPUCA device.

The first main difference is that the spectrum of Cherenkov radiation is continuous while the scintillation has well-defined peaks, as shown in figure 118.

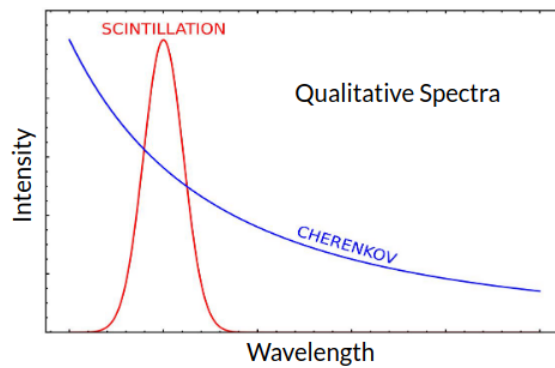


Figure 118 – Scintillation vs Cherenkov spectre [27].

Since the Cherenkov radiation is already in the blue and UV spectrum, there is no need to use the PTP in the dichroic filter. Also, the SiPM is very sensitive to water and can be damaged, as will be explained in section 7. So the C-ARAPUCA must not contain water in its interior. The device also needs the proper cables and connectors to not let water enter the device.

Therefore, the issue of a cryogenic environment is replaced by a water-based environment. Regarding cryogenic environments, given that the C-Arapuca detector is intended to operate at room temperature, the noise in the signal will be more pronounced, whether it be thermal noise or SiPM noise.

The goal of C-Arapuca is a device smaller, more compact, and cheaper than a traditional PMT to detect cosmic and atmospheric particles. Also since the ARAPUCA utilizes a SiPM, there is no need for the high voltage used in PMTs.

The C-Arapuca is a metal box made of aluminum with dimensions of (100x130x30) mm and a window of (70.0 x 93.0) mm. The device is shown in figure 7.



Figure 119 – C-Arapuca design

The wavelength bar is the blue EJ-286 from ELJEN and the dichroic filter used is the one of 400nm cut-off wavelength. The transmittance spectrum is shown in figure 120. In figure, it is possible to note that the filter cut off wavelengths low of 300nm and higher than 440nm.

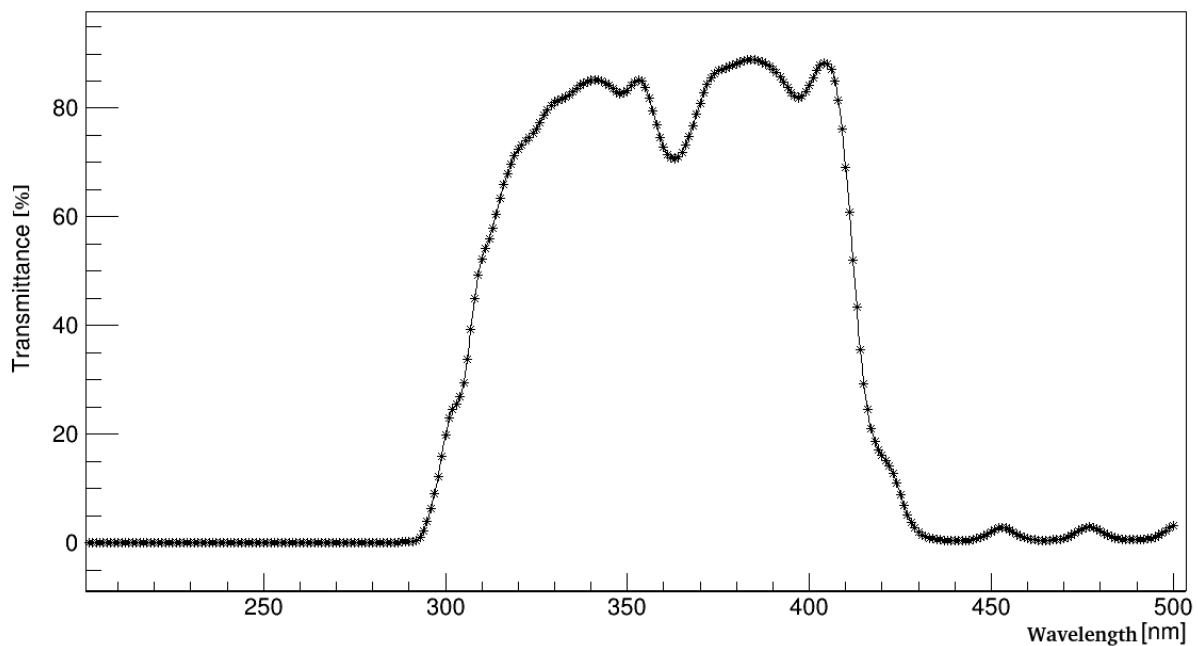


Figure 120 – C-Arapuca dichroic filter transmittance spectrum

The two prototypes of the C-Arapuca build are called Jaci and Guaraci. Those are the names of the goods of the Moon and Sun in the Tupi language, respectively.

The SiPM utilized are from Hamamatsu and inside each C-Arapuca goes two boards containing 4 SiPMs window each. The 2 boards are connected in parallel, so in total 4 wires are needed to the SiPM (anode, cathode and 2 grounds).

The connector utilized is the waterproof SP13 series containing 7 connectors each. The connector can be seen in figure 121.



Figure 121 – Water prof connector of C-Arapuca

Inside the C-Arapuca will also be put the humidity sensor DHT22, which needs 3 wires for operating, totaling the 7 cables in the connector. With an Arduino UNO will be monitored the humidity inside the C-Arapuca to be sure that there is no water penetrating.

7.2.3 WLS and SiPMs

To improve the coupling of the Cherenkov spectrum, as depicted in figure 102, with the C-Arapuca detector, appropriate selection of wavelength shifter (WLS) and SiPM is crucial. The Cherenkov spectrum indicates that the majority of the photons are within the 300 nm to 450 nm range.

Figure 122 presents the absorption and emission spectra of various WLS from ENJEN. The EJ-286 WLS can absorb photons within the 280 nm to 400 nm range, whereas the EJ-282 WLS can absorb photons within the 350 nm to approximately 420 nm range. However, EJ-286 has a better-behaved absorption spectrum.

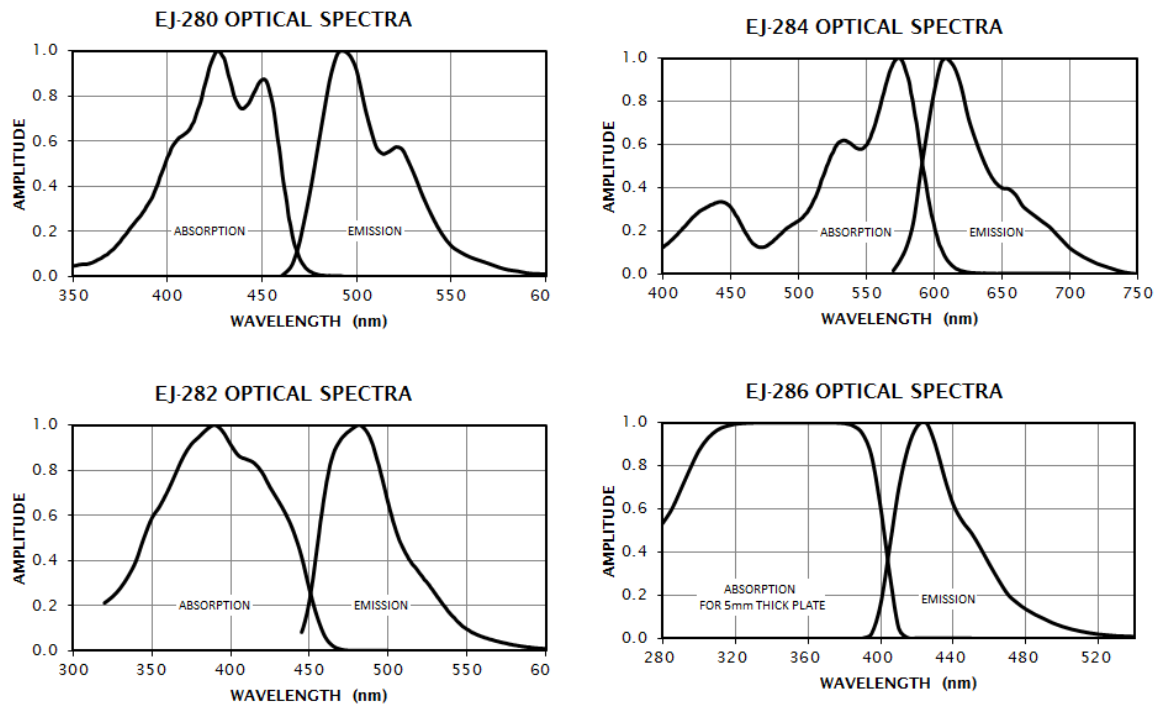


Figure 122 – Different WLS spectrum of absorption and emission [28]

The subsequent step involves coupling the emission spectrum with the SiPM's quantum efficiency spectrum. Figure 123 displays the quantum efficiency of two distinct Hamamatsu SiPMs, revealing their ability to detect photons within the 300 nm to 900 nm range, with a peak around 450 nm.

On the other hand, the two aforementioned WLS, EJ-286 and EJ-282, have an emission spectrum ranging from 400 nm to 520 nm and 450 nm to approximately 600 nm, respectively. Additionally, the peak emission of EJ-286 is closer to the SiPM peak, making it the better choice.

VIKUITI Reflectivity
$R = R_{slab} = 0.95$
Surface area covered by the SiPM in the interior of the slab
$f_{slab} = 0.134831$
Surface area covered by the SiPM in the superior part of the C-Arapuca
$f = 0.0103501$

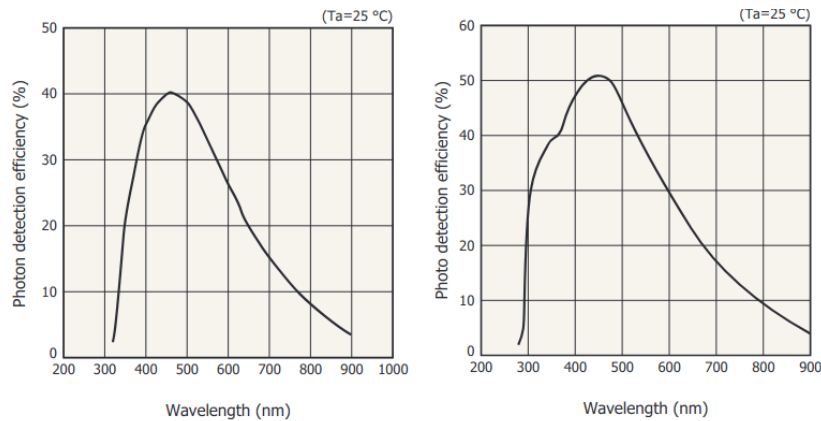


Figure 123 – Photo efficiency of each SiPM. Left: VE Right:HS [29]

7.2.4 Expected efficiency

Using the equations from section 3.3.1 its possible to calculate the percentage of photons that are collected by the second mechanism (gets trapped in the interior of the slab) and the value is shown in equation 7.4.

$$\epsilon_{\theta_c} = \cos(\theta_c) = \cos(\arcsin(\frac{n_{ar}}{n_{guide}})) = \cos(\arcsin(\frac{1.003}{1.58})) = 0.772 \quad (7.4)$$

The efficiency can be calculated using equation 3.17. To use that equation its needed to calculate f, f_{slab}, R and R_{slab} . The values are found in table 7.2.4.

So the geometric efficiency of the device is given by 0.62431, using equation 3.17.

The dichroic filter allows the passage of photon with a wavelength between $\lambda_1 = 270nm$ and $\lambda_2 = 400nm$, so integrating equation C.38 from λ_1 to λ_2 it's possible to calculate the number of photons generated for the mean muon atmospheric (4GeV) for meter traveled in water. The result is 24742.6 γ/m . For this, it was also used the graph given by figure 124, that plot the refraction index of water as a function of the wavelength.

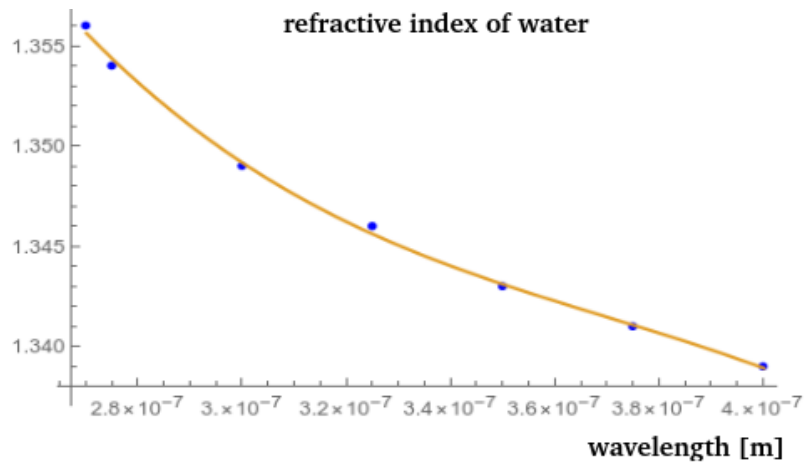


Figure 124 – Refractive index of water as a function of wavelength

To calculate the absorbed photons in the Wavelength bar its fitted a polynomial in the spectrum efficiency of the material is shown in figure 125.

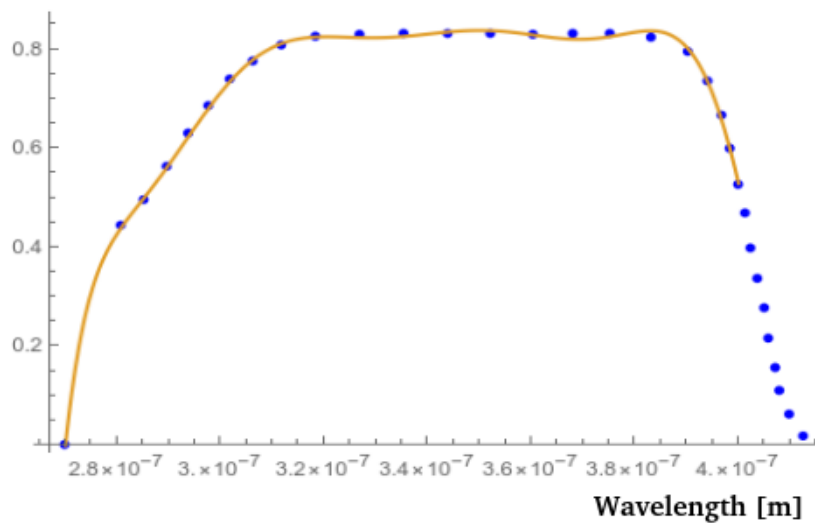


Figure 125 – Absorbance spectrum of the wavelength shifter bar (WLS)

So the number of photons absorbed is given by the integral of the fit of figure 125 times the Cherenkov photon spectrum of equation C.38 from λ_1 to λ_2 . This gives the result of 17337.2 γ/m .

The reemission spectrum of the bar is given by the graph in figure 126.

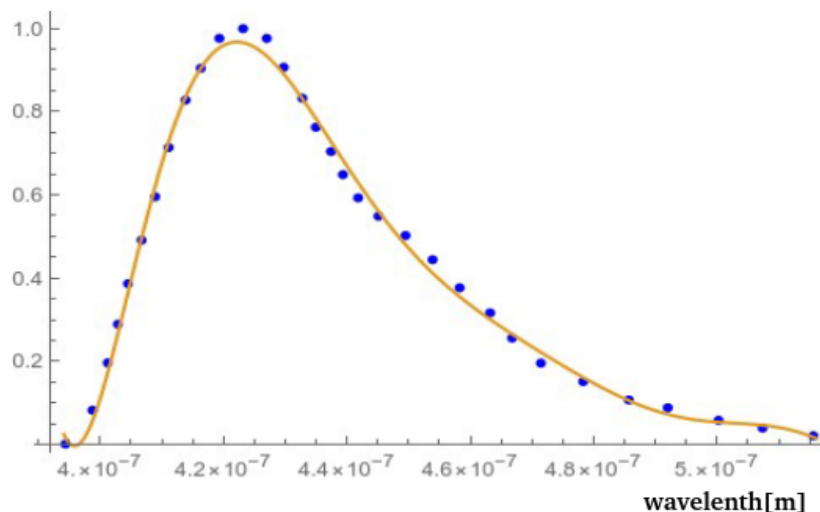


Figure 126 – Reemission spectrum of the wavelength shifter bar (WLS)

This graph is also fitted, divided by the integral of the plot (to normalization), and then multiplied by the geometric efficiency of 0.62431, previously calculated.

Then this graph is multiplied by 17337.2 (the number of photons absorbed) and by 0.9 (The transmittance of the dichroic filter).

The final step is then to integrate this graph times the quantum efficiency of the SiPM. This gives the total of 4215.21 photo-electrons detected for meter.

So the total efficiency is given by equation 7.5.

$$\text{efficiency} = \frac{N_{pe}}{N_{\gamma}} = \frac{4215.21}{24742.6} = 0.17 \quad (7.5)$$

It's possible also to calculate the efficiency of the PMT. The number of photons emitted by meter that a muon emits in the wavelength window that a PMT can detect (from 300nm to 650nm) is 35037.7 γ /m, using equation C.38.

Integrating the C.38 times the quantum efficiency of the PMT it obtained the value of 4828.74 γ /m.

So the total efficiency of the PMT is given by equation 7.6.

$$\text{efficiency} = \frac{N_{pe}}{N_{\gamma}} = \frac{4828.24}{35037.7} = 0.137 \quad (7.6)$$

So the expected efficiency of the C-Arapuca is 17%, bigger than the expected efficiency of the PMT which is 14%.

7.2.5 First Test of C-Arapuca device

It was put the first assembled C-Arapuca (JACI) inside the new barrel, with no water in the interior and applying a signal of 1.7V and duration of 50ns in an ultraviolet LED, it was obtained the histograms shown in figure 127. In this test, the applied PMT voltage was 2kV and the voltage at the SiPM was 56V.

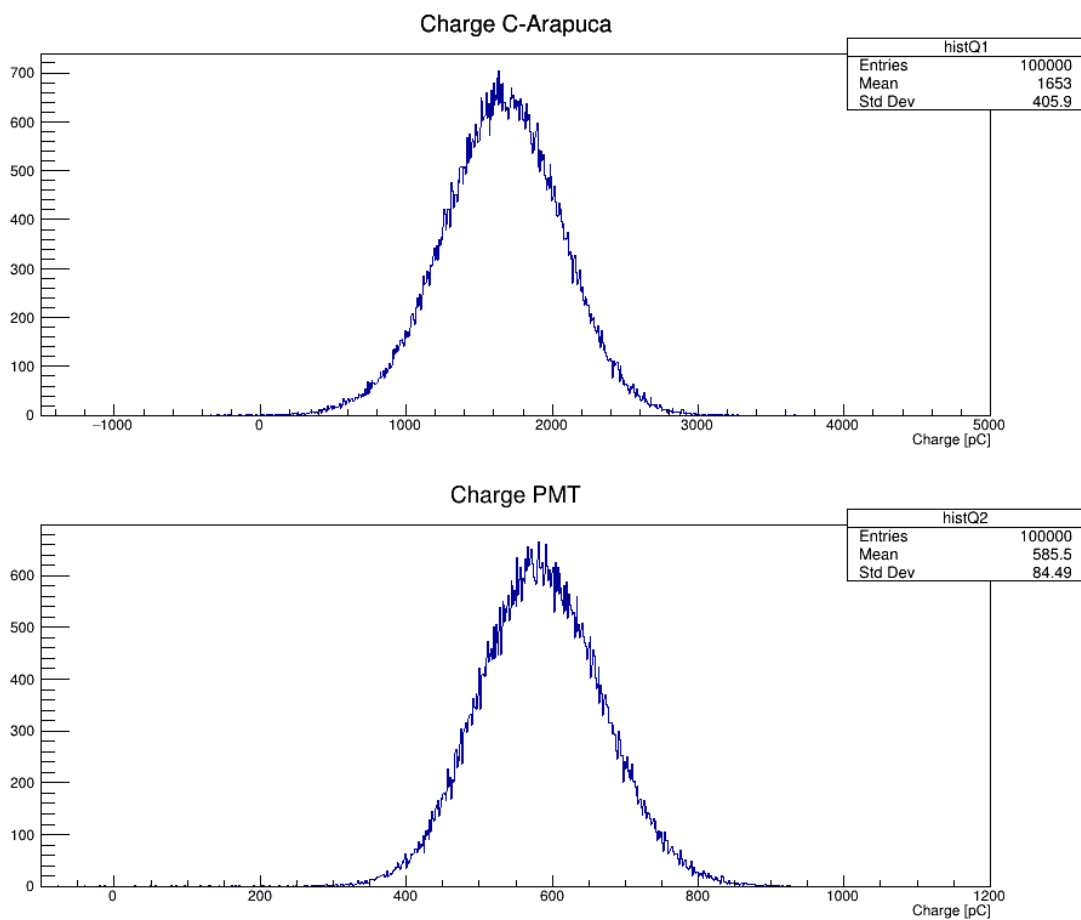


Figure 127 – Charge histogram of the PMT and the C-Arapuca inside the new tonel. The mean charge obtained for the PMT was 585 pC, and for the C-Arapuca was 1653pC

In the figure it's observed that the mean charge obtained for the PMT was 585pC, and for the C-Arapuca was 1653pC. Clearly, the C-Arapuca device was able to see the UV photon, so it's possible to confirm that the device works. The charge ratio between

the mean charge of C-Arapuca over the mean charge of the PMT, in this configuration, is approximately 3.

8 Conclusion

In this thesis it was tested the efficiency of the X-ARAPUCA for visible light, which is aimed to be used in SBND for the study of neutrinos oscillation at short baseline. The device shows an efficiency of 3.2%. More experiments are in the way to test more the device.

In this work it was also made an overview of the electronics used in SBND to acquire the data of the ARAPUCAs and also the work done to make the system be ready to use. More work is planned in the area to further developed the acquisition system.

For APSAIA for example is needed to understand better the noise source and the spectral power noise of the system. Also its needed to adequate the amplifiers in the flange without making them suffer mechanical stress and make sure none of them touch each other.

For DAPHNE its needed to make sure that the system is capable of reading the high rate of data without the system crashing. Its needed, also, to understanding better the data format flux, and see how it changes with the number of FrontEnd Boards (FEB) connected and with the number of ARAPUCAs connected. Also the FPGA codes need to be further understand and REGISTER MAP is the process of being developed.

It was also developed an light monitoring system for the ARAPUCAs to detect the light entering in the interior of the detector in SBND. No light was detected during the move of the detector, and this system can still be used to validate the status of the SiPM's X-ARAPUCAs.

In this dissertation, its was also proposed a novel technology based on the working principle of the ARAPUCA, but instead using scintillation light, the goal is to use Cherenkov radiation.

The area of cosmic rays and climate study will be greatly benefited with the creation of the C-Arapuca, since is more cheaper and more easier to use than an PMT.

Preliminary test shows that is viable to detect the muon peak in an water cherenkov tonel in small-scale, with the water level, water volume presented, water purity and tyvek presented in section 7 . Also theoretical math showed that the C-ARAPUCA is more efficient than an PMT in same conditions. For last it was shown that the C-Arapuca really works.

The next steps are to acquire data from the newer assembled C-ARAPUCAs

and tonel, and then validate definitively the device.

Bibliography

- 1 AGUILAR-AREVALO, A. et al. Updated MiniBooNE neutrino oscillation results with increased data and new background studies. *Physical Review D*, American Physical Society (APS), v. 103, n. 5, mar 2021. Cited 2 times on pages 11 and 31.
- 2 THOMSON, M. *Modern Particle Physics*. 1. ed. [S.l.]: Cambridge University Press, 2013. Cited 6 times on pages 11, 15, 24, 32, 33, and 161.
- 3 FERMILAB. *Fermilab*. <https://vms.fnal.gov/asset/detail?recid=1962973>. Accessed on 02/09/2023. Cited 2 times on pages 11 and 35.
- 4 MACHADO, P. A.; PALAMARA, O.; SCHMITZ, D. W. The short-baseline neutrino program at fermilab. *Annual Review of Nuclear and Particle Science*, Annual Reviews, v. 69, n. 1, p. 363–387, oct 2019. Cited 3 times on pages 11, 36, and 39.
- 5 ACCIARRI, R. et al. A proposal for a three detector short-baseline neutrino oscillation program in the fermilab booster neutrino beam. 03 2015. Cited 3 times on pages 11, 22, and 37.
- 6 MAJUMDAR, K.; MAVROKORIDIS, K. Review of liquid argon detector technologies in the neutrino sector. *Applied Sciences*, v. 11, p. 2455, 03 2021. Cited 2 times on pages 11 and 38.
- 7 A Method to Extract the Charge Distribution Arriving at the TPC Wire Planes in MicroBooNE. 7 2016. Cited 2 times on pages 11 and 39.
- 8 LEO, W. R. *Techniques for Nuclear and Particle Physics Experiments A How-to Approach*. 2. ed. [S.l.]: Springer-Verlag Berlin Heidelberg GmbH, 1994. Cited 7 times on pages 11, 15, 40, 118, 170, 171, and 174.
- 9 ARAUJO, G. R. Wavelength shifting and photon detection of scintillation light from liquid argon. 2019. Cited 3 times on pages 11, 41, and 52.
- 10 SEGRETO, E. Analysis and simulation of events with scintillation light emission from the icarus t600 lar detector. 2006. Cited 3 times on pages 11, 42, and 44.
- 11 MACHADO, A.; SEGRETO, E. Arapuca a new device for liquid argon scintillation light detection. *Journal of Instrumentation*, v. 11, n. 02, p. C02004, feb 2016. Cited 4 times on pages 11, 48, 49, and 51.
- 12 SOUZA, H. V. de. Arapuca, light trapping device for the dune experiment. 2021. Cited 3 times on pages 11, 50, and 92.
- 13 WIKIPEDIA. *Terphenyl*. <https://en.wikipedia.org/wiki/Terphenyl>. Accessed on 03/02/2023. Cited 2 times on pages 11 and 50.
- 14 WIKIPEDIA. *Tetraphenyl butadiene*. https://en.wikipedia.org/wiki/Tetraphenyl_butadiene. Accessed on 03/02/2023. Cited 2 times on pages 11 and 50.

- 15 OMLC. *p-Terphenyl*. <https://omlc.org/spectra/PhotochemCAD/html/003.html>. Accessed on 01/30/2023. Cited 2 times on pages 11 and 51.
- 16 KOCZON, P.; BRAEM, A.; JORAM, C.; SOLEVI, P.; DURR, M.; HOHNE, C. *Wavelength-shifting materials for the use in RICH detectors - p-terphenyl and tetraphenyl-butadiene revisited*. Geneva, 2010. Cited 2 times on pages 11 and 51.
- 17 CARLOSENA, L. et al. Experimental development and testing of low-cost scalable radiative cooling materials for building applications. *Solar Energy Materials and Solar Cells*, v. 230, p. 111209, 06 2021. Cited 2 times on pages 11 and 53.
- 18 FALCONE, A. et al. Cryogenic sipm arrays for the dune photon detection system. 2020. Cited 2 times on pages 11 and 54.
- 19 MACHADO, A.; SEGRETO, E.; WARNER, D.; FAUTH, A.; GELLI, B.; MÁXIMO, R.; PISSOLATTI, A.; PAULUCCI, L.; MARINHO, F. The x-ARAPUCA: an improvement of the ARAPUCA device. *Journal of Instrumentation*, IOP Publishing, v. 13, n. 04, p. C04026–C04026, apr 2018. Cited 4 times on pages 11, 22, 55, and 56.
- 20 WORKMAN, R. L.; OTHERS. Review of Particle Physics. *PTEP*, v. 2022, p. 083C01, 2022. Cited 8 times on pages 13, 16, 24, 25, 27, 114, 119, and 160.
- 21 AGUIAR, R. de. Study of cosmic ray signals in a water cherenkov detector. 2021. Cited 6 times on pages 13, 15, 116, 121, 162, and 168.
- 22 SHUKLA, P.; SANKRITH, S. *Energy and angular distributions of atmospheric muons at the Earth*. [S.l.]: arXiv, 2016. <https://arxiv.org/abs/1606.06907>. Cited 2 times on pages 13 and 117.
- 23 GROOM, D. E.; MOKHOV, N. V.; STRIGANOV, S. I. Muon stopping power and range tables 10 mev–100 tev. *Atomic Data and Nuclear Data Tables*, v. 78, n. 2, p. 183–356, 2001. ISSN 0092-640X. Cited 2 times on pages 13 and 118.
- 24 SPURIO, M. *Particles and Astrophysics. A Multi-Messenger Approach*. [S.l.]: Springer, 2015. Cited 2 times on pages 13 and 120.
- 25 WAGNER, R.; BYRUM, K.; SANCHEZ, M.; VANIACHINE, A.; SIEGMUND, O.; OTTE, N.; RAMBERG, E.; HALL, J.; BUCKLEY, J. The next generation of photo-detectors for particle astrophysics. 05 2009. Cited 2 times on pages 14 and 124.
- 26 14-STAGE photomultiplier tube. [S.l.], 1976. Cited 4 times on pages 14, 15, 128, and 172.
- 27 LAND, B. et al. *Spectral Photon Sorting with the Dichroicon in Large Neutrino Detectors*. https://indico.fnal.gov/event/46746/contributions/210179/attachments/141204/177738/Spectral_Photon_Sorting_with_the_Dichroicon_in_Large_Neutrino_Detectors.pdf. Accessed on 03/05/2023. Cited 2 times on pages 14 and 140.
- 28 ENJEN. *ENJEN*. <https://eljentechnology.com/>. Accessed on 03/02/2023. Cited 3 times on pages 14, 68, and 143.

- 29 HAMAMATSU. *Hamamatsu*. <https://www.hamamatsu.com/us/en.html>. Accessed on 02/27/2023. Cited 3 times on pages 14, 58, and 144.
- 30 PHOTONIS. *Photomultiplier tube basics*. [S.l.], 2002. Cited 2 times on pages 15 and 173.
- 31 NEAMEN, D. A. *Semiconductor Physics and Devices*. 4. ed. [S.l.]: McGrawHill, 2012. Cited 2 times on pages 15 and 176.
- 32 FIRSTSENSOR. *Introduction to silicon photomultipliers (SiPMs)*. 2023. https://www.first-sensor.com/cms/upload/appnotes/AN_SiPM_Introduction_E.pdf. Accessed on 02/06/2023. Cited 4 times on pages 15, 86, 177, and 178.
- 33 HAMMAMATSU. *A technical guide to silicon photomultipliers (MPPC) - Section 1*. 2023. <https://hub.hamamatsu.com/us/en/technical-notes/mppc-sipms/a-technical-guide-to-silicon-photomultipliers-MPPC-Section-1.html>. Cited 7 times on pages 15, 178, 179, 180, 184, 185, and 189.
- 34 ONSEMI. *Biasing and Readout of ON Semiconductor SiPM Sensors*. <https://www.onsemi.com/pub/Collateral/AND9782-D.PDF>. Accessed on 02/06/2023. Cited 2 times on pages 15 and 180.
- 35 CORSI, F.; FORESTA, M.; MARZOCCA, C.; MATARRESE, G.; GUERRA, A. D. Asic development for sipm readout. *Journal of Instrumentation*, v. 4, p. P03004, 03 2009. Cited 3 times on pages 15, 185, and 186.
- 36 HAMMAMATSU. *What is an SiPM and how does it work?* <https://hub.hamamatsu.com/us/en/technical-notes/mppc-sipms/what-is-an-SiPM-and-how-does-it-work.html>. Accessed on 02/06/2023. Cited 2 times on pages 15 and 188.
- 37 BRAINKART. *sp² Hybridization*. https://www.brainkart.com/article/sp2-Hybridization_29817/. Accessed on 01/23/2023. Cited 2 times on pages 15 and 190.
- 38 CORTES, S. *Hybridization of Carbon*. 2020. https://chem.libretexts.org/Bookshelves/Organic_Chemistry. Accessed on 02/24/2023. Cited 2 times on pages 15 and 190.
- 39 CHEMISTRY, A.-L. *Delocalisation*. <https://avevelchemistry.co.uk/definition/delocalisation/>. Accessed on 01/24/23. Cited 2 times on pages 15 and 191.
- 40 GASPAR, C. S. CaracterizaÇÃo fotofísica de derivados de fenantrolina fluorescentes. 2017. Cited 2 times on pages 15 and 191.
- 41 K., H. *Singlet vs. Triplet State*. <https://psiberg.com/singlet-vs-triplet-state/>. Accessed on 01/24/2013. Cited 2 times on pages 15 and 192.
- 42 BOTOGOSKE, G.; PIASSON, A. C. Sistema de controle dos parâmetros relevantes de um criostato contendo argônio líquido (lar). trabalho de conclusão de curso (graduação em engenharia eletrônica). 2021. Cited 3 times on pages 16, 46, and 84.

- 43 ABI, B. et al. First results on ProtoDUNE-SP liquid argon time projection chamber performance from a beam test at the CERN neutrino platform. *Journal of Instrumentation*, IOP Publishing, v. 15, n. 12, p. P12004–P12004, dec 2020. Disponível em: <https://doi.org/10.1088%2F1748-0221%2F15%2F12%2Fp12004>. Cited on page 22.
- 44 ABI, B. et al. Volume i. introduction to dune. *Journal of Instrumentation*, v. 15, n. 08, p. T08008, aug 2020. Disponível em: <https://dx.doi.org/10.1088/1748-0221/15/08/T08008>. Cited on page 22.
- 45 CLEVELAND, B. T.; DAILY, T.; DAVIS, J. R.; DISTEL, J. R.; LANDE, K.; LEE, C. K.; WILDENHAIN, P. S.; ULLMAN, J. Measurement of the solar electron neutrino flux with the homestake chlorine detector. *The Astrophysical Journal*, v. 496, n. 1, p. 505, mar 1998. Cited on page 29.
- 46 PONTECORVO, B. Neutrino Experiments and the Problem of Conservation of Leptonic Charge. *Zh. Eksp. Teor. Fiz.*, v. 53, p. 1717–1725, 1967. Cited on page 29.
- 47 AHMAD, Q. R. et al. Direct evidence for neutrino flavor transformation from neutral-current interactions in the sudbury neutrino observatory. *Phys. Rev. Lett.*, American Physical Society, v. 89, p. 011301, Jun 2002. Cited on page 29.
- 48 AGUILAR, A. et al. Evidence for neutrino oscillations from the observation of anti neutrinos electronic appearance in a anti neutrinos muonic beam. *Physical Review D*, American Physical Society (APS), v. 64, n. 11, nov 2001. Cited on page 30.
- 49 STENICO, G. V. Neutrino phenomenology in short-baseline experimentst. 2021. Cited on page 32.
- 50 BARREIROS, D. M. A minimal seesaw model for neutrino masses and the origin of matter. 2017. Cited on page 34.
- 51 DUNE. *DUNE*. <https://www.dunescience.org/>. Accessed on 03/03/2023. Cited on page 35.
- 52 SEGRETO, E.; MACHADO, A.; PAULUCCI, L.; MARINHO, F.; GALANTE, D.; GUEDES, S.; FAUTH, A.; TEIXEIRA, V.; GELLI, B.; GUZZO, M.; ARAUJO, W.; AMBRÓ SIO, C.; BISSIANO, M.; FILHO, A. L. Liquid argon test of the ARAPUCA device. *Journal of Instrumentation*, IOP Publishing, v. 13, n. 08, p. P08021–P08021, aug 2018. Cited on page 54.
- 53 SEGRETO, E.; MACHADO, A.; FAUTH, A.; RAMOS, R.; SOUZA, G. de; SOUZA, H.; PIMENTEL, V.; BAZETTO, M. Q.; AYALA-TORRES, M. First liquid argon test of the x-arapuca. *Journal of Instrumentation*, v. 15, n. 05, p. C05045, may 2020. Cited on page 57.
- 54 POWER, G. to. *Glass to Power*. <https://www.glasstopower.com/?lang=en>. Accessed on 02/27/2023. Cited on page 58.
- 55 ONSEMI. *ONSEMI*. <https://www.onsemi.com/>. Accessed on 03/02/2023. Cited on page 68.

- 56 REISSMAN. *Temperature measurement with Platinum resistive sensors*. 2023. <https://m.reissmann.com>. Cited on page 84.
- 57 CAEN. *WaveDump*. 2023. <https://www.caen.it/products/caen-wavedump>. Cited on page 89.
- 58 CERN. *ROOT*. 2023. <https://root.cern/>. Accessed on 02/21/2023. Cited on page 91.
- 59 CONDAT, L. A direct algorithm for 1-d total variation denoising. *IEEE Signal Processing Letters*, v. 20, n. 11, p. 1054–1057, 2013. Cited on page 92.
- 60 GALBIATI, C.; LI, X.; LUO, J.; MARLOW, D. R.; WANG, H.; WANG, Y. Pulse shape study of the fast scintillation light emitted from xenon-doped liquid argon using silicon photomultipliers. *Journal of Instrumentation*, IOP Publishing, v. 16, n. 02, p. P02015, 2021. Cited on page 103.
- 61 SEGRETO, E. Evidence of delayed light emission of tetraphenyl butadiene excited by liquid argon scintillation light. *Physical Review C*, v. 91, 11 2014. Cited on page 103.
- 62 DEVOL, T.; WEHE, D.; KNOLL, G. Evaluation of p-terphenyl and 2,2 dimethyl-p-terphenyl as wavelength shifters for barium fluoride. *Nuclear Instruments and Methods in Physics Research Section A: Accelerators, Spectrometers, Detectors and Associated Equipment*, v. 327, n. 2, p. 354–362, 1993. ISSN 0168-9002. Cited on page 103.
- 63 VINOGRADOV, S.; VINOGRADOVA, T.; SHUBIN, V.; SHUSHAKOV, D.; SITARSKY, K. Probability distribution and noise factor of solid state photomultiplier signals with cross-talk and afterpulsing. In: *2009 IEEE Nuclear Science Symposium Conference Record (NSS/MIC)*. [S.l.: s.n.], 2009. p. 1496–1500. Cited on page 108.
- 64 SHUKLA, P.; SANKRITH, S. *Energy and angular distributions of atmospheric muons at the Earth*. [S.l.]: arXiv, 2016. <https://arxiv.org/abs/1606.06907>. Cited on page 120.
- 65 KAMLAND'S precision neutrino oscillation measurements. *Nuclear Physics B*, v. 908, p. 52–61, 2016. ISSN 0550-3213. Neutrino Oscillations: Celebrating the Nobel Prize in Physics 2015. Cited on page 160.
- 66 EVANS, J. *The MINOS experiment: results and prospects*. [S.l.]: arXiv, 2013. <https://arxiv.org/abs/1307.0721>. Cited on page 160.
- 67 WOLFRAM. *Modified Bessel Function of the Second Kind*. <https://mathworld.wolfram.com/ModifiedBesselFunctionoftheSecondKind.html>. Accessed on 17/06/2023. Cited on page 166.
- 68 OVERSTRAETEN R. ; DE MAN, H. V. Measurement of the ionization rates in diffused silicon p- n junctions. 1970. Cited on page 179.
- 69 GRIFFITHS, D. J. *Mecânica Quântica*. 2. ed. [S.l.]: Pearson, 2011. Cited on page 192.

Appendix

APPENDIX A – Model of neutrino oscillation

The neutrino in the vacuum, for being a free particle, each mass state is described by a plane wave propagating through time and space, as shown in [A.1](#), with $\hbar = 1$.

$$|\nu_i(\vec{x}, t)\rangle = e^{i(\vec{p}_i \cdot \vec{x} - E_i t)} |\nu_i\rangle \quad (\text{A.1})$$

In which the relation between mass and energy can be described as shown in equation [A.2](#), in units such that $c = 1$.

$$E_i = \sqrt{m_i^2 + p_i^2} \approx |p_i| + \frac{m_i^2}{2|p_i|} \quad (\text{A.2})$$

The approximation of the equation [A.2](#) is because its mass is much smaller than its energy.

An electron neutrino when created can be described by the equation [A.3](#):

$$|\Psi(x = 0, t = 0)\rangle = |\nu_e\rangle = \sum_{i=1}^3 U_{ei} |\nu_i\rangle \quad (\text{A.3})$$

When we make the state [A.3](#) evolve in space and time we have [A.4](#) and replacing [A.1](#) we got:

$$|\Psi(x, t)\rangle = \sum_{i=1}^3 U_{ei} e^{i(p_i x - E_i t)} |\nu_i\rangle = \sum_{i=1}^3 U_{ei} e^{i(p_i x - (|p_i| + \frac{m_i^2}{2|p_i|})t)} |\nu_i\rangle \quad (\text{A.4})$$

Assuming that the package has medium energy of E and the neutrino's mass is way too small, we can make $E \approx p_i$ and the equation [A.4](#) becomes [A.5](#).

$$|\Psi(x, t)\rangle = e^{iE(x-t)} \sum_{i=1}^3 U_{ei} e^{-i\frac{m_i^2}{2E}t} |\nu_i\rangle \quad (\text{A.5})$$

The state of this neutrino to a distance L of its creation, and assuming that its velocity is very close to the velocity of the light, becomes [A.6](#).

$$|\Psi(L, L)\rangle = \sum_{i=1}^3 U_{ei} e^{-i\frac{m_i^2}{2E}L} |\nu_i\rangle \quad (\text{A.6})$$

The probability of this neutrino changing its flavor is given by [A.7](#), with k being able to assume the indexes μ and τ .

$$|\langle \nu_k | \Psi(L, L) \rangle|^2 = \left| \sum_{i=1}^3 \sum_{j=1}^3 U_{kj}^* U_{ei} e^{-i\frac{m_i^2}{2E}L} \langle \nu_j | \nu_i \rangle \right|^2 = \left| \sum_{j=1}^3 U_{kj}^* U_{ej} e^{-i\frac{m_j^2}{2E}L} \right|^2 \quad (\text{A.7})$$

The equation [A.7](#) can be opened as [A.8](#).

$$P(\nu_e \longrightarrow \nu_k)(L) = |\langle \nu_k | \Psi(L, L) \rangle|^2 = \sum_{j=1}^3 |U_{kj}^* U_{ej}|^2 + 2\text{Re} \left(\sum_{j>i}^{3,3} U_{kj}^* U_{ej} U_{ki}^* U_{ei} e^{-i\frac{m_j^2 - m_i^2}{2E}L} \right) \quad (\text{A.8})$$

To continue, we need to remember that the PMNS matrix is a unity matrix and we can write it like in [A.9](#).

$$UU^\dagger = I \quad (\text{A.9})$$

Opening the terms of the matrix equation [A.9](#) we got [A.10](#).

$$\sum_{i=0}^3 U_{ki} U_{ni}^* = \delta_{kn} \quad (\text{A.10})$$

Multiplying the equation [A.10](#) by its complex conjugate we got [A.11](#).

$$\sum_{i=0}^3 |U_{ki} U_{ni}^*|^2 + 2\text{Re} \left(\sum_{j>i}^{3,3} U_{kj} U_{nj}^* U_{ki} U_{ni}^* \right) = \delta_{kn} \quad (\text{A.11})$$

Replacing the first term of the equation [A.11](#) by [A.8](#) and also replacing the index n by e (electron) we got the equation [A.12](#)

$$P(\nu_e \longrightarrow \nu_k)(L) = \delta_{ek} + 2\text{Re} \left(\sum_{j>i}^{3,3} U_{kj}^* U_{ej} U_{ki}^* U_{ei} (e^{-i\frac{m_j^2 - m_i^2}{2E}L} - 1) \right) \quad (\text{A.12})$$

Opening the exponential of the equation [A.12](#) we got [A.13](#)

$$P(\nu_e \longrightarrow \nu_k)(L) = \delta_{ek} + 2\text{Re} \left(\sum_{j>i}^{3,3} U_{kj}^* U_{ej} U_{ki}^* U_{ei} \left(\cos\left(\frac{m_j^2 - m_i^2}{2E}L\right) - 1 \right) \right) - 2\text{Re} \left(\sum_{j>i}^{3,3} U_{kj}^* U_{ej} U_{ki}^* U_{ei} \left(i \sin\left(\frac{m_j^2 - m_i^2}{2E}L\right) \right) \right) \quad (\text{A.13})$$

In the equation A.13 the cosine of the first summation can be replaced by $\cos x - 1 = -2\sin^2(x/2)$. Since the second summation presents the imaginary number i multiplied by it, we can replace $Re(ix)$ for $-Im(x)$. This way we obtain the final equation for oscillation in the equation A.14

$$\begin{aligned}
 P(\nu_e \longrightarrow \nu_k)(L) = & \delta_{ek} - 4Re\left(\sum_{j>i}^{3,3} U_{kj}^* U_{ej} U_{ki}^* U_{ei} \sin^2\left(\frac{m_j^2 - m_i^2}{4E} L\right)\right) \\
 & + 2Im\left(\sum_{j>i}^{3,3} U_{kj}^* U_{ej} U_{ki}^* U_{ei} \sin\left(\frac{m_j^2 - m_i^2}{2E} L\right)\right)
 \end{aligned}
 \tag{A.14}$$

APPENDIX B – Measured values of PMNS matrix

The PMNS matrix can be described with three mixing angles and one complex phase, as described in equation B.1

$$\begin{pmatrix} U_{e1} & U_{e2} & U_{e3} \\ U_{\mu1} & U_{\mu2} & U_{\mu3} \\ U_{\tau1} & U_{\tau2} & U_{\tau3} \end{pmatrix} = \begin{pmatrix} 1 & 0 & 0 \\ 0 & \cos\theta_{23} & \sin\theta_{23} \\ 0 & -\sin\theta_{23} & \cos\theta_{23} \end{pmatrix} \begin{pmatrix} \cos\theta_{13} & 0 & \sin\theta_{13}e^{-i\delta} \\ 0 & 1 & 0 \\ -\sin\theta_{13}e^{i\delta} & 0 & \sin\theta_{13} \end{pmatrix} \begin{pmatrix} \cos\theta_{12} & \sin\theta_{12} & 0 \\ -\sin\theta_{12} & \cos\theta_{12} & 0 \\ 0 & 0 & 1 \end{pmatrix} \quad (\text{B.1})$$

From recent experiments - like SNO, KamLAND, Super-kamiokande, Minos, Data Bay, RENO and the Double-CHooz - is possible to know the values of the mixing angles. The values are shown in table 10.

Mixing angle	Value
$\sin^2(\theta_{12})$	$0,307 \pm 0,013$
$\sin^2(\theta_{23})$	$0,546 \pm 0,021$ $0,539 \pm 0,022$
$\sin^2(\theta_{13})$	$(2,20 \pm 0,07)10^{-2}$

Table 10 – Values of the mixing angles [20]

The value of the δ phase is not known yet and it is responsible for the CP violation in the leptonic sector.

Another fundamental number in the oscillation studies is the mass values for each state of mass. The mass value is not known yet, however, it is known that the value is small - as shown in table 2.

Once the oscillation depends on the difference of the square of the masses, it is very important to determine this number. The KamLAND experiment determined a value of $m_2^2 - m_1^2 = (7,53 \pm 0,18)10^{-5}eV^2$ [65].

The Minus experiment, however, determined the module of the difference of the square of the mass state 2 and the mass state 3 ($|m_3^2 - m_2^2|$) [66]. The value known in literature is $(2,453 \pm 0,033)10^{-3}eV^2$ to the normal order of masses.

Based on this, it is possible to have two masses hierarchy: the normal order, in which the mass state 3 is bigger than the others two states; or the reversed order, in

which the mass state 3 is smaller than the other two states. Figure 128 exemplifies the possible orders.

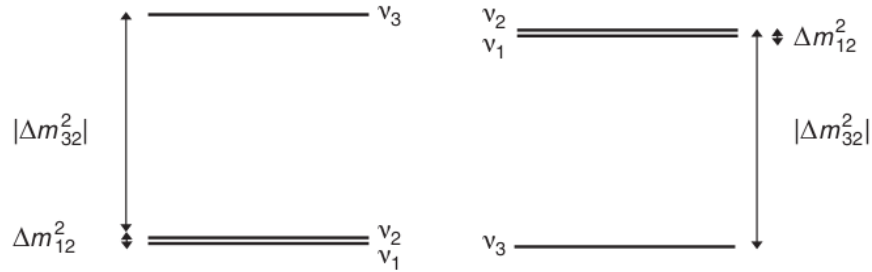


Figure 128 – Possible order of the masses [2]

APPENDIX C – Cherenkov Radiation Derivation

C.1 The problem

A charged particle with a velocity \vec{v} in the z -direction (without loss of generality) in a medium with electric permittivity (ϵ) and magnetic permeability (μ), can have his electric density and current density represented by equation C.1.

$$\begin{aligned} p(\vec{x}, t) &= q\delta(z - vt)\delta(x)\delta(y) \\ \vec{J}(\vec{x}, t) &= vp(\vec{x}, t)\hat{z} \end{aligned} \quad (\text{C.1})$$

This particle travels in the medium as seen in figure 129. The energy lost by the particle by length traveled can be calculated as the energy radiated per distance traveled to outside the infinite cone seen in figure 129 with radius b . This is calculated in equation C.3 with help of the equation C.2.

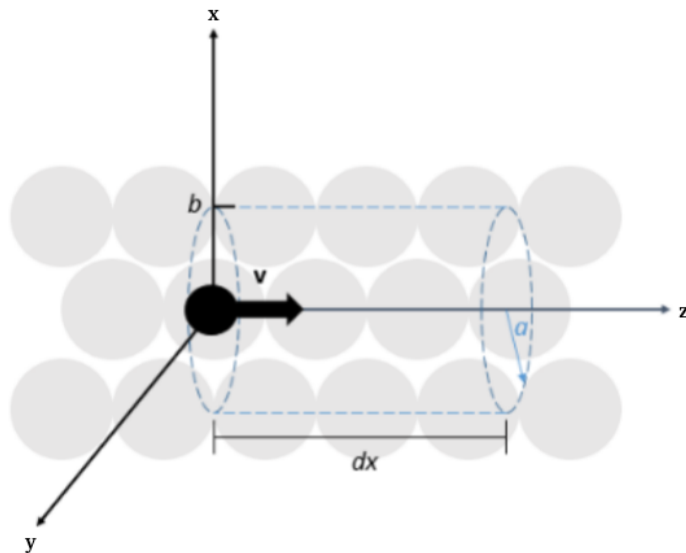


Figure 129 – Particle traveling in a medium with speed in z direction [21]

$$\frac{de}{dt} = \oint \vec{S} \cdot d\vec{A} \quad (\text{C.2})$$

$$\frac{de}{dz} = \frac{de}{vdt} = \frac{1}{v\mu} \oint \vec{S} \cdot d\vec{A} = \frac{1}{v\mu} \iint (\vec{E} \times \vec{B}) \cdot d\vec{A} = \frac{1}{v\mu} \int_0^{2\pi} \int_{-\text{inf}}^{+\text{inf}} (\vec{E} \times \vec{B}) \cdot \hat{n} \cdot b \cdot d\theta \cdot dz \quad (\text{C.3})$$

The integral over the angle gives 2π , due to polar symmetry the value of $(\vec{E} \times \vec{B}) \cdot \hat{n}$ is the same for any theta. For this reason, we can substitute the position vector per the value in the position $\vec{x} = \vec{b} = (0, b, z)$. So substituting this and also $dz = vdt$, the equation C.3 becomes C.4.

$$\frac{de}{dz} = \frac{2\pi \cdot b}{\mu} \int_{-\text{inf}}^{+\text{inf}} (\vec{E} \times \vec{B}) \cdot \hat{y} dt = \frac{2\pi \cdot b}{\mu} \int_{-\text{inf}}^{+\text{inf}} (\vec{E}_z(\vec{b}, t) \times \vec{B}_x(\vec{b}, t) - \vec{E}_x(\vec{b}, t) \times \vec{B}_z(\vec{b}, t)) dt \quad (\text{C.4})$$

Plancherel's theorem says that integrating the product of two functions in the time domain is equal to integrating the product of the Fourier transform of the same functions in the frequency domain. This is shown in equation C.5.

$$\int_{-\text{inf}}^{+\text{inf}} x(t)y(t)dt = \int_{-\text{inf}}^{+\text{inf}} X(\omega)Y^*(\omega)d\omega \quad (\text{C.5})$$

In equation C.5 $X(\omega)$ is the Fourier transform of $x(t)$ and $Y(\omega)$ is the Fourier transform of $y(t)$. So applying the Plancherel theorem in C.4 is obtained equation C.6.

$$\begin{aligned} \frac{de}{dz} &= \frac{2\pi \cdot b}{\mu} \int_{-\text{inf}}^{+\text{inf}} (\vec{E}_z(\vec{b}, \omega) \times \vec{B}_x^*(\vec{b}, \omega) - \vec{E}_x(\vec{b}, \omega) \times \vec{B}_z^*(\vec{b}, \omega)) d\omega = \\ &= \frac{4\pi \cdot b}{\mu} \text{Re} \left\{ \int_0^{+\text{inf}} (\vec{E}_z(\vec{b}, \omega) \times \vec{B}_x^*(\vec{b}, \omega) - \vec{E}_x(\vec{b}, \omega) \times \vec{B}_z^*(\vec{b}, \omega)) d\omega \right\} \end{aligned} \quad (\text{C.6})$$

The last term is obtained remembering that since the electric and magnetic fields are real, the real part of the Fourier transform is even and the imaginary part is odd. So integrating over all frequency space the imaginary part gives zero, and the odd gives 2 times the integral from 0 to infinity.

So the spectral energy density of Cherenkov radiation emitted by distance traveled in a medium by a charged particle is given by C.7.

$$\frac{d^2e}{d\omega dz} = \frac{4\pi \cdot b}{\mu} \text{Re}(\vec{E}_z(\vec{b}, \omega) \times \vec{B}_x^*(\vec{b}, \omega) - \vec{E}_x(\vec{b}, \omega) \times \vec{B}_z^*(\vec{b}, \omega)) \quad (\text{C.7})$$

C.1.1 The electromagnetic potentials

The next step is to calculate the electromagnetic potentials. Using the Lorenz gauge, the equations of the potentials in a medium are given by equations shown in C.8.

$$\begin{aligned}(\nabla^2 - \mu\epsilon\partial_t^2)V(\vec{x}, t) &= -\frac{p(\vec{x}, t)}{\epsilon} \\ (\nabla^2 - \mu\epsilon\partial_t^2)\vec{A}(\vec{x}, t) &= -\mu\vec{J}(\vec{x}, t)\end{aligned}\tag{C.8}$$

The Fourier transform and the inverse Fourier transform in all 4 coordinates (space-time) are defined as shown in equation C.9.

$$\begin{aligned}F(\vec{k}, \omega) &= \frac{1}{4\pi^2} \int \int d^3x dt f(\vec{x}, t) e^{i(\omega t - \vec{k} \cdot \vec{x})} \\ f(\vec{x}, t) &= \frac{1}{4\pi^2} \int \int d^3k d\omega F(\vec{k}, \omega) e^{i(-\omega t + \vec{k} \cdot \vec{x})}\end{aligned}\tag{C.9}$$

The Fourier transform of a function defined in the space domain is given by the function pair defined in equation C.10. Meanwhile, the pair of Fourier transform in the time domain to frequency domain is given by equation C.10 too.

$$\begin{aligned}f(\vec{x}) &\leftrightarrow F(\vec{k}) \\ f(t) &\leftrightarrow F(\omega)\end{aligned}\tag{C.10}$$

The Fourier transform of a function derivate in space or in time is given by equation C.11.

$$\begin{aligned}\nabla f(\vec{x}) &\leftrightarrow i\vec{k}F(\vec{k}) \\ \partial_t f(t) &\leftrightarrow -i\omega F(\omega)\end{aligned}\tag{C.11}$$

So using the properties equation given by C.11 and applying the Fourier transform in all coordinates (3 spatial and one temporal) of the equations that defined the Lorenz gauge, its obtained equation C.12.

$$\begin{aligned}(|k|^2 - \mu\epsilon\omega^2)V(\vec{k}, \omega) &= \frac{p(\vec{k}, \omega)}{\epsilon} \\ (|k|^2 - \mu\epsilon\omega^2)\vec{A}(\vec{k}, \omega) &= \mu\vec{J}(\vec{k}, \omega)\end{aligned}\tag{C.12}$$

The Fourier transform of the charge density is given by equation C.13.

$$\begin{aligned}
p(\vec{k}, \omega) &= \frac{1}{4\pi^2} \int \int d^3x dt p(\vec{x}, t) e^{i(\omega t - \vec{k} \cdot \vec{x})} = \frac{q}{4\pi^2} \int \int d^3x dt \delta(z - vt) \delta(x) \delta(y) e^{i(\omega t + \vec{k} \cdot \vec{x})} = \\
&= \frac{q}{4\pi^2} \int dz e^{i(\omega \frac{z}{v} - k_z z)} \int dx \delta(x) \int dy \delta(y) \int dt \delta(z - vt) = \frac{q}{4\pi^2} \int dz e^{iz(\frac{\omega}{v} - k_z)} = \frac{q}{2\pi} \delta(\omega - vk_z)
\end{aligned} \tag{C.13}$$

The current density transformation is shown in equation C.14.

$$\vec{J}(\vec{k}, \omega) = vp(\vec{k}, \omega) \hat{z} \tag{C.14}$$

So substituting equations C.13 and C.14 in C.12, it's possible to obtain the potentials as given equation C.15.

$$\begin{aligned}
V(\vec{k}, \omega) &= \frac{q\delta(\omega - vk_z)}{2\pi\epsilon(|k|^2 - \mu\epsilon\omega^2)} \\
\vec{A}(\vec{k}, \omega) &= \epsilon\mu v V(\vec{k}, \omega) \hat{z}
\end{aligned} \tag{C.15}$$

C.2 The Electromagnetic Fields

The fields are given by equations shown in C.16.

$$\begin{aligned}
\vec{E}(\vec{x}, t) &= -\nabla V(\vec{x}, t) - \partial_t \vec{A}(\vec{x}, t) \\
\vec{B}(\vec{x}, t) &= \nabla \times \vec{A}(\vec{x}, t)
\end{aligned} \tag{C.16}$$

Applying the Fourier transform in C.16 is obtained C.17.

$$\begin{aligned}
\vec{E}(\vec{k}, \omega) &= -i\vec{k} \cdot V(\vec{k}, \omega) + i\omega \vec{A}(\vec{k}, \omega) \\
\vec{B}(\vec{k}, \omega) &= i\vec{k} \times \vec{A}(\vec{k}, \omega)
\end{aligned} \tag{C.17}$$

Substituting equations C.15 in C.17 its obtained equation C.18

$$\begin{aligned}
\vec{E}(\vec{k}, \omega) &= i(\omega\epsilon\mu v \hat{z} - \vec{k}) V(\vec{k}, \omega) \\
\vec{B}(\vec{k}, \omega) &= i\epsilon\mu v V(\vec{k}, \omega) \vec{k} \times \hat{z} = i\epsilon\mu v V(\vec{k}, \omega) (k_y \hat{x} - k_x \hat{y})
\end{aligned} \tag{C.18}$$

So the magnetic field in the z-direction, which is needed in equation C.6 is zero. The only terms that we need to calculate are \vec{E}_z and \vec{B}_x .

In equation C.19 the magnetic field in the x-direction is returned to the space domain.

$$\begin{aligned}
B_x(\vec{x}, \omega) &= \frac{1}{(4\pi^2)^{\frac{3}{4}}} \int d^3k B_x(\vec{k}, \omega) e^{i\vec{k}\cdot\vec{x}} = \frac{iq\mu v}{(4\pi^2)^{\frac{5}{4}}} \int d^3k \frac{k_y \delta(\omega - vk_z)}{(|k|^2 - \mu\epsilon\omega^2)} e^{i\vec{k}\cdot\vec{x}} = \\
&= \frac{iq\mu v}{(4\pi^2)^{\frac{5}{4}}} \int \int dk_y dk_x \frac{k_y}{k_x^2 + k_y^2 + \omega^2(\frac{1}{v^2} - \epsilon\mu)} e^{ik_y y} e^{ik_x x} e^{i\frac{\omega}{v}z} \int dk_z \delta(\omega - vk_z) = \\
&= \frac{iq\mu e^{i\frac{\omega}{v}z}}{(4\pi^2)^{\frac{5}{4}}} \int \int dk_y dk_x \frac{k_y}{k_x^2 + k_y^2 + \omega^2(\frac{1}{v^2} - \epsilon\mu)} e^{ik_y y} e^{ik_x x}
\end{aligned} \tag{C.19}$$

The magnetic field at point $\vec{x} = \vec{b}$ is show in equation C.20

$$B_x(\vec{b}, \omega) = \frac{iq\mu e^{i\frac{\omega}{v}z}}{(4\pi^2)^{\frac{5}{4}}} \int_{-\infty}^{\infty} \int_{-\infty}^{\infty} dk_y dk_x \frac{k_y}{k_x^2 + k_y^2 + \omega^2(\frac{1}{v^2} - \epsilon\mu)} e^{ik_y b} \tag{C.20}$$

Calling $\Omega^2 = \omega^2(\frac{1}{v^2} - \epsilon\mu)$ and integrating over k_x the equation C.20 becomes
C.21.

$$B_x(\vec{b}, \omega) = \frac{iq\mu e^{i\frac{\omega}{v}z}}{4^{\frac{5}{4}}\pi^{\frac{3}{2}}} \int_{-\infty}^{\infty} dk_y \frac{k_y}{\sqrt{k_y^2 + \Omega^2}} e^{ik_y b} = \frac{iq\mu\Omega e^{i\frac{\omega}{v}z}}{4^{\frac{5}{4}}\pi^{\frac{3}{2}}} \int_{-\infty}^{\infty} du \frac{u}{\sqrt{u^2 + 1}} e^{iub\Omega} \tag{C.21}$$

The integral of C.21 can be written as shown in equation C.22.

$$\int_{-\infty}^{\infty} du \frac{u}{\sqrt{u^2 + 1}} e^{iub\Omega} = \frac{1}{i\Omega} \partial_b \int_{-\infty}^{\infty} du \frac{1}{\sqrt{u^2 + 1}} e^{iub\Omega} \tag{C.22}$$

The integral in equation C.22 can be opened as shown in equation C.23.

$$\int_{-\infty}^{\infty} du \frac{1}{\sqrt{u^2 + 1}} e^{iub\Omega} = \int_{-\infty}^{\infty} du \frac{\cos(ub\Omega)}{\sqrt{u^2 + 1}} + i \int_{-\infty}^{\infty} du \frac{\sin(ub\Omega)}{\sqrt{u^2 + 1}} \tag{C.23}$$

The second term gives zero since it's an integral of an odd function. However, the first term is just the two times the modified Bessel function of the second kind of order 0 ($2K_0(\Omega b)$)[67]. So the magnetic field becomes equation C.24.

$$B_x(\vec{b}, \omega) = \frac{2q\mu e^{i\frac{\omega}{v}z}}{4^{\frac{5}{4}}\pi^{\frac{3}{2}}} \partial_b K_0(\Omega b) \tag{C.24}$$

The recurring relation of the modified Bessel functions of second order is shown in equation C.25.

$$\frac{dK_v(x)}{dx} = -K_{v+1}(x) + \frac{v}{x} K_v(x) \tag{C.25}$$

Using this relation, it's possible the show the equation C.26 using the chain rule.

$$\partial_\alpha K_0(\alpha x) = \frac{dK_0(\alpha x)}{d(\alpha x)} \cdot \frac{d(\alpha x)}{d(\alpha)} = -K_1(\alpha x) \cdot x \quad (\text{C.26})$$

So the magnetic field can be written as shown in equation C.27.

$$B_x(\vec{b}, \omega) = \frac{-2q\mu\Omega e^{i\frac{\omega}{v}z}}{4^{\frac{5}{4}}\pi^{\frac{3}{2}}} K_1(\Omega b) \quad (\text{C.27})$$

Now, the electric field in the z-direction is calculated also making the Fourier transform as shown in equation C.28.

$$\begin{aligned} E_z(\vec{x}, \omega) &= \frac{1}{(4\pi^2)^{\frac{3}{4}}} \int d^3k E_z(\vec{k}, \omega) e^{i\vec{k}\cdot\vec{x}} = \\ &= \frac{iq}{\epsilon(4\pi^2)^{\frac{5}{4}}} \int dk_x dk_y \frac{\omega(\epsilon\mu v - \frac{1}{v})}{k_x^2 + k_y^2 + \Omega^2} e^{ik_y y} e^{ik_x x} e^{i\frac{\omega}{v}z} \int dk_z \delta(\omega - vk_z) = \\ &= \frac{iqe^{i\frac{\omega}{v}z}}{\epsilon v(4\pi^2)^{\frac{5}{4}}} \int dk_x dk_y \frac{\omega(\epsilon\mu v - \frac{1}{v})}{k_x^2 + k_y^2 + \Omega^2} e^{ik_y y} e^{ik_x x} \end{aligned} \quad (\text{C.28})$$

Also setting the coordinate to \vec{b} its obtained the equation C.29.

$$E_z(\vec{b}, \omega) = \frac{-iq\Omega^2 e^{i\frac{\omega}{v}z}}{\omega\epsilon(4\pi^2)^{\frac{5}{4}}} \int_{-\infty}^{\infty} \int_{-\infty}^{\infty} dk_x dk_y \frac{1}{k_x^2 + k_y^2 + \Omega^2} e^{ik_y b} \quad (\text{C.29})$$

Integrating in k_x its obtained equation C.30

$$E_z(\vec{b}, \omega) = \frac{-iq\Omega^2 e^{i\frac{\omega}{v}z}}{\omega\epsilon 2^{\frac{5}{2}}\pi^{\frac{3}{2}}} \int_{-\infty}^{\infty} dk_y \frac{1}{\sqrt{k_y^2 + \Omega^2}} e^{ik_y b} = \frac{-iq\Omega^2 e^{i\frac{\omega}{v}z}}{\omega\epsilon 2^{\frac{5}{2}}\pi^{\frac{3}{2}}} \int_{-\infty}^{\infty} du \frac{1}{\sqrt{u^2 + 1}} e^{iub\Omega} \quad (\text{C.30})$$

Using again the equation C.23 its obtained C.31.

$$E_z(\vec{b}, \omega) = \frac{-i2q\Omega^2 e^{i\frac{\omega}{v}z}}{\omega\epsilon 2^{\frac{5}{2}}\pi^{\frac{3}{2}}} K_0(b\Omega) \quad (\text{C.31})$$

C.3 Spectrum

So the spectral density of energy radiated by charged particles due to Cherenkov is given by equation C.32, substituting equation C.31 and C.27 in C.7.

$$\frac{d^2 e}{d\omega dz} = \frac{4\pi \cdot b}{\mu} \text{Re}(\vec{E}_z(\vec{b}, \omega) \times \vec{B}_x^*(\vec{b}, \omega)) = \frac{bq^2}{2\pi^2\omega\epsilon} |\Omega|^2 \text{Re}(i\Omega K_0(\Omega b) K_1^*(\Omega b)) \quad (\text{C.32})$$

Considering the spectrum far from the particle ($\Omega b \gg 1$), the Bessel function turns out in function C.33 [21].

$$K_0(\Omega b) \approx K_1(\Omega b) \approx \sqrt{\frac{\pi}{2b\Omega}} e^{-\Omega b} \quad (\text{C.33})$$

So equation C.32 becomes C.34.

$$\frac{d^2 e}{d\omega dz} = \frac{q^2}{4\pi\epsilon\omega} |\Omega|^2 \text{Re}\left(i \frac{\sqrt{\Omega}}{\sqrt{\Omega^*}} e^{-b(\Omega+\Omega^*)}\right) \quad (\text{C.34})$$

The omega term can be manipulated as shown in equation C.35.

$$\Omega = \sqrt{\omega^2 \left(\frac{1}{v^2} - \epsilon\mu\right)} = \omega \sqrt{\frac{1}{c^2 \beta^2} - \frac{n_{medium}^2}{c^2}} = \frac{\omega}{c} \sqrt{\frac{1}{\beta^2} - n_{medium}^2} \quad (\text{C.35})$$

The particle will emit radiation only if the term inside the $\text{Re}\cdot$ is real. This happen when the term $\sqrt{\frac{\Omega}{\Omega^*}} e^{-b(\Omega+\Omega^*)}$ is imaginary.

If Ω is real, that happens when $\beta < 1/n_{medium}$, which means that the particles are slower than the speed of light of the medium the term $\sqrt{\frac{\Omega}{\Omega^*}} e^{-b(\Omega+\Omega^*)}$ becomes $e^{2\Omega b}$ which is real. Then the particle doesn't emit Cherenkov radiation.

If Ω is imaginary the term, that happens when $\beta > 1/n_{medium}$, which means that the particles are faster than the speed of light of the medium the term $\sqrt{\frac{\Omega}{\Omega^*}} e^{-b(\Omega+\Omega^*)}$ becomes $\sqrt{-1} = i$. So the particle will emit Cherenkov radiation.

In this condition, the equation C.34 becomes C.36.

$$\frac{d^2 e}{d\omega dz} = \frac{q^2 n_{medium}^2 \omega}{4\pi\epsilon c^2} \left(1 - \frac{1}{(\beta n_{medium})^2}\right) = \frac{q^2 \mu \omega}{4\pi} \left(1 - \frac{1}{(\beta n_{medium})^2}\right) \quad (\text{C.36})$$

The Cherenkov spectrum in terms of frequency is given by equation C.37. This is made remembering that $\omega = 2\pi f$.

$$\frac{d^2 e}{df dz} = \pi q^2 \mu f \left(1 - \frac{1}{(\beta n_{medium})^2}\right) \quad (\text{C.37})$$

So finally the Cherenkov spectrum of the number of emitted photons in terms of wavelength is given by equation C.38. This is made remembering that for a photon the relation between energy and wavelength is $E_\gamma = \frac{hc}{\lambda}$ and $c = \lambda f$, so the total energy of N photons is equal to $\frac{Nhc}{\lambda}$.

$$\frac{d^2N}{d\lambda dz} = \frac{\pi q^2 \mu c}{h} \frac{1}{\lambda^2} \left(\frac{1}{(\beta n_{\text{medium}})^2} - 1 \right) \quad (\text{C.38})$$

APPENDIX D – Photomultiplier

D.1 Photomultiplier Tube

A photomultiplier (PMT) is a device that detects photons using the photoelectric effect.

The device is a vacuum tube with the following elements composing it: a photocathode, an electron optical input system, the collection of dynodes, and the anode. Figure 130 shows a schematic of a PMT.

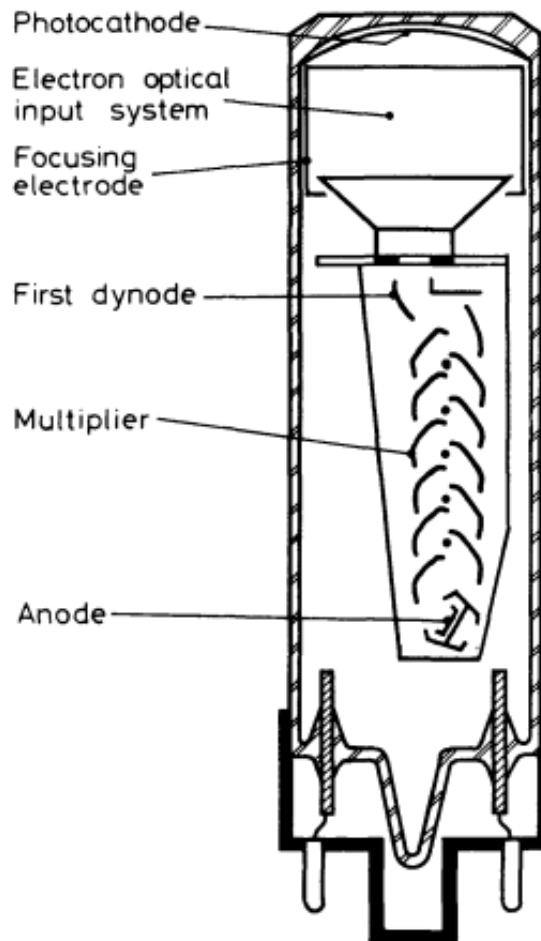


Figure 130 – Schematic of a PMT [8]

The photon that arrives in the window of the PMT and collides with the

photocathode, can free an electron from the material due to the photoelectric effect. To free the electron, the photon energy needs to be greater than the work function (Φ) of the material, since the kinetic energy of the free electron after gaining energy from the photon is given by D.1.

$$T_{e^-} = hf - \Phi \quad (\text{D.1})$$

The PMT is powered up with a high voltage of the order of 1000V to 2000V. The negative and positive potential are connected to the cathode and anode respectively.

This voltage is distributed along the device, from anode to cathode, so there will be a potential difference between each of the dynodes, between a dynode and the electrode, or between the electrodes. More details in D.1.3.

D.1.1 Electron Optical Input System

When the electron is ejected in the cathode due to potential difference it goes toward the focus electrode. This section is made in a way that independent of the region of the cathode that the electron is free it takes the same amount of time to reach the focus.

To achieve this goal the collection window is made with a certain curvature. The equipotential lines generated because of the voltage applied between the focusing electrode and the acceleration electrode are shown in figure 131.

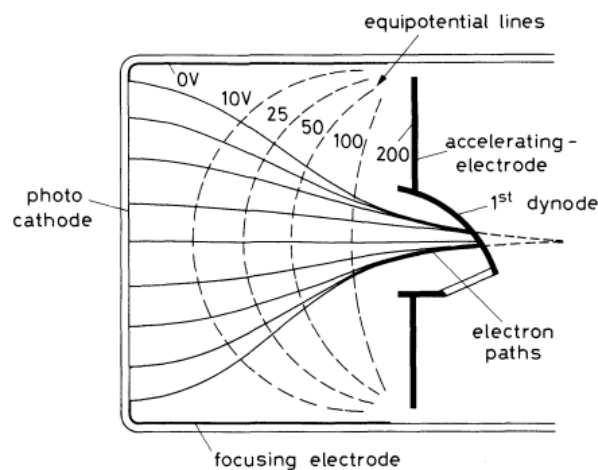


Figure 131 – Equipotential lines in Electron Optical Input System [8]

D.1.2 Photomultiplication

The photo-electron is accelerated by the accelerating electrode and arrives in the system of dynodes.

When an energetic electron collides with a dynode, it will eject more electrons in the vacuum. These electrons get accelerated by the electric field and collide with the next dynode generating more electrons. This mechanism is responsible for the PMT's high gain. On average a PMT has around 10 to 14 dynodes.

D.1.3 Voltage Divider

The voltage divider is a collection of resistors of series that feed the PMT. A schematic of a voltage divider can be seen in figure 132.

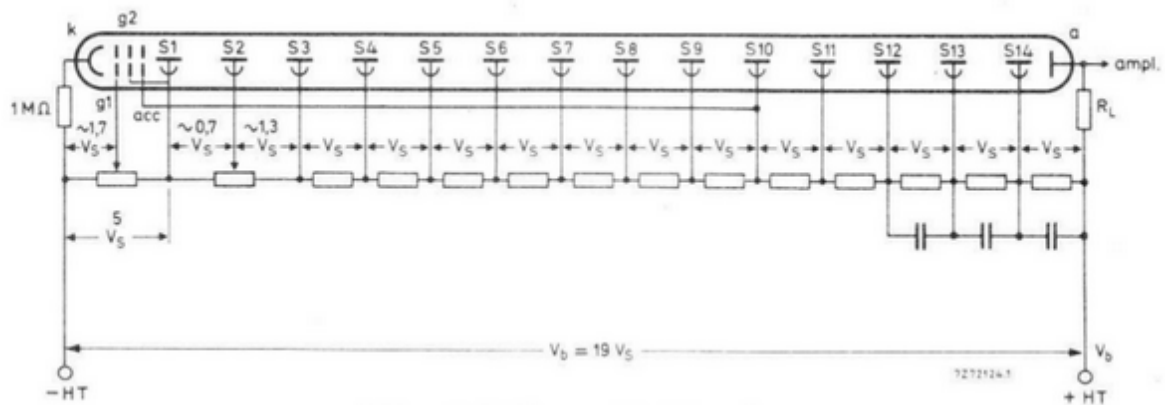


Figure 132 – Electric Diagram of a voltage divider [26]

The gain of each step is very sensitive to the potential difference between each dynode. The current in the resistors must be greater than the current inside the PM. For example, if the inside current increases, the outside current must not decrease to maintain the gain constant. Also in the last stages it can be added capacitors, as shown in 132, to maintain the voltage between the dynodes.

The output current is read in the anode, and to decouple the high voltage it's necessary to add a capacitor in series with the input impedance of the readout electronics.

D.1.4 Gain

The gain of each step of photo multiplication is proportional to the potential difference between each dynode as given by equation D.2.

$$G_d = k.V_d \quad (\text{D.2})$$

So the overall gain is given by multiplying the gain of each step (N steps) as shown in equation D.3.

$$G = (k.V_d)^N \quad (\text{D.3})$$

Since the voltage between the dynodes is a fraction of the applied voltage, the gain is proportional to the applied voltage multiplied N times, as shown in figure 133.

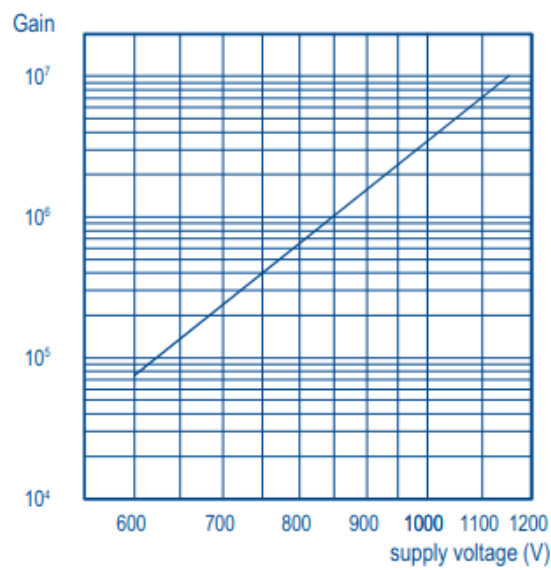


Figure 133 – Plot of the gain as a function of the applied voltage [30]

D.1.5 Linearity

The output current of a PMT is directly proportional to the number of photons hitting the window as shown in figure 134.

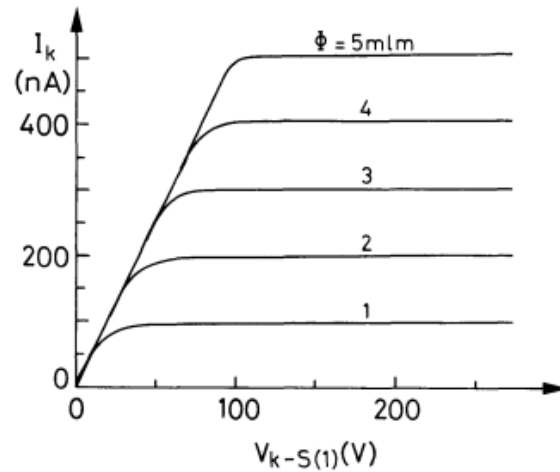


Figure 134 – Plot of the current as a function of the applied voltage and luminosity flux [8]

But is only true above a threshold of applied voltage. This happens because at low voltages not all electrons are collected by the dynodes. Meanwhile at high voltage occurs a saturation in the gain, because all electrons are captured by the dynodes and the current becomes proportional to the incident flux (desired relationship).

D.1.6 Quantum Efficiency

The Quantum Efficiency ($N(\lambda)$) is an important quantity and measures the probability of an incident photon in the cathode to generate a photon-electron. A Photon with a lower wavelength has more energy and as consequence, it's easier to win the work function of the material. But too lower wavelength photons are absorbed by PMT window glass.

Another useful quantity is the radiant cathode sensitivity ($S(\lambda)$) which is defined as the ratio of current produced in the cathode by the photoelectric effect over the incident power flux, as shown in equation D.4.

$$S(\lambda) = \frac{I_k}{P(\lambda)} \quad (\text{D.4})$$

The term I_k and $P(\lambda)$ can be written as D.5 and D.6, respectively.

$$I_k = e \frac{n_e^{\text{catode}}}{dt} = e \cdot N(\lambda) \frac{n_\gamma(\lambda)}{dt} = e \cdot N(\lambda) \cdot \text{flux}_\gamma(\lambda) \quad (\text{D.5})$$

$$P(\lambda) = flux_{\gamma}(\lambda).E(\lambda) = flux_{\gamma}(\lambda).hf = flux_{\gamma}(\lambda).\frac{hc}{\lambda} \quad (D.6)$$

Substituting [D.5](#) and [D.6](#) in [D.4](#), we obtain equation a relation between quantum efficiency and radiant cathode sensitivity, as shown in equation [D.7](#).

$$S(\lambda) = \lambda n(\lambda) \frac{e}{hc} = \frac{\lambda.N(\lambda)}{1240} \frac{[A]}{[W]} \quad (D.7)$$

D.2 Silicon photomultipliers

A silicon photomultiplier is a device capable to detect photons and emit an electrical signal as a response. Basically is a set of PN junctions reversely powered and working in the avalanche regimen.

To better comprehend its work, it will be revised briefly on how the PN junction and the avalanche regimen work.

D.2.1 PN Junction

A PN junction arises when a type N semiconductor gets in touch with a type P semiconductor. The type N semiconductor is the one that was doped with more electronegative atoms. Therefore the material has an excess of electrons. The type P is the one that has an excess of holes because it was doped with materials less electronegative.

When these two materials get in touch, the excess electrons in the N region will go through the process of diffusion to the P region and will recombine with the holes in that region. While that the holes will go to the N region and will recombine with the electrons in that region.

This process can not happen forever and, in fact, as the electrons leave the N region an excess of positive charge will be left behind. While, as the hole leave the region, an excess of negative charge will be left behind.

This charge difference generates an electric field in the direction of the N region to the P region. Therefore electrons in the N region and the holes of the P region will be repelled by this electric field, not being able to pass through the region. The formed region is called the depletion region. [Figure 135](#) is shown an illustrative scheme of the PN junction in equilibrium.

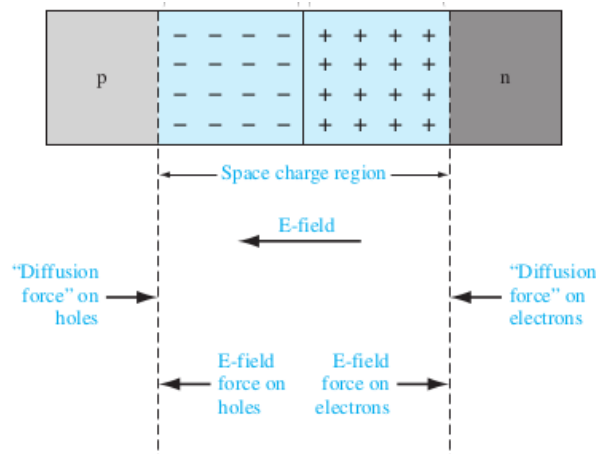


Figure 135 – Scheme of PN junction [31]

For the device to directly conduct (in the P to N direction) it is necessary to apply a potential difference such that the potential barrier of the depletion region decreases, allowing the passage of charge carriers.

By reversely polarizing the device the effect will increase the depletion region and barrier's potential, increasing the electric field and difficulting the passage of charge carriers.

The figure 136 shows the direct polarizing effect and the reverse polarizing effect of a junction.

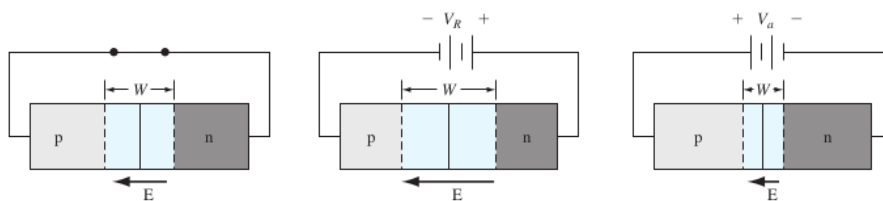


Figure 136 – Polarizing effect of a PN junction [31]

When the junction is reversely polarized with a very high voltage, it can generate a current or by Zener effect or by Avalanche effect.

As the temperature increases, the concentration of charge carriers also increases by thermal generation. As a consequence more holes cross the potential barrier from N to P and more electrons from P to N. This causes the depletion region to decrease and as a consequence, the junction potential also decreases.

D.2.1.1 Avalanche effect

When the applied reverse voltage is too high, the electrons and the holes that eventually arrive at the depletion zone are strongly accelerated by the intense electric field in the region.

These charge carriers receive a lot of kinetic energy in the process and, when colliding with others charge carriers in the region, generate pairs of electrons-holes, that also will be accelerated by the electric field, generating a cascade effect. As a result, in the device will be generated a reverse current.

The increase in the temperature causes in the voltage potential breakdown avalanche the inverse of what happens in the junction potential. In this case, the increase in the temperature causes a higher thermal agitation in the atoms, decreasing the free path of the electrons. Therefore it is necessary a higher reverse voltage to start the impact ionization.

D.2.2 SiPM

A SiPM is a set of microcells in parallel to each other, arranged in a rectangular matrix as shown in Figure 137. Each microcell has an area in the order of tens of μm^2 .

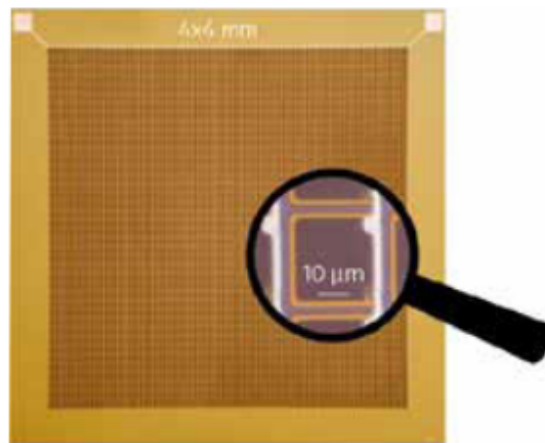


Figure 137 – Microcells matrix forming a SiPM [32]

Each microcell is a set in parallel of avalanche photodiodes operating in reverse polarization (Geiger mode). In the figure 138 it is shown a schematic of a microcell. The R_q resistor shown is the quenching resistor.

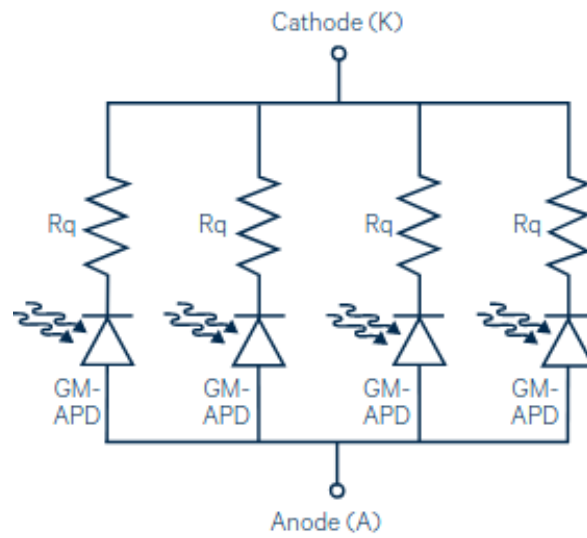


Figure 138 – Electric diagram of a microcell [32]

When a photon is absorbed one electron of the valence band is promoted to the conduction band and generates one electron-hole pair.

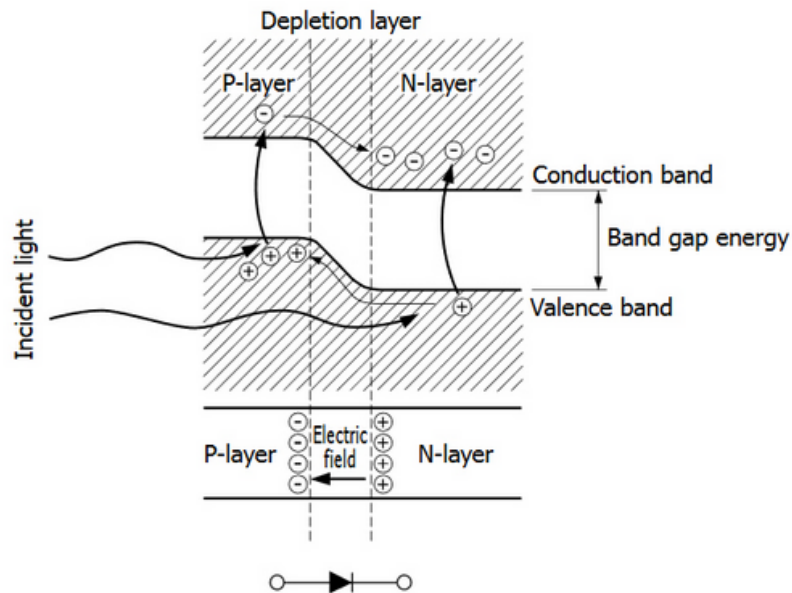


Figure 139 – Diagram of a SiPM band [33]

The generated hole in the n side out of the depletion zone is transported to the p side by diffusion process, while the electron generated in the p side out of the depletion

zone is transported to the n side also by diffusion process. However since this process depends on the diffusion velocity, this process is slow.

The fast process happens when a pair is generated inside the depletion zone. Due to the semiconductor being operated in avalanche regimen, the generated holes and electrons have the cascade effect mentioned in D.2.1.1. It is important to highlight that the rate of ionization of an electron is greater than the hole's rate [68].

Photons with a wavelength higher penetrate deeper into the interior of the device as shown in figure 140. Furthermore, in the figure it is shown the parts of an avalanche photodiode that make up a SiPM.

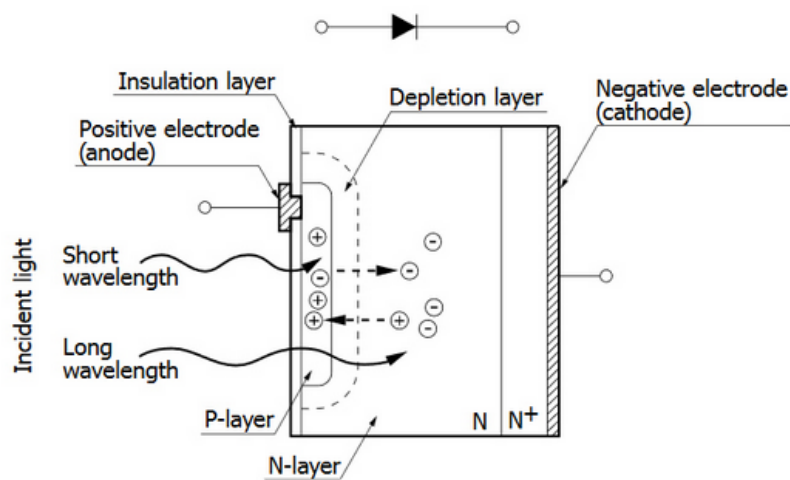


Figure 140 – Scheme of an avalanche photodiode [33]

Beyond that the device can be built in two different ways: the P-on-N mode or the N-on-P mode. In the figure 141 it is shown both types.

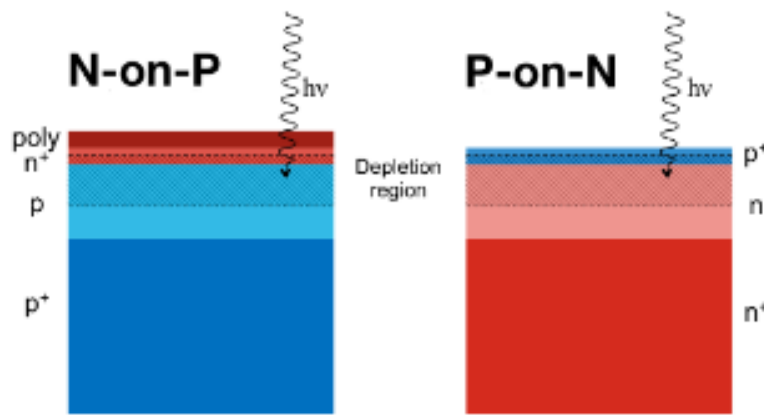


Figure 141 – P-on-N and N-on-P photodiodes [34]

Since the electrons when generated will be accelerated to the N region, the bigger the distance traveled in the depletion region, the more the electrons and holes pairs will be ionized. For this reason, the type N-on-P have a greater gain to photon with higher wavelength, once the electron will be more generated in the interior of the device and will have to cross most part of the depletion region until arriving in the cathode, as exemplified in the figure 142.

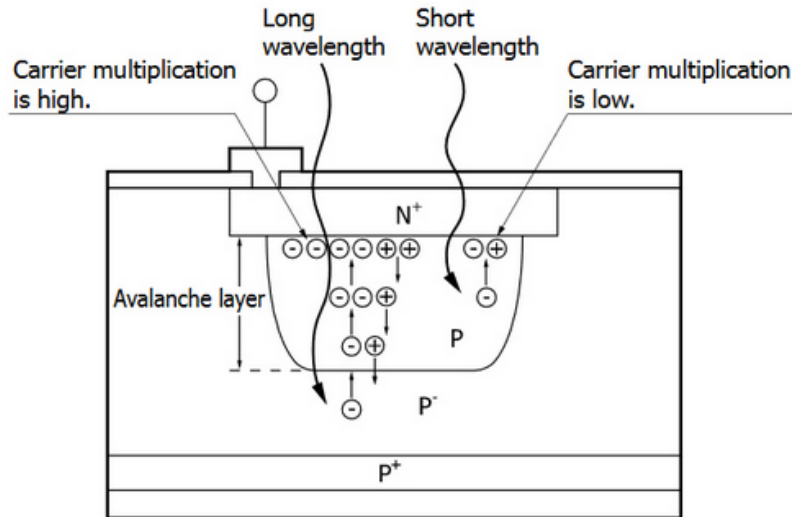


Figure 142 – Photodiode P-on-N and N-on-P [33]

The inverse is also true and when the semiconductor is P-on-N, the electrons generated on the surface of the device will travel a larger path in the depletion region in

the direction of the cathode. Therefore this type amplifies more the light signals with low wavelengths.

Anyway, returning to the working of the optical sensor, the device is powered with a voltage greater than the avalanche breakdown voltage. When the photon is collected, the avalanche effect takes action and a current will appear in the device. This current would last forever if it wasn't for the presence of the R_q that dispels the energy until the diode stops conducting. In other words, the current increases (due to the avalanche effect), and the voltage in R_q also increases ($V = RI$). Therewith the potential drop in the diode decreases until the applied voltage becomes not enough to maintain the avalanche.

While the semiconductor is in avalanche effect and conducting, its voltage decreases, and will be blind for newly collected photons and will only be able to collect a new photon after the current drop next to zero (reverse conduction current). Therefore a photodiode can only count one photon at a time.

But since each microcell (each pixel) has a large set of photodiodes, and since a SiPM has an enormous set of pixels, this device is a great photon counter, being limited only to the total number of photodiodes.

In experiments in which the SiPM goes in cryogenics environments, the reverse voltage necessary to cause the avalanche effect is much smaller, as explained in [D.2.1.1](#). As a consequence the gain increases in environments with lower temperatures, once the gain is proportional to the overvoltage applied to the device, as will be explained in section [D.2.3](#).

D.2.3 Electric Model

A branch of a SiPM's pixel can be modeled as shown in figure [143](#).

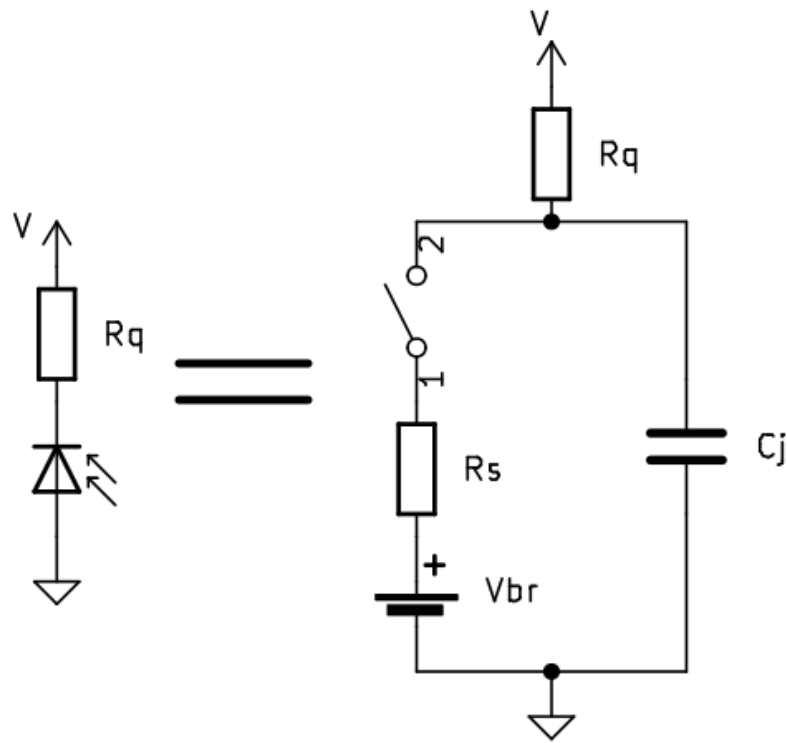


Figure 143 – Electric model of a SiPM

In the model, V is the reverse power voltage that is equal to $V = V_{br} + V_{ov}$. The term V_{br} is the breakdown voltage and V_{ov} is the over voltage above the breakdown voltage. The capacitance C_j is the junction capacitance of the diode, and the resistance R_{a_s} is the internal resistance of the device.

While no photon is detected, the switch stays open and no current runs through the device. This stage is called quiescent mode.

When a photon is detected the switch closes and the avalanche process starts. This stage is called discharge mode because the charge accumulated in the internal capacitance is discharged in the resistors. The avalanche process would go on forever if energy was not been dissipated in the quenching resistor.

The Thévenin equivalent circuit seen by the capacitor is shown in figure 144.

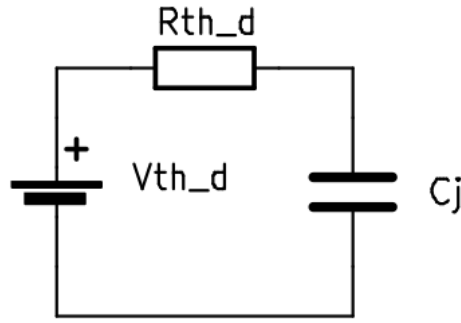


Figure 144 – Thevenin equivalent in discharge phase

Where the thévenin source and thévenin is given by equations D.8 and D.9.

$$V_{TH}^D = V_{br} + V_{ov} \frac{R_s}{R_q + R_s} \quad (D.8)$$

$$R_{TH}^D = R_q // R_s \quad (D.9)$$

Since R_q needs to quench the current, his value must be greater than R_s . In this limit $V_{TH}^D \approx V_{br}$ and $R_{TH}^D \approx R_s$. Then the discharge constant of time is equal to $\tau_D = C_j * R_{TH}^D \approx C_j * R_s$.

So the voltage across the capacitor, which is the same voltage of the photodiode, is given by equation D.10.

$$V_{PD}^D(t) = V_{C_j} = V_{TH}^D + (V - V_{TH}^D) e^{\frac{-t}{\tau_D}} = V_{br} + V_{ov} e^{\frac{-t}{\tau_D}} \quad (D.10)$$

And the current that crosses the semiconductor is given by equation D.11.

$$i_{PD}^D(t) = \frac{V - V_{PD}^D(t)}{R_q} = \frac{V_{ov}}{R_q} (1 - e^{\frac{-t}{\tau_D}}) \quad (D.11)$$

When the voltage across the photodiode becomes near the breakdown voltage, the device can't support the avalanche process anymore. In this stage the switch closes, and the capacitor starts to recharge. This stage is called the recovery phase.

This stage is just an RC circuit, with R equal to R_q , C equal to C_j and the initial capacitor voltage is approximately V_{br} . So the constant of time (τ_R) is equal to $R_q.C_j$.

So the voltage across the capacitor, which again is the same across the semi-conductors, is given by equation D.12.

$$V_{PD}^R(t) = V + (V_{br} - V)e^{\frac{-t}{\tau_R}} = V - V_{ov}e^{\frac{-t}{\tau_R}} \quad (D.12)$$

And as consequence, the current in the device equals to D.13.

$$i_{PD}^R(t) = \frac{V - V_{PD}^R(t)}{R_q} = \frac{V_{ov}}{R_q} e^{\frac{-t}{\tau_R}} \quad (D.13)$$

With equation D.11 and D.13 it's possible to plot the output current when a photon is detected. This plot is shown in figure 145. In the plot, it's possible to note that the recovery time is much greater than the discharge time.

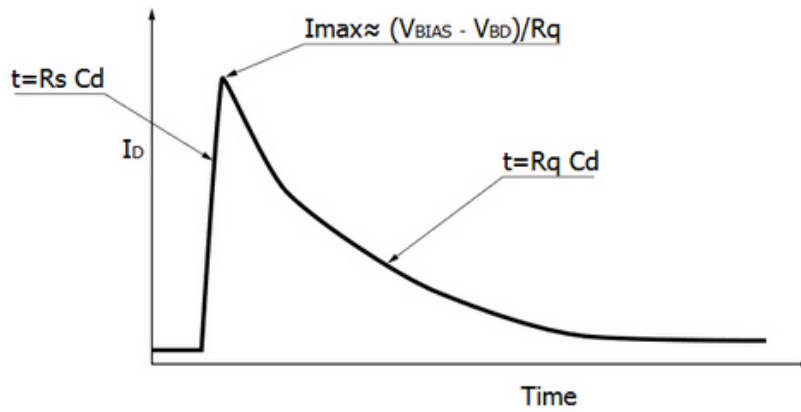


Figure 145 – Expected current signal when a photon is detected in a single cell [33]

When the capacitor recharges the circuit returns to quiescent mode.

The charge in the signal can be found integrating the current over all the signal time, but since recovery time is much bigger than discharge time, we can approximate integrating only in recovery time, as given by equation D.14.

$$Q = \int_0^{\infty} i_{PD}(t) dt \approx \int_0^{\infty} i_{PD}^R(t) dt = C_j V_{ov} \quad (D.14)$$

So the single photon-electron's gain is given by equation D.15. It's possible to note that the gain is directly proportional to the overvoltage applied to the SiPM, as we can see in figure 146.

$$G = \frac{Q}{e} = \frac{C_j V_{ov}}{e} \quad (\text{D.15})$$

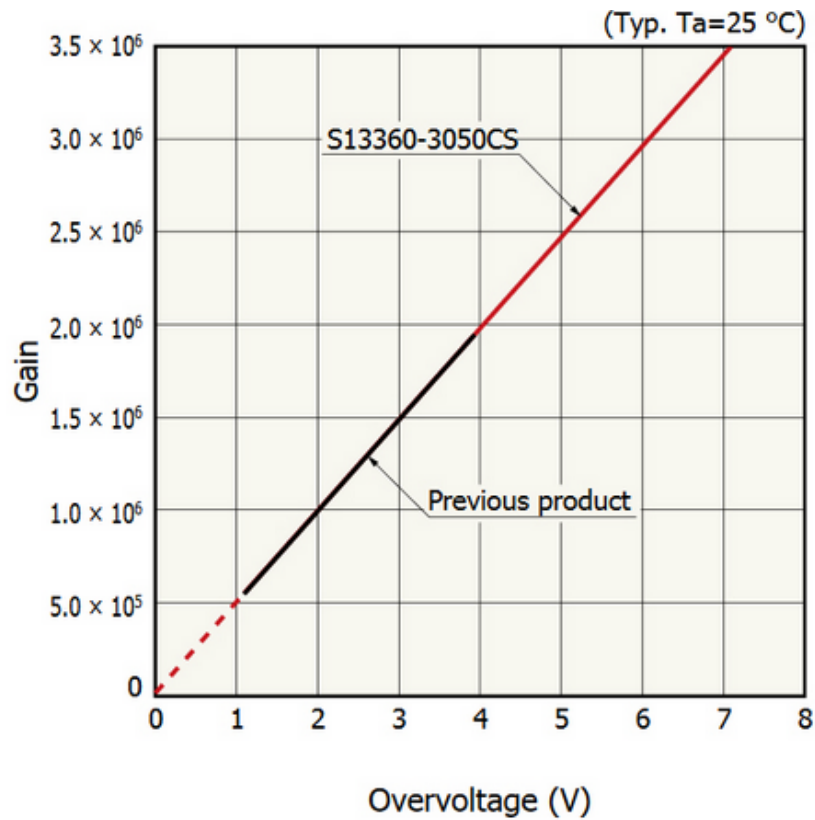


Figure 146 – Gain as a function of Overvoltage [33]

But it's important to remember, that a microcell is in parallel with another microcell, so when a microcell is activated its output is affected somehow by the other microcells. It's possible to model this behavior as shown in figure 147. More information can be seen in [35].

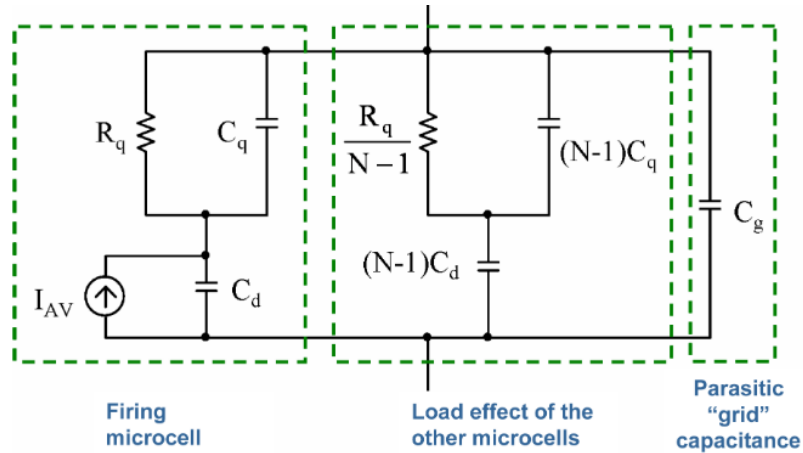


Figure 147 – Electric model of a SiPM [35]

D.2.4 Measurement circuit

The circuit shown in 143 is just to understand the output waveform. But in practice, we need to put the signal generated in an amplifier with the input impedance of $Z_i n$.

Also to maintain the voltage applied of V in the SiPM even when a lot of current is driven by the source voltage, it's recommended to put a capacitor in parallel with the source. The circuit is shown in 148. A resistor R can also be added to protect the device in case of a lot of light is exposed, and protect the SiPM from a high current.

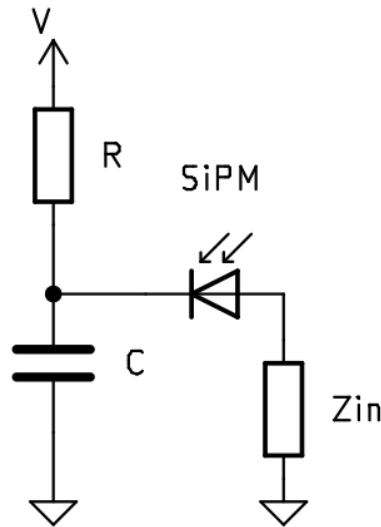


Figure 148 – Circuit for reading SiPM's Signal

The current that is created in the device can be approximated to [D.11](#) and [D.13](#), but substituting R_q to $R_q + Z_{in}$, since these two resistances are in series. So the voltage across the input impedance is equal to $I \cdot Z_{in}$, which is proportional to $\frac{Z_{in}}{Z_{in} + R_q}$. So as we increase the value of Z_{in} , more voltage "enters" the amplifier and greater the gain.

At the same time, as we increase Z_{in} , greater is going to be the time constant of the recover phase ($\tau_R = (R_q + Z_{in}) \cdot C_j$) so the signal will last longer. So the rate of detection of photons of the device will decrease. So we have a situation of win-loss between gain and photon rate detection.

D.2.5 Photon Detection Efficiency

The Photon Detection Efficiency (PDE), nothing more, is the probability of a photon that arrives in SiPM's window becoming an electrical pulse as seen in [D.2.3](#).

Then PDE is given by equation [D.16](#).

$$PDE = QE \cdot FF \cdot Pt \quad (\text{D.16})$$

In equation [D.16](#), QE is the quantum efficiency, FF is Geometrical Fill Factor and Pt is the Triggering Probability.

The quantum efficiency is the probability of a photon generating an electron-hole pair. This probability is related to the photon wavelength, since the photon energy is

equal to hf , and this energy is the capability of promoting an electron to the conduction band or a hole to the valance band.

The Triggering Probability is the probability of a generated electron-hole pair to initialize the avalanche process. As discussed in D.2.2 this process is related to the position where the pair is generated, which is related to the wavelength. This means that the Triggering Probability is a function of the wavelength. Also as strong the electric field in the depletion region, more chance of the avalanche starting, so Triggering Probability is also a function of the V_{ov} .

By last, the geometrical fill factor is the active optical area of the SiPM. The SiPMs have some dead areas due to other components and structures in the board.

Figure 149 shows the photon detection efficiency of a Sipm as a function of Overvoltage and photon wavelength.

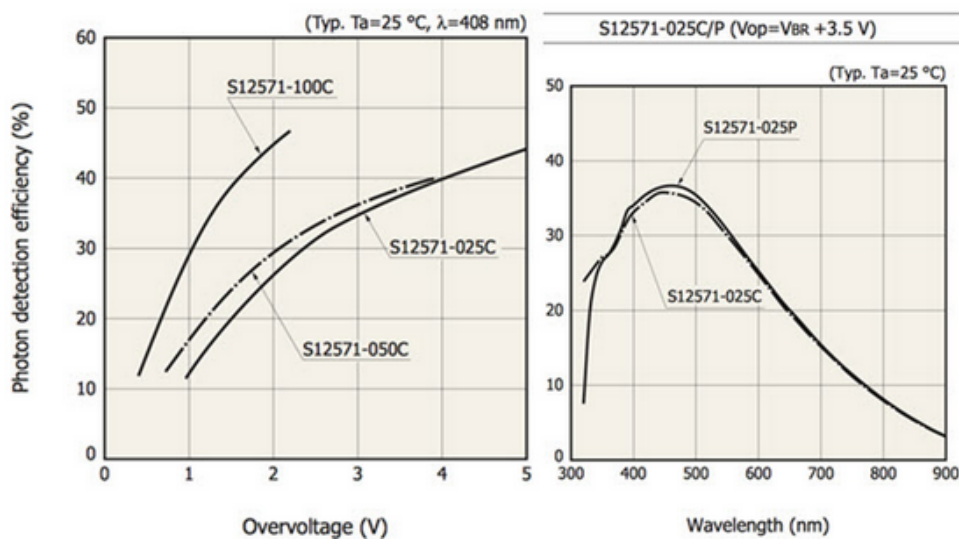


Figure 149 – PDE as a function of overvoltage and wavelength [36]

D.2.6 Noise Sources

The three greatest noise sources and unwanted signals are dark noise, crosstalk and afterpulses.

D.2.6.1 Dark Noise

Dark noise are the signals generated by thermal generated electron-holes pair. When those pairs are generated by thermal agitation, there is a probability that starts the

avalanche breakdown, and a signal can be produced even in absence of light. Since dark noise is a phenomenon due to temperature, as the temperature increases the dark noise also increases.

D.2.6.2 Afterpulse

When a discharge occurs due to photon absorption or thermal noise some charge carriers can be trapped in lattice defects. After the pulse finishes, those trapped charge carriers can be released and restart the avalanche breakdown, and as consequence, a second delayed pulse is emitted. In figure 150 are show examples of afterpulses.

D.2.6.3 Crosstalk

When a discharge takes place, the temperature inside the semiconductor increases, resulting in the emission of photons. These photons move through the semiconductor and some of them exit the device, while others are reabsorbed by either the same photodiode or neighboring ones. The reabsorbed photons can create additional electron-hole pairs, increasing the likelihood of generating pulses in other junctions. Consequently, the output pulse may be higher than anticipated, as a result of the superposition effect. In figure 150 are show examples of crosstalk.

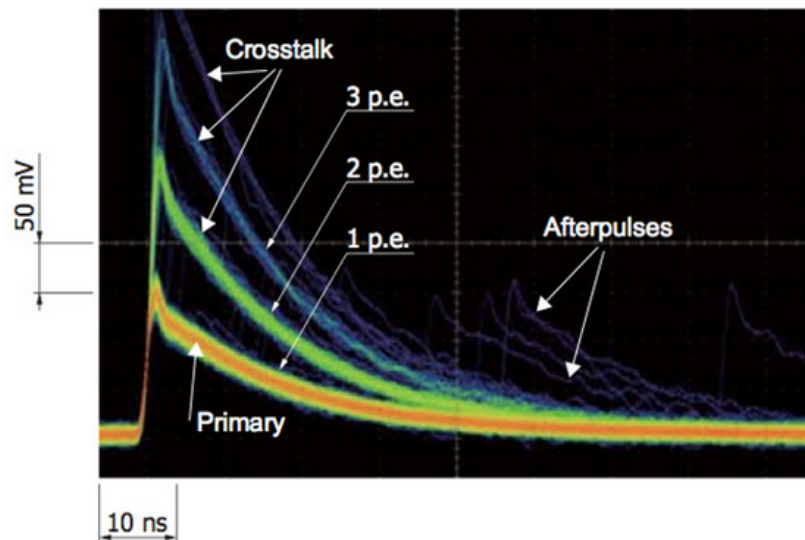


Figure 150 – Crosstalk and Afterpulses in a SiPM [33]

APPENDIX E – WaveLength Shifters

The organic scintillators are formed by hydrocarbons that contain chemical structures called benzenes. The scintillation lights originated from delocalized electrons (electrons that are not associated with any molecule) that came from benzene rings.

The carbon atoms suffer from a process called hybridization sp^2 in benzene rings, in which the carbon passes through two s complete orbitals and two p incomplete orbitals, to a s complete orbital, a p complete orbital and three sp^2 incomplete orbitals, due to the superposition of the original orbitals. This gives the atom a plane trigonal geometry. The hybridization process can be viewed better in the figures 151 and 152.

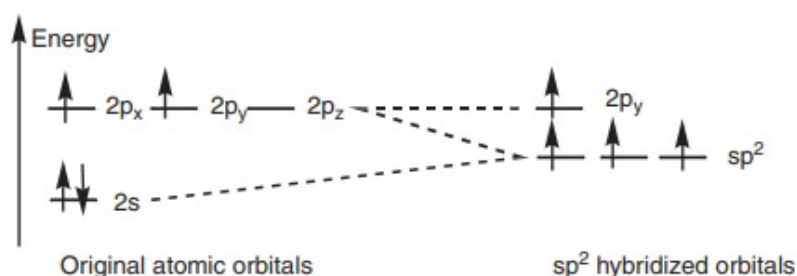


Figure 151 – sp^2 hybridization process [37]

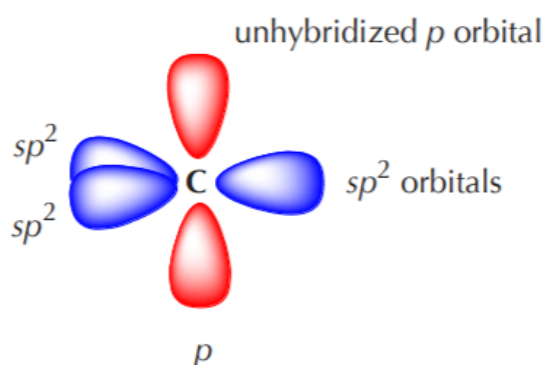


Figure 152 – Shape of the orbitals [38]

Due to this geometry, the benzene molecule shows 6 π connections - as shown in figure 153. This p orbital set forms a ring-shaped electronic cloud, in which the electrons could be in any place described by it. Those are the delocalized electrons.

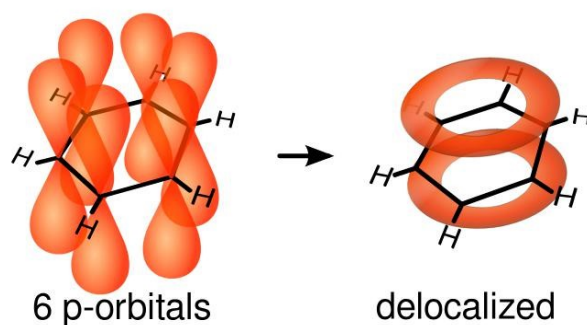


Figure 153 – π connections in the benzene molecule and resultant orbital [39]

The π connection electrons form a state of singlets or triplets. The figure 154 shows the energetic levels of an organic scintillator. Each level of energy associated with a singlet (S) or a triplet (T), shows a fine structure of possible energy related to a degree of vibrational energy.

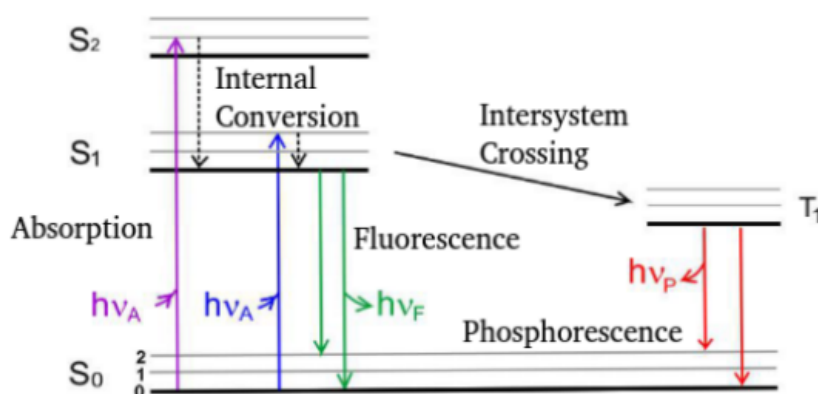


Figure 154 – Levels of energy of an organic scintillator [40]

The fundamental state is the singlet state S_0 . The singlet state can be described as in the equation E.1.

$$|S\rangle = \frac{|\uparrow\downarrow\rangle - |\downarrow\uparrow\rangle}{\sqrt{2}} \quad (\text{E.1})$$

When absorbing energy, the electron goes to a greater energy singlet state. It can also happen that the electron has its spin changed (which is much rare) and the

system goes to a triplet state. There are three triplet states with the same energy, which are described in the equation E.2.

$$\begin{aligned} |T_+\rangle &= |\uparrow\uparrow\rangle \\ |T_0\rangle &= \frac{|\uparrow\downarrow\rangle + |\downarrow\uparrow\rangle}{\sqrt{2}} \\ |T_-\rangle &= |\downarrow\downarrow\rangle \end{aligned} \quad (\text{E.2})$$

In figure 155 it is shown examples of an energy promotion of a singlet state with greater energy or to a triplet state.

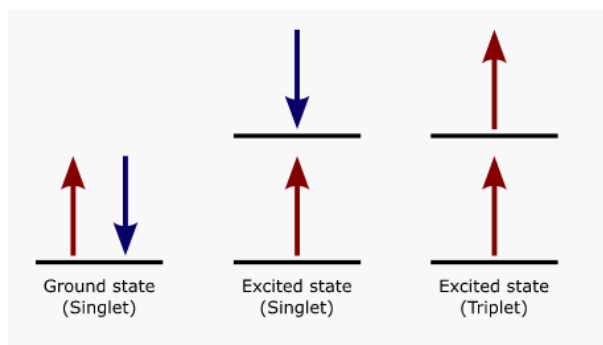


Figure 155 – Levels of energy of a organic scintillator [41]

As seen in figure 154, the triplet states show greater energy than their singlet counterpart. This happens, in short, because the electrons, for being fermions, need to be in antisymmetric wave functions to satisfy Pauli's exclusion principle. But the total wave function of two electrons is the combination of the spatial part with the spin part.

Therefore, since the singlet has an antisymmetric spin part, its spacial part is symmetric. The triplet, however, shows a symmetric spin function, hence its spatial function is antisymmetric.

It is possible to show that a pair of electrons whose spatial part is symmetric have a shortest average distance between each other, while electrons whose spatial part is antisymmetric have a greater average distance between each other [69].

Therefore singlets states have electrons closer to each other, which means that the system has a greater potential electric energy related to the triplet, in which the electrons are further from each other, hence it is justified the fact that singlet states show a higher energy than triplets states.

Finally, the transition of a singlet state to a triplet state and vice versa is extremely prohibited, due to the multipole transition rules.

When an electron is promoted to a higher energetic singlet state - like the S1 - it suffers a quick internal conversion, releasing its vibrational energy in the form of heat and going to the least energetic S1 band.

From this moment, two results can happen: the most common one is that the electron undergoes the process of fluorescence - a quick process in which decays to an S0 state of energy - emitting, in the process, a photon with lower energy than the utilized to promote the particle to the S1 level; the second possible process - however, the least probable (due to selection rules) - is that the system suffers from an intersystem crossing, and goes from a singlet state to a triplet state, this process occurs releasing energy in the form of heat and decreasing the total spin of the system in 1 (without the emission of a photon) and this is only possible because of the spin-orbit coupling of the system.

When the system is at a triplet state, the transition to a singlet state takes more time than the singlet-singlet transition, due to the transition being prohibited. This transition is called phosphorescence and is characterized by a long decay time, and a lower energy is released by the photon.

Since the energy released by both processes in general is lower than the required energy to promote the electron, the material tends to be transparent to its own scintillation, which is desired.